Opto-Electronic Science

Review

April 2025, Vol. 4, No. 4

DOI: 10.29026/oes.2025.240030 CSTR: 32246.14.oes.2025.240030

Structural color: an emerging nanophotonic strategy for multicolor and functionalized applications

Wenhao Wang[1†], Long Wang[1*], Qianqian Fu[2†], Wang Zhang[3†], Liuying Wang[1], Gu Liu[1], Youju Huang[2*], Jie Huang[1], Haoyuan Zhang[1], Fuqiang Guo[1] and Xiaohu Wu[4*]

Color as an indispensable element in our life brings vitality to us and enriches our lifestyles through decorations, indicators, and information carriers. Structural color offers an intriguing strategy to achieve novel functions and endows color with additional levels of significance in anti-counterfeiting, display, sensor, and printing. Furthermore, structural colors possess excellent properties, such as resistance to extreme external conditions, high brightness, saturation, and purity. Devices and platforms based on structural color have significantly changed our life and are becoming increasingly important. Here, we reviewed four typical applications of structural color and analyzed their advantages and shortcomings. First, a series of mechanisms and fabrication methods are briefly summarized and compared. Subsequently, recent progress of structural color and its applications were discussed in detail. For each application field, we classified them into several types in terms of their functions and properties. Finally, we analyzed recent emerging technologies and their potential for integration into structural color devices, as well as the corresponding challenges.

Keywords: structural color; metasurface; photonic crystals; dynamic tunable

Wang WH, Wang L, Fu QQ et al. Structural color: an emerging nanophotonic strategy for multicolor and functionalized applications. *Opto-Electron Sci* **4**, 240030 (2025).

Introduction

Structural color has gained tremendous attention since it was discovered in nature[1]. It can be observed not only in a wide range of creatures, like butterflies, beetles, chameleons, and octopuses, but also in our daily life, e.g., digital versatile discs (DVDs), soap bubbles, and windows. The light-matter interaction, diffraction, scattering, interference, etc., produce vivid and bright color features with high stability, endurance, and environmental friendliness[2,3]. It holds more competitive edges than traditional coloration strategies and thus makes it promising in many fields. Besides, the properties of non-toxic, non-fading, physical and chemical resistance and uncomplicated manufacture enable it to be an ideal alternative to dyes and pigments[4,5]. Therefore, researchers have made great efforts to increase structural color gamut and

[1]Zhijian Laboratory, Rocket Force University of Engineering, Xi'an 710025, China; [2]College of Materials, Chemistry and Chemical Engineering, Hangzhou Normal University, Hangzhou 311121, China; [3]Engineering Product Development, Singapore University of Technology and Design, Singapore 487372, Singapore; [4]Thermal Science Research Center, Shandong Institute of Advanced Technology, Jinan 250100, China.
[†]These authors contributed equally to this work.
*Correspondence: L Wang, E-mail: wlxs520@126.com; YJ Huang, E-mail: yjhuang@hznu.edu.cn; XH Wu, E-mail: xiaohu.wu@iat.cn
Received: 19 November 2024; Accepted: 6 January 2025; Published online: 26 March 2025

improve brightness and purity, making structural color adapt to more extensive fields. Meanwhile, dynamically tunable and responsive photonic devices are in great demand for the needs of pacing technology innovation, which provides extensive opportunities for structural color. These properties can be easily achieved by adjusting the geometric parameters or refractive index under outer stimuli. The continuous exploration of structural color has led to its application in anti-counterfeiting, display technology, sensors, and printing. Consequently, an increasing number of multifunctional devices have been invented to enhance our lives and boost various industries[6–8].

There are several types of structural color platforms, including metasurface[9–13], photonic crystal (PC)[14,15], plasmonic resonance[16,17], resonance cavity[18,19], closed and non-closed packed colloid particle[20–23]. The structural color of metasurfaces is attributed to periodic structure design and the coupling enhancement of meta-atoms, which endow perfect impedance matching or resonance excitation. Consequently, metasurfaces offer the capability to manipulate light in a manner that aligns with our specific intentions, providing tailored responses to various optical stimuli, despite the challenges associated with their high cost and the complexity of large-scale fabrication[24,25]. Moreover, they can manipulate the flow of light in amplitude[26], phase[27–29], and polarization[30–33] within subwavelength structures. Based on Mie scattering and resonance, plasmonic resonance, and Fano resonance etc., dielectric and metal metasurfaces can conveniently produce structural color[34]. Nanostructures with elaborate geometry designs, such as rods, disks, and voids, are widely chosen for application. However, the fabrication process, characterized by its time-consuming nature and high costs, primarily impedes the industrial application and broader acceptance of this technology. Nevertheless, the high-resolution capabilities beyond the diffraction limit and angle independence contribute to its significant status. Typically, focused ion beam milling (FIB)[35], electron-beam lithography (EBL)[36], interference lithography (IL)[37], and femtosecond laser-induced periodic surface structures (LIPSS)[38,39] are several mainstream manners. Benefiting from the advances of nano/micro-scale fabrication, PC leads the way to structural color with more diversities in one dimension (1D), two dimension (2D), and three dimension (3D) than its counterparts, which allows the patterns to embrace more flexibility, and less limitation on materials choice[40–43]. Besides, woodpile structures have demonstrated their effectiveness in achieving full photonic bandgaps, attracting a considerable amount of research interest[44,45]. The aforementioned techniques, classified as top-down approaches, face limitations that hinder their widespread adoption. In contrast, bottom-up methods are gaining preference due to their cost-effectiveness and rapid prototyping capabilities. To overcome these limitations, self-assembled colloidal crystals have garnered significant interest among researchers. The focus is on leveraging the inherent advantages of bottom-up synthesis to enhance manufacturability and efficiency[46–48]. As a kind of PC, it shows extreme compatibility with other substrates, which means it could be integrated with many different kinds of materials to achieve novel functions, such as hydrogels[49], polydimethylsiloxane (PDMS)[30], shape-memory polymers[50], magnetic particles and more[51,52]. To realize structure color, closed or non-closed colloidal particles are prerequisites to form ordered systems, where a photonic stop band caused by Bragg diffraction prevents the transmission of specific wavelengths of light, leading to high reflectance within a specific visible spectrum related to lattice constants. Structural colors are produced by various techniques, including Fabry-Perot (F-P) nanocavities with superimposed metal-insulator-metal (MIM) layers[53–55] and multilayer thin films fabricated through methods such as magnetron reactive sputtering, plasma-enhanced chemical vapor deposition (PECVD), or electron-beam evaporation. These methods exhibit vibrant colors based on different principles: F-P nanocavities achieve this through narrowband absorption due to resonance enhancement, while multilayer thin films utilize photonic bandgaps[56,57].

This paper is a comprehensive review of recent advancements in the field of structural color, with a particular focus on its applications in anti-counterfeiting, display technology, sensors, and printing (Fig. 1). Firstly, a variety of fabrication methods are discussed and compared, ultimately focusing on the selection of structural colors that are specifically suited for a range of application scenarios. Secondly, this review dissects the mechanisms underlying the emergence of structural colors and the foundational principles of their design in terms of micro/nano photonics strategy. A comparative analysis of five typical structural coloration principles is presented, shedding light on their individual advantages and limitations. This critical evaluation is intended to streamline the progression from conceptual design to

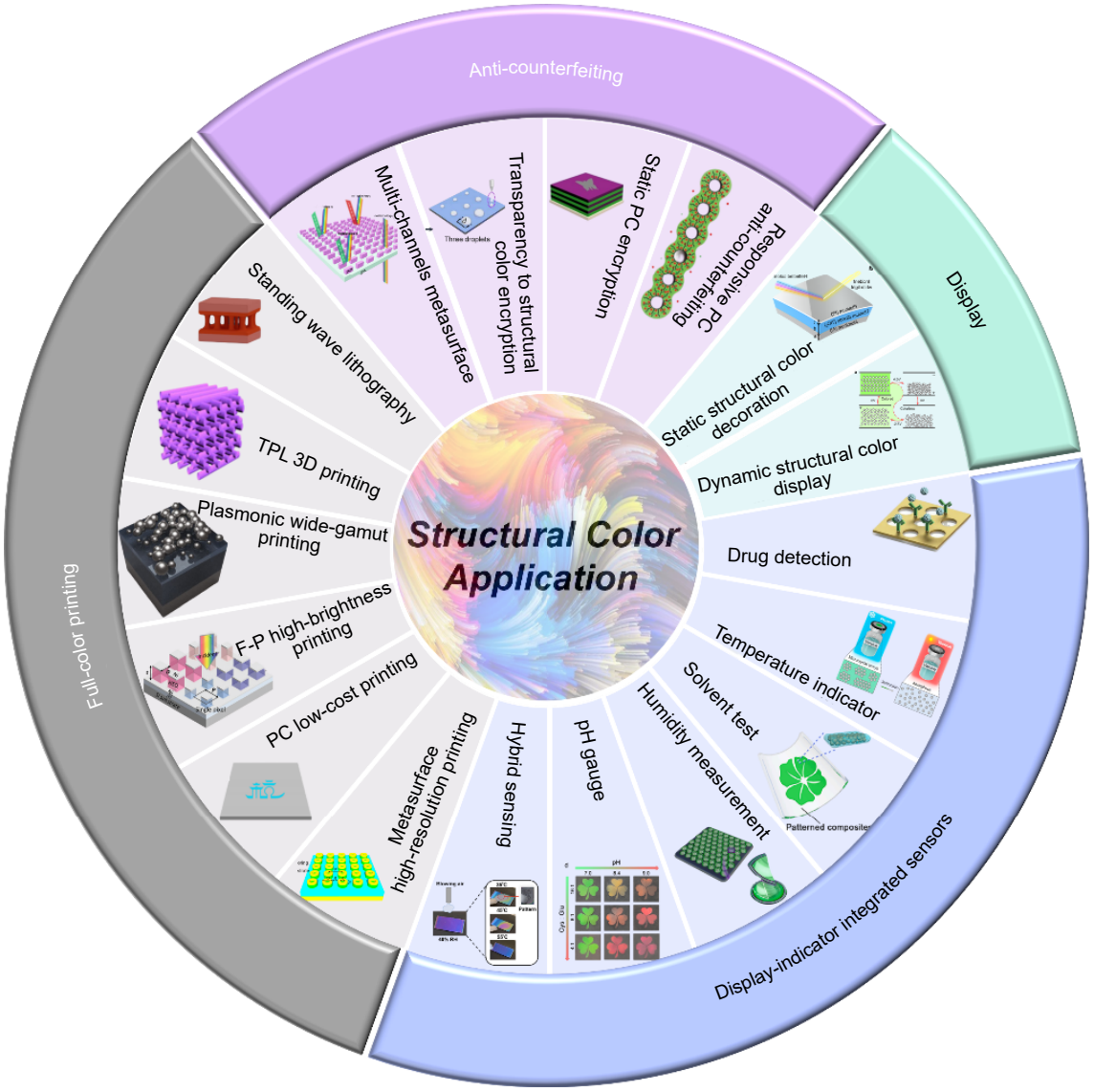

Fig. 1 | Overview of structural color applications. Multi-channels metasurfaces, transparency to structural color encryption, static PC encryption, responsive PC anti-counterfeiting, static structural color decoration, dynamic structural color display, drug detection, temperature indicator, solvent test, humidity measurement, pH gauge, hybrid sensing, metasurface high-resolution printing, PC low-cost printing, F-P high-brightness printing, plasmonic wide-gamut printing, two-photon lithography (TPL) 3D printing, standing wave lithography. Figure reproduced with permission from: ref.[64], American Chemical Society; ref.[65], AAAS; ref.[66], American Chemical Society; ref.[52], John Wiley and Sons; ref.[67], American Chemical Society; ref.[21], Springer Nature; ref.[68], John Wiley and Sons; ref.[49], American Chemical Society; ref.[69], Elsevier; ref.[70], Elsevier; ref.[71], American Chemical Society; ref.[72], Elsevier; ref.[73], American Chemical Society; ref.[42], American Chemical Society; ref.[74], John Wiley and Sons; ref.[75], Springer Nature; ref.[45], Springer Nature; ref.[37], Springer Nature.

practical application. Thirdly, the review delves into the burgeoning applications of structural colors from artificial structures to colloidal crystals. It grounds the discussion in practical applications that showcase the versatility of current design strategies and their capacity to satisfy a broad array of functional demands. Finally, this review presents the challenges ahead and potential avenues for future research.

This review sets itself apart from prior studies with the following distinctive contributions[58–63]:

1) We categorized the main structural color fabrication methods into bottom-up, top-down, and hybrid approaches, providing guidance for selecting suitable methods in various applications scenarios.

2) We thoroughly discuss the five primary mechanisms of structural coloration, providing an in-depth understanding of the behavior of structural colors from the perspectives of fundamental physics and photonics.

3) We have comprehensively discussed the application potential and intrinsic relationships of structural colors, moving beyond mere descriptions of single structural color method, thus providing an application-oriented perspective to clarify the prospects of structural color applications.

Methods

A summary of fabrication methods, building blocks, advantages and their functionalities is presented in Table 1. The numerous methods for fabricating structural colors can be broadly categorized into three approaches: the bottom-up method, the top-down method, and a hybrid approach that integrates both. The bottom-up method, notable for its cost-effectiveness and accessible fabrication process, holds significant potential for industrial-scale production. Conversely, the top-down method excels in creating intricate nano-/microstructures, catering to high-resolution demands in display and printing technologies, albeit at the expense of higher manufacturing

Table 1 | A summary of different fabrication methods for structural color.

Classification	Fabrication method	Building blocks	Advantages	Functionalities	Ref.
Bottom-up method	Magnetic field induced self-assembly	Fe_3O_4@TA-PVP nanoparticle	Magneto-responsive	Display	ref.[51]
		Fe_3O_4@PVP@PGDMA		Display and anti-counterfeiting	ref.[52]
	Steric repulsion induced self-assembly	Fe_3O_4-attached *den*-BBCP(AW-*b*-BnW)		Display	ref.[76]
	Dip-coating	ZnS@SiO_2 nanoparticle	Thermo-responsive, programmable encryption	Sensor, display and anti-counterfeiting	ref.[77]
	Open mill machine	PS@PEA@P(EA-*co*-AA)	Humidity-responsive and flexible	Sensor, display and anti-counterfeiting	ref.[78]
	Evaporation induced self-assembly	SiO_2 nanoparticle	Alcohol-responsive	Sensor and anti-counterfeiting	ref.[14]
		CeO_2@SiO_2	Electrically responsive and high saturation	Display	ref.[46]
		SiO_2 nanoparticle	Self-healing, programmable and flexible		ref.[79]
	Sacrificial template method	Inverse opal polypeptide	Solvent/pH dual-responsive	Anti-counterfeiting	ref.[71]
		Inverse opal PFS	Electrically responsive	Display	ref.[80]
	Confined self-assembly of suspension	P(MMA-BA) nanoparticle	Mechanically/pH dual-responsive	Anti-counterfeiting, sensor	ref.[81]
	Spin-coating	TiO_2/PMMA 1D PC	Low-cost and vapor/solvent response	Anti-counterfeiting	ref.[66]
	Electron-beam evaporation	ZnS/Ge 1D PC	Precise color and large-scale	Display	ref.[82]
		ZnS/Ge/Ag multilayer film	Wide-gamut, high purity, and large-scale		ref.[83]
	Air-water interface self-assembly	PS nanoparticle	Mechanically responsive, fast and high brightness	Sensor	ref.[84]
	Silkscreen printing	SiO_2 nanoparticle	Fast and large-scale	Printing and anti-counterfeiting	ref.[85]
	Hydrothermal growth	ZnO flower-like nanostructure	Feasible and low-cost	Display	ref.[86]
	Spray coating	P(St-MMA-AA) nanoparticles	High brightness and angle-independence	Display and sensor	ref.[87]
	Polymerization and microfluidic chip	Oil droplet	Low-cost	Display	ref.[88]
	Functional group modification and layer by layer dip coating	Chitosan/CMC-N_3 1D PC	Fast, low-cost, and temperature/relative humidity dual-responsive	Display and anti-counterfeiting	ref.[72]

Table 1 (Continued)

Classification	Fabrication method	Building blocks	Advantages	Functionalities	Ref.
Top-down method	EBL, reactive ion etching, and inductively coupled plasma	Asymmetric Al cross	Dual-mode color states, high-density information encoding storage	Display, anti-counterfeiting and printing	ref.[31]
	FIB	Nanohole	High-resolution and precise color	Display and printing	ref.[35]
	EBL and reactive ion etching	Si nanorod	Solvent response, high brightness and purity, and wide gamut	Printing and anti-counterfeiting	ref.[36]
	Pulsed laser printing	Ag nanojet	Fast and convenient	Printing and anti-counterfeiting	ref.[89]
	Nanoimprinting	PDMS grating	Fast and dynamic tunable	Display and anti-counterfeiting	ref.[90]
	Femtosecond laser lithography	Hydrogel micropillar	Designable and vapor responsive	Anti-counterfeiting and printing	ref.[91]
	Two-photon polymerization lithography	Woodpile IP-Dip resist	Ultra-high resolution and 3D printing	Anti-counterfeiting and printing	ref.[45]
Bottom-up and top-down integrated method	PECVD, electron beam evaporation, and EBL	Al grating	Multi-mode polarization encoding and broad color range	Display, anti-counterfeiting and printing	ref.[92]
	PECVD and EBL	Si_3N_4 nanorod	High-resolution and dual-mode color states	Display, anti-counterfeiting and printing	ref.[64]
	Magnetron sputtering and EBL	*α*-Si cube	High-resolution and electrically tunable	Display	ref.[93]
	Chemical crosslinking and ink-jet printing	Polymer microdome	Janus property, high-resolution, large-scale, and convenient	Printing	ref.[65]
	Chemical crosslinking and digital light processing 3D printing	Highly charged elastic nanoparticle	4D printing, thermos-responsive		ref.[94]
	Seed-mediated method and laser	Au nanoplate	High resolution	Printing	ref.[95]
	Femtosecond laser lithography and Electron-beam evaporation	TiAlN/TiN film	High resolution and precise color design		ref.[38]

Note: The bottom-up method emphasizes the gradual assembly of micro-/nanostructures through chemical synthesis or straightforward physical techniques, starting from basic components and building up to the complete structure. Conversely, the top-down method employs sophisticated micro- and nanofabrication tools to meticulously craft structures via subtractive manufacturing, focusing on the evolution from bulk materials to tailored micro- and nanostructures. The bottom-up and top-down integrated method combines both, integrating the distinctive attributes of each method to form a cohesive and synergistic fabrication process.

costs. Furthermore, the synergistic integration of bottom-up and top-down methods has forged a pioneering pathway to reconcile the competing priorities of cost and fabrication efficiency. As the field of structural color technology advances, these diverse fabrication techniques can be strategically selected to address the nuanced requirements of specific application scenarios.

Coloration mechanisms

The various nanostructures inherent in structural color platforms facilitate distinct light-matter interactions, each manipulating light based on its unique mechanism. Herein, we briefly introduce the fundamental principles of five main types of structural color generation strategies, including 1D PC, F-P cavity, 2D and 3D colloidal crystal, and metasurface (Fig. 2).

1D structural color

1D PC

The creation of structural colors can be achieved through the strategic alternation of layers with high and low refractive indices within a one-dimensional PC. These 1D PCs exhibit distinct optical properties that are

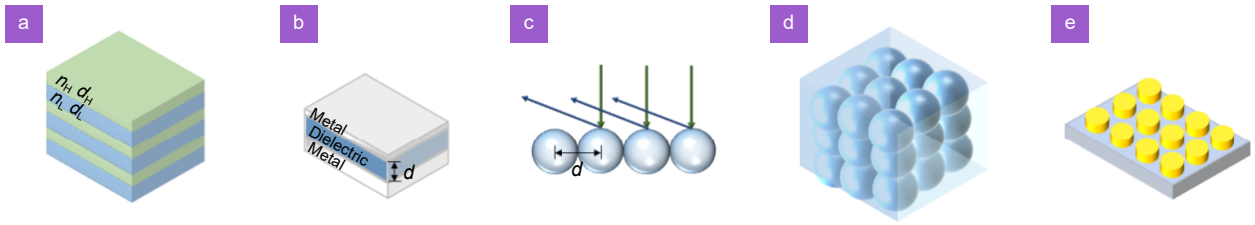

Fig. 2 | Mechanisms of structural color. (**a**) Schematic diagram of 1D PC with alternative high and low refractive index dielectric layer. n_H and n_L are the refractive indices of the high and low refractive index dielectric layer, and d_H and d_L are their corresponding thickness. (**b**) F-P cavity with a configuration that dielectric layer with thickness d is sandwiched between two metal layers. (**c**) 2D colloidal crystal with particle distance d. (**d**) 3D colloidal crystal that is surrounded by materials with refractive index contrast. (**e**) Schematic diagram of the metasurface.

influenced by factors such as periodicity, refractive index contrast, layer thickness, and the surrounding environment. The distinctive optics characteristics stem from the photonic bandgap (PBG) formation, a phenomenon arising from the constructive interference of light waves[66,96,97]. As depicted in Fig. 2(a), the traditional 1D PC does not necessitate the utilization of costly lithographic techniques such as FIB, EBL, or femtosecond laser. Instead, a variety of coating methods, including magnetron sputtering, electron beam evaporation, and spin coating, are viable alternatives. It is crucial to control the deposition rate meticulously to ensure robust interlayer bonding and to mitigate the risk of film cracking due to excessive internal stress.

For periodic 1D PC (with the same refractive index and thickness for all basic units), the center wavelength λ_0, the reflectivity R, and the bandwidth of PBG $\Delta\lambda_0$ are given by the following equations[62,98–100]

$$n_{\rm H}d_{\rm H} = n_{\rm L}d_{\rm L}=2m\lambda \ , \tag{1}$$

$$R = \left[\frac{1-\left(\frac{n_{\rm H}}{n_{\rm L}}\right)^{2N}\frac{n_{\rm H}^2}{n_{\rm a}n_{\rm s}}}{1+\left(\frac{n_{\rm H}}{n_{\rm L}}\right)^{2N}\frac{n_{\rm H}^2}{n_{\rm a}n_{\rm s}}}\right]^2 , \tag{2}$$

$$\Delta\lambda_0 = \frac{4\lambda_0}{\pi}\arcsin\left[\frac{n_{\rm H}-n_{\rm L}}{n_{\rm H}+n_{\rm L}}\right] , \tag{3}$$

where m is the diffraction order (m=0, 1, 2, …); $n_{\rm H}$ and $n_{\rm L}$ are the refractive indices of the high and low refractive index layers; $d_{\rm H}$ and $d_{\rm L}$ refer to the thickness of high and low refractive index layers; $n_{\rm a}$ and $n_{\rm s}$ are the refractive indices of free space (usually air) and substrate respectively; N is the number of periods.

For quasi-periodic 1D PC which has a "doping layer" or forms periodic units with more than two layers, the total reflection and transmission can be described by the transfer matrix method (TMM) as follows[101–103]:

$$\boldsymbol{M}_l = \begin{bmatrix} \cos\left(2\pi n_l d_l\frac{\cos\theta_l}{\lambda}\right) & \frac{\sin\left(2\pi n_l d_l\frac{\cos\theta_l}{\lambda}\right)}{\eta_l}\,{\rm j} \\ {\rm j}\eta_l\sin\left(2\pi n_l d_l\frac{\cos\theta_l}{\lambda}\right) & \cos\left(2\pi n_l d_l\frac{\cos\theta_l}{\lambda}\right) \end{bmatrix} , \tag{4}$$

$$\eta_l = \begin{cases} n_l/\cos\theta_l, {\rm TM} \\ n_l\cos\theta_l, {\rm TE} \end{cases} , \tag{5}$$

$$\begin{bmatrix} E_{l-1} \\ H_{l-1} \end{bmatrix} = \boldsymbol{M}_l \begin{bmatrix} E_l \\ H_l \end{bmatrix} , \tag{6}$$

where $\boldsymbol{M}_l$ is the characteristic matrix of l layers; d_l, n_l and θ_l are the thickness, refractive index and refracting angle of the $l_{\rm th}$ layer, respectively; λ is the wavelength of the light; η_l is the admittance; and E_{l-1}, H_{l-1} and E_l, H_l are the tangential components of electric and magnetic fields of l–$1_{\rm th}$ and $l_{\rm th}$ layer, respectively. According to Snell's law, $n_l\sin\theta_l$=$n_0\sin\theta_0$, the final characteristic equation of all n layers can be expressed as

$$\begin{bmatrix} E_l \\ H_l \end{bmatrix} = \prod_{l=1}^{n} M_l \begin{bmatrix} E_n \\ H_n \end{bmatrix} = \begin{bmatrix} m_{11} & m_{12} \\ m_{21} & m_{22} \end{bmatrix} \begin{bmatrix} E_n \\ H_n \end{bmatrix} . \tag{7}$$

Specifically, the total reflection R and transmission T are given by the following equations

$$R = \left|\frac{m_{11}+\eta_n m_{12}-\eta_0^{-1}\left(m_{21}+\eta_n m_{22}\right)}{m_{11}+\eta_n m_{12}+\eta_0^{-1}\left(m_{21}+\eta_n m_{22}\right)}\right|^2 , \tag{8}$$

$$T = \frac{4{\rm Re}\left(\eta_n/\eta_0\right)}{\left|m_{11}+\eta_n m_{12}+\eta_0^{-1}\left(m_{21}+\eta_n m_{22}\right)\right|^2} , \tag{9}$$

where η_0 is the admittance of the air and $\eta_{\rm n}$ is the admittance of the $n_{\rm th}$ layer. The structural color of a 1D PC arises from the selective reflection of light at specific wavelengths; that is, altering the position of PBG can readily change color.

F-P cavity

F-P cavity bears similarities to the 1D PC in terms of

configuration. However, the key distinction lies in its simpler three-layer configuration, which facilitates more accessible and straightforward production of structural color (Fig. 2(b)). The top metal layer and bottom mirror layer form a cavity to confine light in the dielectric layer, which results in an absorption peak or reflection dip[18,57]. In addition, the F-P cavity is usually asymmetric, with a thinner top metal layer and a thicker bottom layer. In this case, incident light can effectively come into the resonance cavity to support F-P resonance mode and interference of light at the metal-dielectric interface. The reflection intensity can be calculated as[104]

$$R = \frac{2R_{\rm m}\cdot(1-\cos\delta)}{1+R_{\rm m}^2-2R_{\rm m}\cos\delta}\ , \tag{10}$$

$$\delta = 2m\pi = \frac{2\pi}{\lambda}\cdot n\cdot 2d\cdot\cos\theta_{\rm t}\ , \tag{11}$$

where $R_{\rm m}$ is the reflectance of the metal mirror and δ is the phase difference of the neighboring emergent light from dielectric to air after the bottom mirror's reflection. In Eq. (11), m is the resonance order at wavelength λ; n and d are the refractive index and thickness of the dielectric spacer, respectively, and $\theta_{\rm t}$ is the angle of transmission.

F-P cavity resonance has more sensitive angle-dependence due to the derivation of (λ/θ) being highly dependent on n and incident angle[83,105,106]. When the application does not necessitate this angle-dependent characteristic, it is advisable to minimize the thickness of the top metallic layer and opt for a material with a higher refractive index. Moreover, to enhance the color purity and improve the brightness, a feasible way is to increase the quality factor to narrow the peak (dip) width.

It is noteworthy that through an elaborate choice of lossy material and designing of dielectric spacer thickness, broadband absorption can be obtained, resulting in a black appearance, which is unattainable for PC[107]. Recently, the F-P cavity has been widely extended in many fields rather than only for structural color generation, especially F-P cavity-enhanced electrochromism which successfully achieves the combination of structural color and pigment color[108–111]. Therefore, due to the simple configuration and easy fabrication, the F-P resonance cavity enables the generation of structural color more easily. The possibility of high internal stress of film can be greatly reduced when compared with 1D PC, even though using the same fabrication method (magnetron sputtering or electron-beam evaporation), because of the reduction of layer numbers.

2D structural color

2D colloidal crystal

Colloidal crystals can self-assemble into a 2D hexagonal array with high periodicity and densely closely packed characteristic. Of various nanosphere diameters and refractive indices of colloidal crystal, it exhibits different diffraction and scattering behaviors. The 2D colloidal crystal can be seen as a kind of grating-film combination, the diffraction structural color can be explained by interference theory and Bragg's law:

$$m\lambda_0 = 2Dn_{\rm eff}\cos\theta_{\rm b}(m=1,2,\cdots)\ , \tag{12}$$

$$m\lambda_0 = dn\left(\sin\theta_{\rm i}+\sin\theta_{\rm m}\right)(m=1,2,\cdots)\ , \tag{13}$$

where $\theta_{\rm b}$ is the refraction angle of light in the thin film (nanospheres in line can be equivalent to a thin film); D and $n_{\rm eff}$ are the equivalent thickness of the thin film and refractive index; d refers to the distance between two adjacent particles; n is the refractive index of particles; $\theta_{\rm i}$ and $\theta_{\rm m}$ are the incident and reflection angle, respectively. m and λ_0 are the diffraction order and wavelength.

However, light beams are not only diffracted and scattered toward all directions but also transmitted through the monolayer nanosphere arrays, resulting in low brightness and intensity observed by the eyes. To counteract this and enhance the observed brightness and intensity of the diffracted and reflected light, it is beneficial to employ strategies such as utilizing a high collimation beam (under sunshine), or a black background (substrate), which helps in maximizing the contrast and visibility of structural color[112,113]. Compared to the above-mentioned structural color generation platforms, colloidal crystal has outstanding low-cost and large-scale potential, which can be fabricated by air-liquid interface self-assembly, spin coating, and micro-propulsive injection method[114–116]. Among these, air-liquid interface self-assembly is particularly efficient for producing high-quality 2D colloidal crystals. The process involves hydrophobic colloidal particles settling on an aqueous solution's surface, where they spread due to the water's higher surface tension. To achieve a perfect monolayer PC, it is crucial to carefully increase the spreading fraction of the colloidal particles on the water's surface and to utilize surfactants to improve the uniformity of the colloidal array. Subsequently, the colloidal array can be meticulously transferred onto the target sample by the careful removal of excess liquid.

Metasurface

The engineering of metasurface architectures predominantly concentrates on augmenting the inter-coupling gain between adjacent elements, meticulously calibrating the thickness of the dielectric layers, and achieving optimal impedance matching. Theoretical frameworks like multi-wavelength interference, effective medium theory, and plasmonic resonance have been instrumental in guiding the geometric optimization of these structures. This theoretical groundwork plays a pivotal role in the precise control of the structural coloration, significantly enhancing the color vividness and resolution. To evaluate the reflection R and transmission T under incident light, the square of reflection and transmission coefficients equal to them respectively[73,117].

$$R = S^2_{11} = \frac{\frac{\mathrm{i}}{2}\left(\frac{1}{Z_\mathrm{r}} - Z_\mathrm{r}\right)\sin\left(nk_0p\right)}{\cos\left(nk_0p\right) - \frac{\mathrm{i}}{2}\left(\frac{1}{Z_\mathrm{r}} + Z_r\right)\sin\left(nk_0p\right)}, \quad (14)$$

$$T = S^2_{21} = \frac{1}{\cos\left(nk_0p\right) - \frac{\mathrm{i}}{2}\left(\frac{1}{Z_\mathrm{r}} + Z_\mathrm{r}\right)\sin\left(nk_0p\right)}, \quad (15)$$

where k_0=ω/c represents the vacuum wave vector; $n = \sqrt{\varepsilon_{\mathrm{eff}}\mu_{\mathrm{eff}}}$ is complex refractive index and $Z_\mathrm{r} = \sqrt{\mu_{\mathrm{eff}}/\varepsilon_{\mathrm{eff}}}$ is complex impedance. ω, $\varepsilon_{\mathrm{eff}}$, μ_{eff}, p and c are angular frequency, effective permittivity, effective permeability, dielectric thickness and speed of light in vacuum respectively. The analysis and quantitative calculation are difficult for metasurface, so researchers often resort to finite element software to optimize unit structures.

The fabrication of metasurface seriously relies on high-end equipment, including FIB, EBL and nanoimprinting which can ensure high accuracy of periodic structure. Consequently, while metasurface offers superior structural color with exceptional resolution, brightness, accuracy, and color gamut, it is imperative to weigh their cost-effectiveness against the value they provide in specific applications.

3D colloidal crystal

Colloidal nanoparticles can be well dispersed in numerous solvents, e.g., ethoxylated trimethylolpropane triacrylate, 1,2-dichlorobenzene, water, etc[118]. The electrostatic repulsive forces between two neighboring nanoparticles promote the formation of colloidal crystals as the existence of shearing. The interparticle interaction (F) can be described through Coulomb's Law[20,119–121]:

$$F = \frac{1}{4\pi\varepsilon_0\varepsilon_\mathrm{r}} \cdot \frac{q_1q_2}{d^2}, \quad (16)$$

where q_1 and q_2 denote the charges of two neighboring colloidal crystal nanoparticles; ε_0 and ε_r are the permittivity of free space and relative permittivity, respectively; d is the distance of two neighboring nanoparticles. Once the dispersed nanoparticles reach a suitable volume fraction, uniform and high-regularity 3D colloidal crystal arrays form spontaneously[122,123]. The structural color generation can be attributed to PBG, and its position significantly influences color exhibition. The center wavelength λ_0 of PBG can be calculated as

$$\lambda_0 = 2dn_{\mathrm{eff}} = \left(\frac{\pi}{3\sqrt{2}\phi}\right)^{1/3}\left(\frac{8}{3}\right)^{1/2} \cdot D\left(n^2_{\mathrm{sphere}}\,\phi + {n_{\mathrm{solvent}}}^2(1-\phi)\right)^{1/2}, \quad (17)$$

where n_{eff} is the effective refractive index of the whole structure including colloidal crystal nanoparticles and surrounding solvents; n_{sphere} and n_{solvent} are corresponding refractive indices of colloidal crystal and surrounding solvent. According to Bragg's Law, the distance of face-centered cubic (FCC) lattices' (111) plane can be described by D and ϕ which are nanoparticle diameter and packing fraction of FCC lattices (ϕ=0.74) as presented in the right part of Eq. (17).

Hence, the modulation of nanoparticle diameter and the refractive indices of themselves as well as the solvent can control the final color exactly. It is particularly noteworthy that a higher contrast ratio between the colloidal crystal and the solvent results in greater reflectivity intensity. Therefore, core/shell and hollow nanoparticles are synthesized to improve color brightness and impart the device's excellent performance[77,124,125]. The typical schematic illustration of a 3D colloidal crystal PC is shown in (Fig. 2(d)), and it is also called an opal structure. A critical aspect of the fabrication process is to prevent defects and cracks in the colloidal crystal arrays, as these can lead to color impurities. The capillary force, acting as an external driving force, is often utilized to induce the self-assembly of colloidal crystal nanoparticles and achieve homogeneous colloidal crystal arrays. This process is due to the asynchronous progression of the solid-liquid-air interface as it descends into the solvent, which in turn triggers the formation of a meniscus at the substrate surface where the colloidal crystal films are formed. After the evaporation of solvent, multilayer colloidal crystal films are attached to the substrate tightly.

Dip-coating as an improved way based on such a

mechanism can obtain homogenous colloidal crystal film more efficiently and quickly than vertical convection deposition[77,126,127]. There are also some other ways to construct 3D colloidal crystals with high efficiency and low cost, e.g., spray coating, micro-propulsive injection method under the assistance of the Marangoni effect, and blade coating[87,114,128–130].

In conclusion, these coloration strategies, which harness distinct light-matter interactions to elicit structural color, each possess unique design parameters for controlling specific colors (Table 2). At the application stage, a judicious consideration of their respective advantages and disadvantages can lead to the optimization of performance and the formulation of effective design guidelines.

Applications

Anti-counterfeiting

Information security is highly emphasized in the era of informatization. Therefore, how to encrypt information with more channels from different aspects at the same time, and in turn, making decryption and replication difficult, poses a formidable challenge[131]. Traditionally, complex patterns or long sequences of disordered numbers are extensively applied, but the possibility of being decoded remains high. Structural color, correlating to precisely designed parameters, is an ideal candidate for anti-counterfeiting, possessing controllable, angle-dependent color with long-term stability, high flexible pattern manufacturability and transferability[132–134]. Usually, a structural color anti-counterfeiting device should at least possess one of the following characteristics: 1) can present more than one kind of patterns with different polarization conditions; 2) can present specific colors under certain excitation or directions; 3) the invisible patterns or information can show up through preconcerted process; 4) structural color information can be made through transparent raw materials.

Static PC encryption

One of the typical characteristics of structural color is its sensitivity to light fields, such as angle-dependence, polarization-dependence, and scattering/diffraction-dependence. Therefore, static PC encryption devices can offer reliable information security without other complex assistance.

The selection of fabrication method significantly influences the commercial viability and functional attributes of structural color devices in anti-counterfeiting applications. The bottom-up approach, predominantly relying on chemical synthesis and subsequent self-assembly or straightforward physical techniques, constructs structural colors with limited precision due to minimal human intervention. This method's encryption capabilities are primarily realized through pattern complexity and the flexibility to transfer onto various substrates, offering a wide application scope[135,136]. However, it falls short in environmental durability and color saturation, leading to less effective encryption[137].

Conversely, the top-down method excels in the designability of periodic structures, ranging from 1D to 3D, with the potential to predict the color presentation and physical properties of structural colors through finite element simulation. Crucially, this method leverages sophisticated micro- and nanofabrication techniques to achieve more intricate and adaptable color combinations and a richer array of patterns, outperforming the bottom-up approach in precision and versatility. These characteristics render the top-down method more suitable for high-performance encryption applications, where durability and visual authentication are paramount. Generally, the top-down fabrication method holds promise, with numerous emerging strategies aimed at streamlining the process and endowing more functions. However, the bottom-up approach is often more desirable in static PC encryption due to its economic advantages.

Table 2 | A summary of different coloration mechanisms.

Classification	Dimension	Disadvantages	Advantages	Physics parameters
PC	1D	Wide FWHM	Feasible design, highly controllable, algorithm assisted, and simple	R, λ_0
	2D	Limited material selection and fabrication method	Precise control of color	λ_0
	3D	Low peak intensity		
F-P cavity	1D	More than one resonance absorption peak	Feasible design, highly controllable, and simple	R
Quasi-periodic PC	1D	Complex calculation for color customization	High design freedom	R,T
Metasurface	2D	Ultra-complex calculation for color customization	Ultra-precise control of color	R, T

1D PCs with alternate refractive index layers could form PBG and be easily designed using TMM. The stacked multilayered photonic system is sensitive to thickness variation, viewing angle difference, and the arrangement order for structural color presentation[138,139]. Consequently, information and colors can be selectively tuned by changing these parameters[140]. In general, 1D PCs possess fewer encoding manners and information-carrying channels, which results in lower reliability in anti-counterfeiting. 3D PC offers additional factors for tuning PBG, including factors such as nanoparticle size, lattice constant, and refractive index contrast between background and nanoparticles, and could also be combined with other responsive materials or serve as templates for further modification[141–143]. In this case, colloidal crystals PC which provides a fast and cost-effective way for anti-counterfeiting has been widely studied.

Traditional assembly techniques such as spin-coating, vertical convective self-assembly, and spray-coating can be used to form multilayered colloidal crystals, without the need for complex instruments or physical and chemical assistance. However, by carefully controlling the assembly interface between the substrate and the nanoparticle suspension, it is possible to create a monolayer PC due to the Marangoni effect, which is a type of 2D PC[30,84,114]. The planar self-assembly monolayer PC has fewer cracks and defects than the 3D PC, but exhibits relatively weaker color performance. Consequently, whether 2D or 3D PC, their advantages are more evident than those of 1D PC.

Most anti-counterfeiting PCs are combined with polymers as soft and flexible tags. 3D PC anti-counterfeiting patterns could be attached to virtually any substrates, making them promising candidates for anti-counterfeiting, although certain challenges and obstacles need to be addressed. First, light scattering occurs between neighboring nanoparticles, which decreases color saturation and brightness, meanwhile, the reflected and transmitted light would also be suppressed[144,145]. This outcome is undesirable in the anti-counterfeiting field, where distinguishability is crucial. Second, increasing the refractive index contrast leads to low transparency while maintaining high brightness, yet decreasing it will result in the opposite outcomes[23,30,124,146]. Consequently, when applying them to anti-counterfeiting tags, the balance between color brightness and transparency should be considered in advance.

Multiplexed anti-counterfeiting involves the use of multiple channels to encrypt information, which is challenging to achieve solely using self-assembled PCs. To address this, Lai et al. proposed an encoding platform that utilizes the nanoimprinting technique to create hexagonal micro-shallow pits on a self-assembled polystyrene (PS) substrate (Fig. 3(a))[30]. This periodic nanostructure provides three independent channels for presenting different information: scattering mode, reflection mode, and polarization mode. Interestingly, the authors demonstrated the practical application of this platform in cryptographic QR codes and security labels. By changing the incident light direction and rotating the polarization angle of the polarizer, both the QR codes and security labels can reveal three different hidden items of information. In addition, numerous studies have successfully illustrated the potential of 3D PCs for anti-counterfeiting in banknotes, commodities, and a range of high-value objects (Fig. 3(b–e))[52,147–150].

In the future, the encrypted information based on structural color can be combined with Internet of Things (IOT), with specific software employed to decipher the information encoded within the structural colors. For instance, by endowing existing QR codes with structural color characteristics, it is possible to augment the dimensionality of information storage, thereby enhancing the security and reliability of the information.

Responsive PC anti-counterfeiting

Indeed, stimuli-responsive platforms or devices for PC encoding present greater challenges for counterfeiting when compared to static counterparts. While static anti-counterfeiting devices rely on their intrinsic physical properties to exhibit different states, responsive devices require specific external stimuli to reveal hidden information[151]. For example, Ma et al. employed a spin-coating technique to create patterned films using alternating layers of TiO_2 nanoparticles and PMMA layers[66]. These films exhibited reversible color switching between yellow-green and orange when subjected to solution penetration and elimination. Importantly, the observed colors also displayed strong angle-dependence, adding the degree of information complexity (Fig. 4(a)). Fang et al. introduced a fascinating application of 3D colloidal systems through their "cold" programming shape-memory PCs (Fig. 4(b))[50]. They achieved this by initially constructing silica colloidal templates and subsequently infiltrating them with copolymers of ethoxylated trimethylolpropane triacrylate and poly (ethylene glycol)

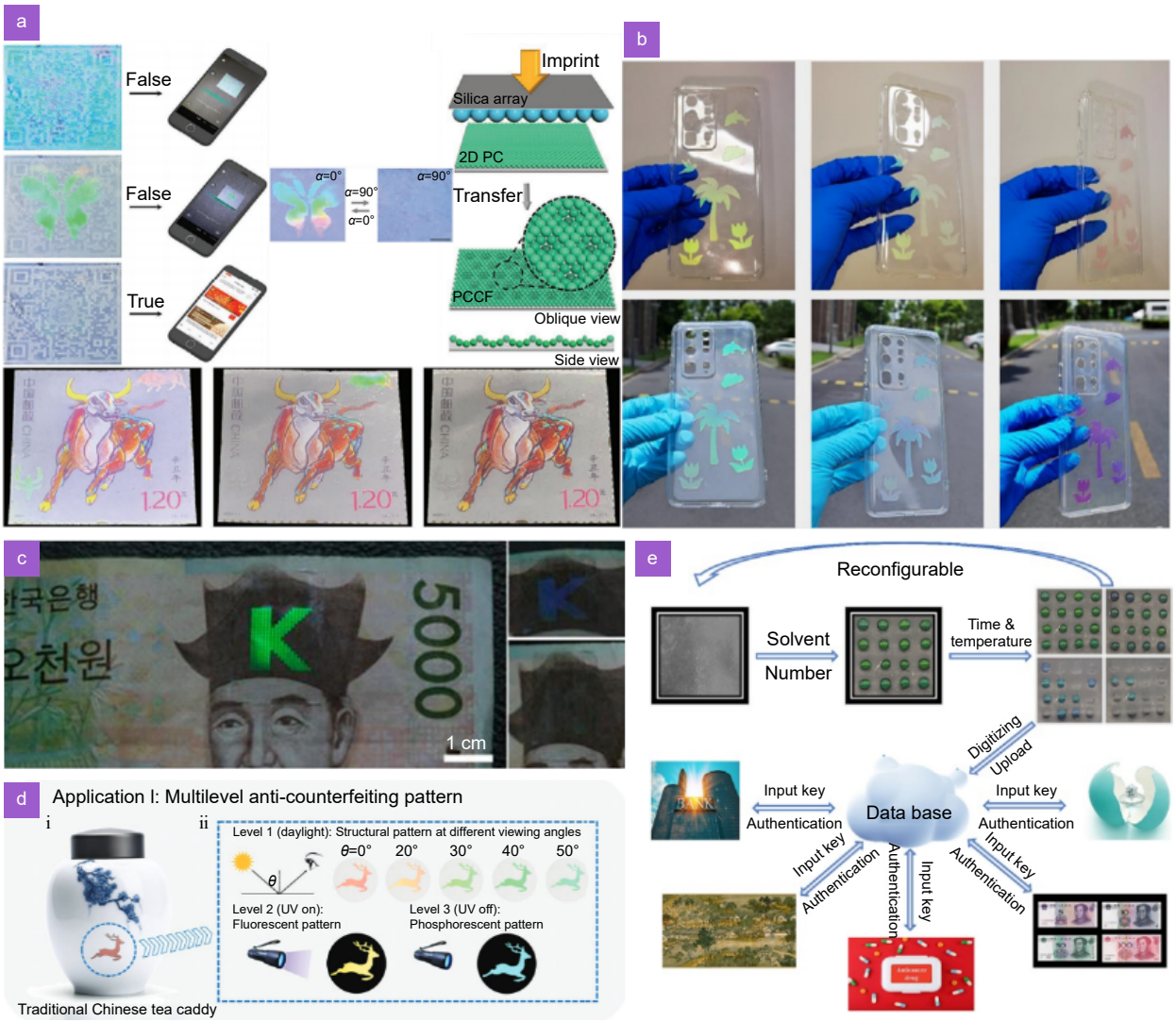

Fig. 3 | Static PC encryption. (**a**) Schematic of the processes for the fabrication of photonic crystal composite film (PCCF) and schematic illustrations showing encryption and recognition of the paper-printed QR code and stamps encoded by PCCF. (**b**) Multiangle photochromism (indoors and outdoors) effect of the functional PC films with different patterns on the phone case. (**c**) The patterned photonic crystal film on a Korean banknote. (**d**) Anti-counterfeiting pattern displayed at different viewing angle on a traditional Chinese tea caddy. (**e**) A multi-industry applicable optical anti-counterfeiting system with higher security level and fast identification and decryption process of the PC. Figure reproduced with permission from: (a) ref.[30] , John Wiley and Sons; (b) ref.[148], American Chemical Society; (c) ref.[147], American Chemical Society; (d) ref.[149], John Wiley and Sons; (e) ref.[150], Elsevier.

diacrylate (PEGDA). By removing the templates using a hydrofluoric acid wash, macroporous films were obtained. The responsive mechanism is attributed to capillary pressure, enabling recovery from pressing-induced deformations through a pull-off force. Moreover, it is compatible with hydrogels, polar solvents, and shape-memory polymers and can be particularly modified with magnetic nanoparticles[51,152–154]. For instance, Huang et al. developed a rewritable decoding paper, which allows real-time information display using a "NIR laser pencil" on the PC flexible films (Fig. 4(c))[155]. Most importantly, when the paper cools down to room temperature, the written information disappears simultaneously because of the shrinkage effect of thermosensitive thin film, which leads to a reduction in the lattice spacing within the PC.

Lai et al. reported a 2D PC kirigami, which can endure 10000 cycles of stretching and releasing without obvious attenuation. The periodic flap gates underwent out-of-plane deformation as the strain increased, exhibiting evidently angle-dependent color change. The authors also realized programmable control of information

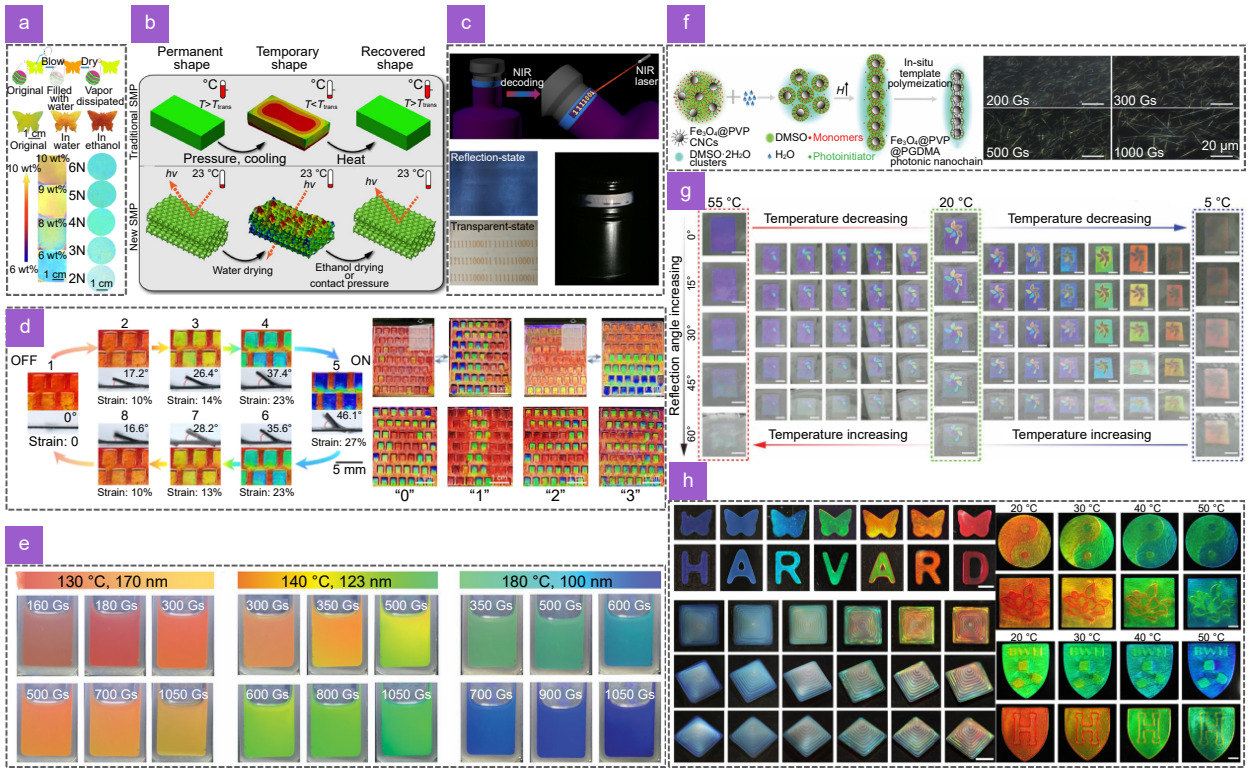

Fig. 4 | Responsive PC anti-counterfeiting. (**a**) Schematic diagram of flexible 1D PC butterfly patterns in the process of blowing and drying. (**b**) The nanoscopic recovery and deformation process of the permanent 3D photonic crystal structure stimulated by drying the sample out of ethanol or applying an external contact pressure. (**c**) Schematic diagram of the information decoding process of thermosensitive structural colored labels. (**d**) Color switching of the bioinspired PC-PDMS kirigami under uniaxial tension and its programmable application. States 1–5 are the loading steps during which the gates lift and the color changes from red to blue. States 5–8 are the unloading process. The colors return to the same value as those during the loading process when the lifting angles of gate arrays return to the original state. (**e**) Magnetically responsive structural colors under different *H*. (**f**) Schematic illustration for the fabrication process of Fe_3O_4@PVP@PGDMA PNCs via a selective concentration polymerization of monomers in microheterogenous dimethyl sulfoxide–water (DMSO–H_2O) binary solvents and its anti-counterfeiting application. (**g**) Digital photographs of the prepared multiplexed patterned thermochromic photonic film soaked in water with different temperatures and viewed at different reflection angles. (**h**) Digital photographs of the printed 2D non-close-packed and 3D non-close-packed pyramids patterns with different colors and time-difference-printed tunable-multicolor patterns using inks with different structural colors. Figure reproduced with permission from: (a) ref.[66], American Chemical Society; (b) ref.[50], Springer Nature; (c) ref.[155], American Chemical Society; (d) ref.[84], John Wiley and Sons; (e) ref.[51], John Wiley and Sons; (f) ref.[52], John Wiley and Sons; (g) ref.[77], John Wiley and Sons; (h) ref.[94], Elsevier.

display with different thicknesses and lifting angles (Fig. 4(d))[84]. Furthermore, magnetic Fe_3O_4 nanoparticles can serve as the core in core/shell nanostructure, offering magnetic responsiveness[51,52,153,154,156]. Under the influence of magnetic fields, these nanoparticles can form long, ordered chain-like nanostructures, with the direction of the chains influencing the color display (Fig. 4(e) and 4(f)).

Magnetically responsive PCs provide a contactless method for color manipulation, offering significant advantages over traditional techniques. Additionally, other non-contact methods like solution infiltration, pressure, and vapor offer viable alternatives for creating responsive anti-counterfeiting features[78,157]. The use of phase transition materials represents another promising direction, enabling contactless control through temperature regulation[158–160]. Their electromagnetic parameters will change after heating up to phase transition temperature, thus leading to a switch between dielectric and metallic state. Integrating such materials within F-P cavities or multilayer structures allows for reversible color tuning of the structure.

Hydrogels like poly (N-isopropylacrylamide) (PNIPAM) and PEGDA offer another intriguing property-they can swell or shrink in response to cycles of heating and cooling (Fig. 4(g))[77,94,161]. Based on this property, the lattice constant of colloidal PCs will increase or decrease accordingly, and the reflection color will change in terms of the shift of the reflectance peak. Therefore, a

combination of bottom-up and top-down methods is highly demanded to complement each other. To this end, the assistance of 3D printing becomes valuable[94,162]. Liao et al. dispersed highly charged elastic nanoparticles (HENPs) in a cross-linkable PEGDA composite solution to create printable ink, which successfully reached the control of structural colors from microscale to macroscale simultaneously (Fig. 4(h))[94]. The ability to print arbitrary 3D structures with a wide range of temperature-responsive behavior across the entire spectral range significantly expands the dimensions of anti-counterfeiting measures, making the resulting PCs more secure and reliable.

While these responsive PC anti-counterfeiting patterns exhibit extraordinary performance in information security, they cannot endure a sufficient number of stability cycles. At the end of each cycle, nanostructures will suffer irreversible damage resulting in performance deterioration[163–165]. In the cycling process, the modulation of interstitial spacing within the units responsible for generating structural colors results in the shifting of reflection peaks[166,167]. This responsive mechanism inevitably induces dislocations and slips, causing the constituent structures to progressively deviate from their initial positions. The accumulation of such tendencies leads to an impaired response to normal excitation, thereby constraining the regulation of interstitial gaps. The primary mode of failure in responsive PC stems from the matrix itself. For example, thermo-responsive PC, which mainly rely on hydrogel matrixes, are susceptible to failure due to high glass transition temperatures, exacerbated by liquid evaporation and the degradation of the internal cross-linked network. In the case of magnetically responsive PC devices, the progression towards disorder and the cumulative effect of irreversible responses ultimately lead to the loss of functionality.

In order to enhance the cycling stability of responsive PC, which is the barrier for long-term practical application, researchers focus on optimization of matrix for endurability[168–170], reducing lattice distortion[171], and suppressing structure collapse[171]. Selecting a matrix capable of withstanding the stresses inherent in responsive conditions and preserving system stability is essential for prolonging the shelf-life of these devices. The use of matrices with low glass transition temperatures, such as copolymer in thermos-responsive PC is a proven strategy for achieving optimal cycling performance, thereby ensuring the enduring functionality and reliability of responsive photonic crystals[77,172]. In the domain of mechanically responsive PC devices, PDMS[173] and poly(ethylene glycol) phenyl ether acrylate (PEGPEA)[174,175] are commonly utilized as matrix materials due to their exceptional resilience and durability. These properties enable the maintenance of stable elastic strains and the reduction of fatigue damage, which are critical for enhancing the operational lifespan of responsive PCs. Moreover, self-healing properties, facilitated by hydrogen-bond-rich hydrogels, are essential for improving cycling stability[176–178].

Overall, responsive PCs excel over static counterparts in security, benefiting from their enhanced complexity in counterfeit data, more robust encryption techniques, and increased difficulty in replication. Furthermore, by incorporating multimodal anti-counterfeiting strategies[179,180], self-destructive characteristics[181] and luminescent materials[182–184], the dimensionality of encrypted information can be significantly broadened, offering a more secure and versatile approach in the field of anti-counterfeiting technologies. Additionally, a significant advantage of responsive PCs is their compatibility with intelligent software and system integration, aligning more closely with the trend towards future intelligent development[185,186].

It is noteworthy that 4D printing, an emerging technology in recent years, has the potential to transcend the non-dynamic and non-adjustable characteristics of traditional 3D printing[187,188]. The inherent dynamic regulation capabilities of the printing materials are precisely what the display of structural colors aspires to achieve. The integration of these two technologies holds significant potential and could usher in new opportunities for the development of structural colors.

Multi-modes metasurfaces

Anti-counterfeiting devices based on metasurfaces bear a wide range of choices in terms of materials and patterns, including all-dielectric, metal, and hybrid metasurfaces as well as asymmetric, symmetric, and chiral patterns[189–193]. While it may take time for metasurface devices to become integrated into daily life and achieve large-scale utilization, recent developments in grating-type and cross-like pixel arrays have shown as an intriguing avenue to achieve polarization-switchable color displays, making the cloning of specific images unattainable (Fig. 5(a) and 5(b))[31,92]. The essence is to break the symmetric system, constructing asymmetric geometries in

the *X*-*Y* plane to induce different light-matter interactions for different polarization states.

The asymmetrical geometry introduces an inherent anisotropy into the system, allowing for polarization-dependent light scattering or absorption, which leads to different resonance conditions or scattering mechanisms for different polarizations, resulting in distinct colors or optical responses. For instance, by inducing and suppressing magnetic dipole (MD) resonance under different polarization modes, a bird and a fish can alternatively appear based on the all-dielectric Si_3N_4 nanorods metasurface (Fig. 5(c))[64]. Additionally, two different images can be displayed in the same area without the crosstalk effect through a combination of nanocrosses and nanorods. The high saturation and brightness characteristics of sharp and narrow reflectance peaks approach almost 1 in both "on" and "off" states. There are many researchers dedicated to manipulating light with more degrees of freedom, as well as separately achieving versatility on a single cell under the assistance of photolithography[194,195]. In this case, phase-modulated metahologram and structural color nanoprint would be obtained at the same time, contributing to higher information density[28,196–199]. The plane contains nano-building blocks with a series of carefully designed specific rotation angles to generate angle-dependent Doppler shifts,

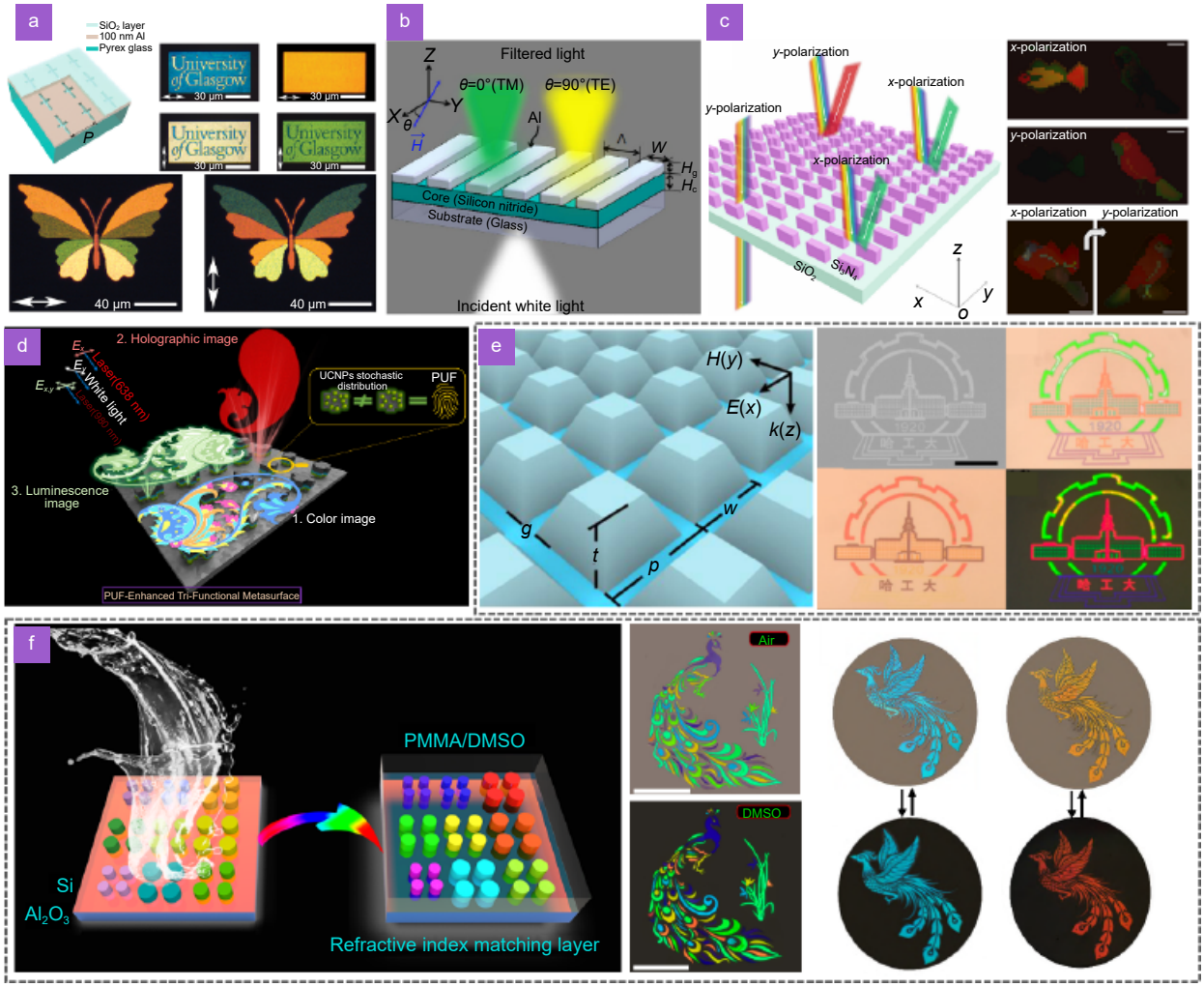

Fig. 5 | Multi-modes metasurfaces for anti-counterfeiting. (**a**) Schemes of aperture geometry and arrangement and microscopic images with dual color information states "printed" with nanoscale resolution. (**b**) Schematic configuration of the proposed color filter where the incident white light is filtered into different colors depending on the polarization. (**c**) Bright field optical images of the "fish and bird" comprising nanorods under *x*- and *y*-polarized light. (**d**) Schematic illustration of the tri-functional metasurface integrating a color print, hologram, and luminescence image by controlling amplitude, phase, and luminescence properties. (**e**) Full color image printing with TiO_2 metasurfaces. (**f**) The optical microscope images of phoenix with different colors in the air and DMSO. Figure reproduced with permission from: (a) ref.[31], American Chemical Society; (b) ref.[92], Springer Nature; (c) ref.[64], American Chemical Society; (d) ref.[133], Elsevier; (e) ref.[200], American Chemical Society; (f) ref.[36], Springer Nature.

thus geometric phase differences can be observed. This novel paradigm underpins metasurfaces for wider application. Rezaei et al. fabricated a metasurface using cross-shaped nanounits, which consisted of a layer of SiO_2 film sandwiched between Al films (Fig. 5(d))[133]. The metasurface employs anisotropic gap-plasmon resonance, thereby enabling support for multi-channel information security. This advanced design allows for the seamless integration of holographic, color, and luminescent images within a single device. Notably, the color images displayed exhibit a pronounced polarization dependence, offering an additional layer of security.

Technically, the guided mode resonance effect, which is stimulated by gratings is produced by coupling resonance between diffraction and leaked modes[201]. This effect leads to a narrower spectral bandwidth (smaller full width at half maximum or FWHM) and high diffraction efficiency with polarization sensitivity. Additionally, it is a cost-effective approach compared to other techniques[202,203]. The incorporation of subwavelength pixel arrays enables the encoding of more intricate details. In essence, metasurfaces provide robust information security, capable of rendering subtle cues and warehousing high-density optical information[35,204,205].

In constructing anti-counterfeiting metasurfaces based on the coupling effect of Mie resonances, TiO_2 has been used as the building block more frequently (Fig. 5(e))[89,200,206]. TiO_2 is preferred over Si metasurfaces in the visible regime due to its lower intrinsic loss. However, Yang et al. creatively proposed an extremely thin Si metasurface coated with a refractive index matching layer, polymethyl methacrylate (PMMA) or dimethyl sulfoxide (DMSO), which effectively suppresses unnecessary reflection both inside and outside the main peak without significant loss[36]. In addition, the Si metasurface is fabricated using EBL and reactive ion etching with a minimum pixel size of 190 nm, the resultant metasurface can approach the diffraction limit with a spatial resolution of around 10^5 dpi due to the high refractive index of Si. Thus, the poor color performance and pale appearance when it is exposed to air can be overcome and the gamut area can be extended to 181.5% of sRGB. As proof of its anti-counterfeiting application, the vibrant and distinct image of the "phoenix" and its lifeless counterpart can be dynamically switched with the fast response with or without DMSO infiltration (Fig. 5(f)).

Metasurfaces possess a higher degree of freedom and flexibility in processing, and by optimizing the parameters and arrangement of unit structures, they can precisely tailor optical response characteristics to achieve controllable design of amplitude, phase, polarization, and more[207–211]. Currently, the design methods of metasurfaces that rely on machine learning and artificial intelligence have greatly enhanced the design chain from demand-driven and function-oriented to specific structures, providing a broad prospect for the development of structural colors.

Emerging anti-counterfeiting technology

The high-cost and time-consuming process of metasurface fabrication has been a major obstacle. Therefore, facile and cost-effective ways are highly expected. One ideal goal is to encrypt transparent materials into security carriers, where no structural color or information can be observed in the non-encrypted state but becomes visible under specific conditions after the encoding process.

Lapidas V. et al. have substantially enhanced the encoding capacity through direct laser printing without sacrificing high-resolution and environmental resistance (Fig. 6(a))[89]. The structural color is produced by light scattering and plasmonic resonance of Ag nanojet-nanoparticle ensembles, and the color is governed by the applied pulse energy. Quick response (QR) code is its typical anti-counterfeiting scenario, which can be precisely distinguished through algorithms and yet more unclonable. Similarly, Li et al. developed a kind of transparent polymer ink that is capable of printing in commercial inkjet through which structural colors can be largely and quickly produced with high resolution, such as elaborate portrait images (Fig. 6(b))[65]. The gamut, saturation, and brightness of the color can be preciously controlled by modifying the morphology of microdome structures through adjustments in the number of droplets or substrate wettability. Interestingly, the optical Janus property characterizes its rather unique anti-counterfeiting function in that the coloration can only be observed on one side of the panel due to total internal reflection (TIR)[212]. Though these methods exhibit great potential in preventing forgery at low cost, they are still inadequate to meet the increasing need for a trade-off between throughput and efficiency[186,213,214].

Nanoimprinting is a promising technique capable of fabricating on nearly all substrates and enabling unlimited replication using master samples. Hou et al. proposed a kirigami structure inspired by animals that can programmably switch colors[90]. Gratings are imprinted on

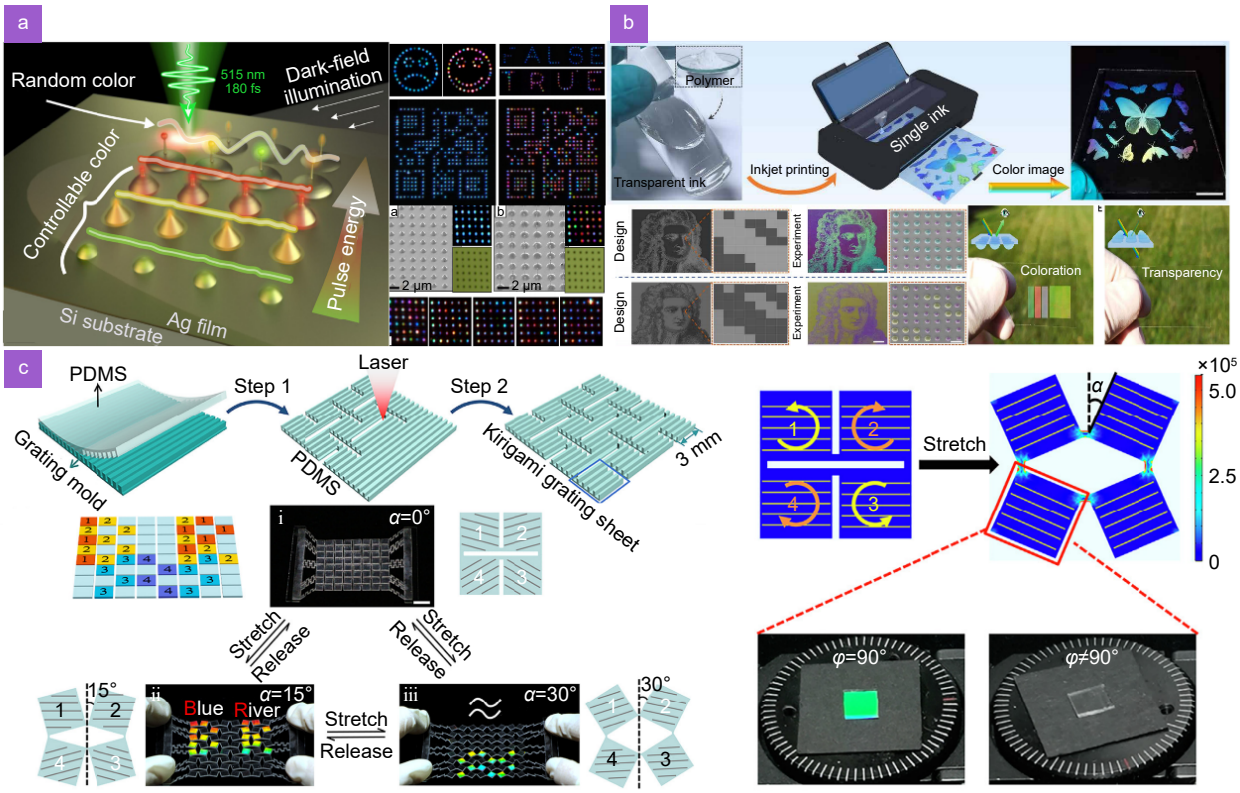

Fig. 6 | Emerging anti-counterfeiting technology. (**a**) Schematic illustration of Ag nanostructures fabrication and its dark-field printing. (**b**) The process of structural-color printing with a single transparent polymer ink and the optical Janus property of coloration and transparency of the printed structural-color panel viewing from the bare unpatterned (blank) side. (**c**) Schematic of the fabrication procedure of the kirigami grating sheet and grating patterns with different azimuth angles (illustrated by code patterns) and the process of reading encrypted patterns by stretching. Figure reproduced with permission from: (a) ref.[89], AIP Publishing; (b) ref.[65], AAAS; (c) ref.[90], Elsevier.

PDMS by nanoimprinting, followed by laser cutting to achieve flexibility and programmability. Through stretching, images and encrypted information could be displayed or hidden with specific colors arising from the diffraction of gratings. Nevertheless, the size of the pixel is far too big to support high resolution (Fig. 6(c)).

In summary, metasurfaces offer a high-resolution, versatile solution for anti-counterfeiting, enabling complex, tunable pattern fabrication. However, they face limitations such as substrate inflexibility, typically using Si wafers. Emerging technologies like direct laser printing, nanoimprinting, and TIR provide a fast and efficient alternative. While top-down methods are effective for anti-counterfeiting, bottom-up approaches like colloidal self-assembly for 3D PCs avoid expensive equipment and complex processing. Despite offering multifunctionality and flexibility, they suffer from lower resolution and control compared to top-down methods. The future lies in combining additive manufacturing with self-assembly for optimal results.

Display

Structural color provides an ideal strategy to exhibit colorful images and characters with high brightness, wide gamut, low cost, and vividness. As a static display platform, there are various coating films or planes developed for decorations or specific patterns based on structural color using reflection mode or transmission mode[57,86,215–217]. Moreover, E-books and displayers are harmful to our eyes[218], while structural color platforms are different from these devices, which present information in a more friendly way. The dynamic display of structural color, activated by an electric field, holds promise as a replacement for E-ink technology[219]. Furthermore, there is an urgent need for the development of structural color platforms that can be activated by magnetic fields and force fields, among others[93].

Static structural color decoration

Static structural color decoration primarily relies on the vivid, colorful, and rich hues presented by structural colors, making it suitable for decorative needs in various

areas such as daily life and architecture. In addition to devices that display only specific colors, patterned decorative devices overlap in functionality with printing. Therefore, the primary criterion for classification is determining which application the device is best suited for. Concerning static structural color, it is common to fabricate on a hard substrate, for example, a metasurface based on Si or metal substrate, F-P cavity, and 1D PC that consist of multilayers of dielectrics or metals[215].

Li et al. derived a series of formulations to evaluate multipole expansion and fabricated an α-Si nanodisk metasurface based on this theory[220]. The introduction of electric quadrupole and magnetic dipole significantly expands the color range, and decorative applications were also demonstrated (Fig. 7(a)). While metasurfaces allow for precise control of color through adjustments in the *X*-*Y* plane structure, the *Z*-axis direction poses an opportunity for achieving more vivid color by complete control of hue, saturation, and brightness. Notably, controlling dimensions in three directions using traditional methods poses difficulties due to their inherent limitations. FIB is limited by its large-scale manufacture possibility and lithography can hardly balance the cost of time and precision. A feasible way to tackle such

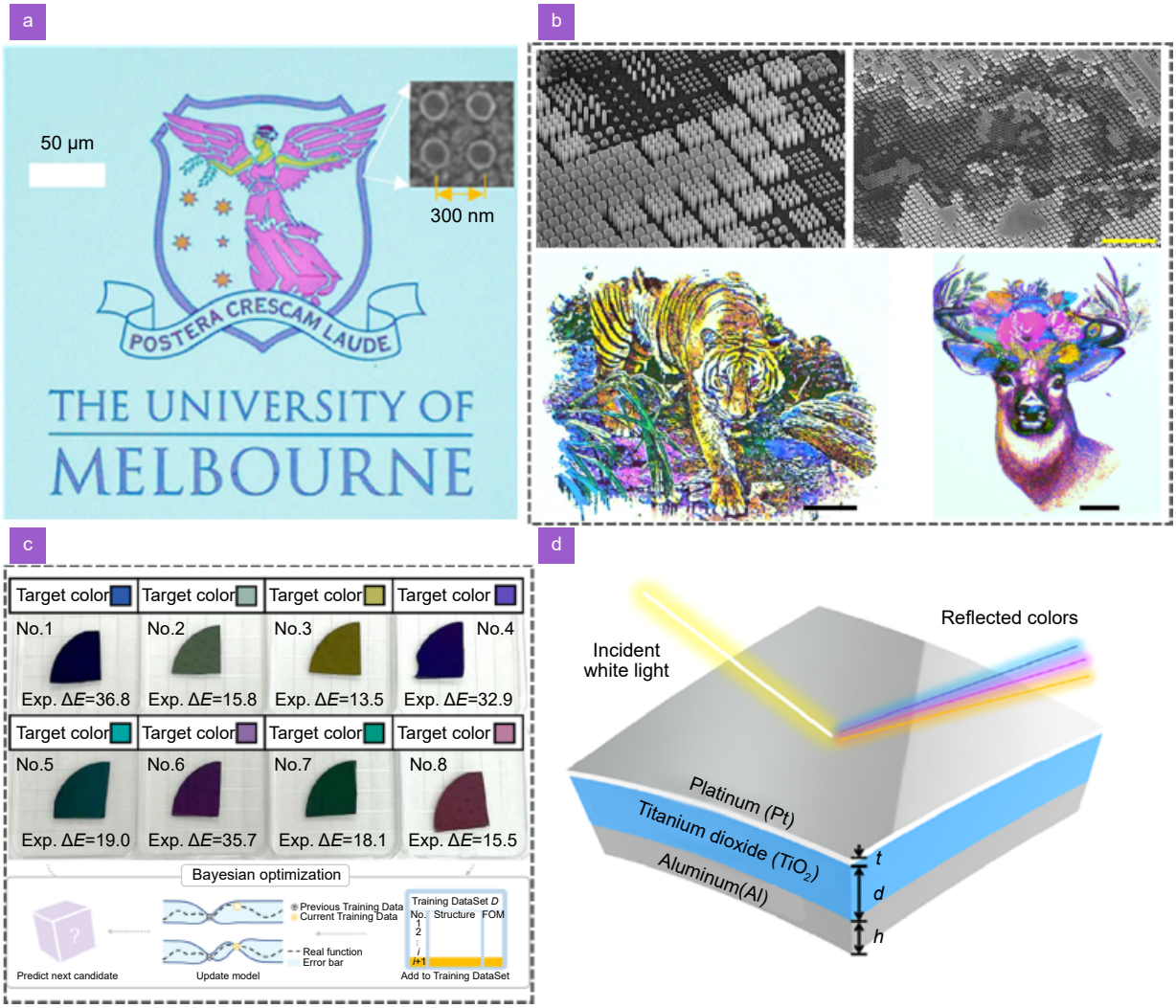

Fig. 7 | Static structural color decoration. (**a**) Optical microscope image of demonstration of color printing of institutional logo of authors of this paper. (**b**) Color reproduction ability of the structural color metasurface after introducing height regulation into *X*–*Y* plane: a comparison between the original picture and as-fabricated structural color metasurface including its optical micrograph and a large area SEM image and its details of the micro-pixels with real three-dimensions structure regulation in *X*–*Y*–*Z* directions. (**c**) Photographs showcasing the fabricated structures alongside their target color, fabricated color, and the respective color difference, denoted as Exp. Δ*E*; the Bayesian optimization process is presented below. (**d**) Proposed structure involving an asymmetric F−P nanocavity based on Al−TiO_2−Pt and measured (solid lines) and simulated (dashed lines) reflection spectra and the corresponding colors. Figure reproduced with permission from: (a) ref.[220], American Chemical Society; (b) ref.[221], John Wiley and Sons; (c) ref.[82], Springer Nature; (d) ref.[67], American Chemical Society.

challenges was proposed by Li et al.[221], they used grayscale assembled nanofabrication method based on EBL. Specifically, sacrificial layer is very important in the process. It acts as a template to determine the final structure. EBL provides the template pattern upon the sacrificial layer and TiO_2 was deposited on it by atomic layer deposition. The nanostructure is then transferred onto a quartz substrate, resulting in a metasurface with desired properties. It is worth noting that the resolution is ultrahigh (6.4×10^{10} dpi) (Fig. 7(b)). Metasurfaces are indeed advantageous, offering high resolution, a broad spectrum of colors, angle independence, and exceptional precision. However, they have not yet reached a stage suitable for large-scale applications. Consequently, structural colors based on multilayer systems have garnered significant interest. Despite this, their utility is currently confined primarily to simple structural color coatings or decorative applications, owing to the constraints of their limited designability. Hu et al. utilized a material informatics inverse design method to construct multilayer ZnS/Ge films, which proved more efficient than the empirical design (Fig. 7(c))[82]. Eight different color samples were fabricated, all of which closely matched their target colors, as observed by the naked eye and confirmed through reflectivity spectra analysis, regardless of viewing angle. Owing to the phase shift of a F-P cavity, a dielectric layer sandwiched by two metallic layers, its structural color is highly dependent on the viewing angle which originates from the difference in effective light path (Fig. 7(d))[67]. To solve these disadvantages, multilayer systems can be extended to incorporate more than two materials. By combining the coupling effect of different resonance cavities, phase compensation layers, and high-lossy absorption layers, performance improvements can be achieved[56,83,222,223].

Dynamic structural color display

These devices provide unique ways to display information, however, the low expansibility has not been solved yet. Similar to the fabrication method for hard substrate metasurfaces, periodic patterns can be transferred to flexible substrates, such as PDMS (Fig. 8(a))[224,225] or elastomeric photopolymers[226]. Apart from the costly process, the anodic aluminum oxide (AAO) template method, a type of soft lithography, can produce highly ordered hole arrays, allowing for easy replication of nanostructures on flexible substrates[227]. Due to the low tolerance for parameter variation of structural color, flexible structural color displays can tune the information or patterns through mechanical stimulation. However, this dynamic display strategy is transient and unstable. Although some indicators and smart tags require such a property, Lyu et al. used Mg as the top layer, and its color changes upon infiltration with water due to the removal of Mg, stable and reconfigurable characteristics are expected in most application scenarios[228].

PCs can be tuned under the excitation of voltage, with the shrinkage and swelling of the polymer, which influences the lattice distance and changes the structural color (Fig. 8(b) and 8(c))[80,229]. All-solid electrically tunable PCs usually require high voltage, and the inverse opal structure can efficiently lower the applied voltage. However, the low cycle life and poor color purity are far from the demand.

Colloidal PCs can be either positively or negatively charged. When applying voltage on the electrodes, the colloidal particles can move to the counter electrode under the drive of the electric field. In contrast to transient display devices, electrically responsive photonic crystals (ERPCs) are capable of sustaining their color state through the persistent application of voltage. This stable state is due to the balance between electrostatic force and applied electric force, and the reversible manipulation is attributed to lattice compression and expansion. Fu et al. synthesized CeO_2@SiO_2 PCs and dispersed them in propylene carbonate, successfully solving the large-scale requirement of nonsilica PCs with high crystallinity and a large dielectric contrast[46]. Dynamic display units with a 3×3 cell array were fabricated to verify the fast response speed from red to green, reversibility, and independent control potential (Fig. 8(d)). The polar solvent system needs a higher voltage to overcome Coulombic interaction, and thus it is more energy-consuming for prolonged operation, as well as producing electrochemical byproducts which can reduce cycle stability. Unfortunately, a weakly polar system is not beneficial for colloidal crystal self-assembly. Ge et al. proposed three ways to settle this difficulty: 1) Modifying SiO_2 colloidal crystals with hydrophobic functional groups to ensure good dispersion in weakly polar solvents. 2) Dispersing SiO_2 colloidal crystals in aniline, where Si–OH and $-NH_2$ groups can absorb each other to avoid particle agglomeration. 3) Adding an extra layer of Au, which can induce strong electric field confinement around the Au nanotips[20,47,48]. These methods are able to significantly reduce the voltage to below 2 V, although the response

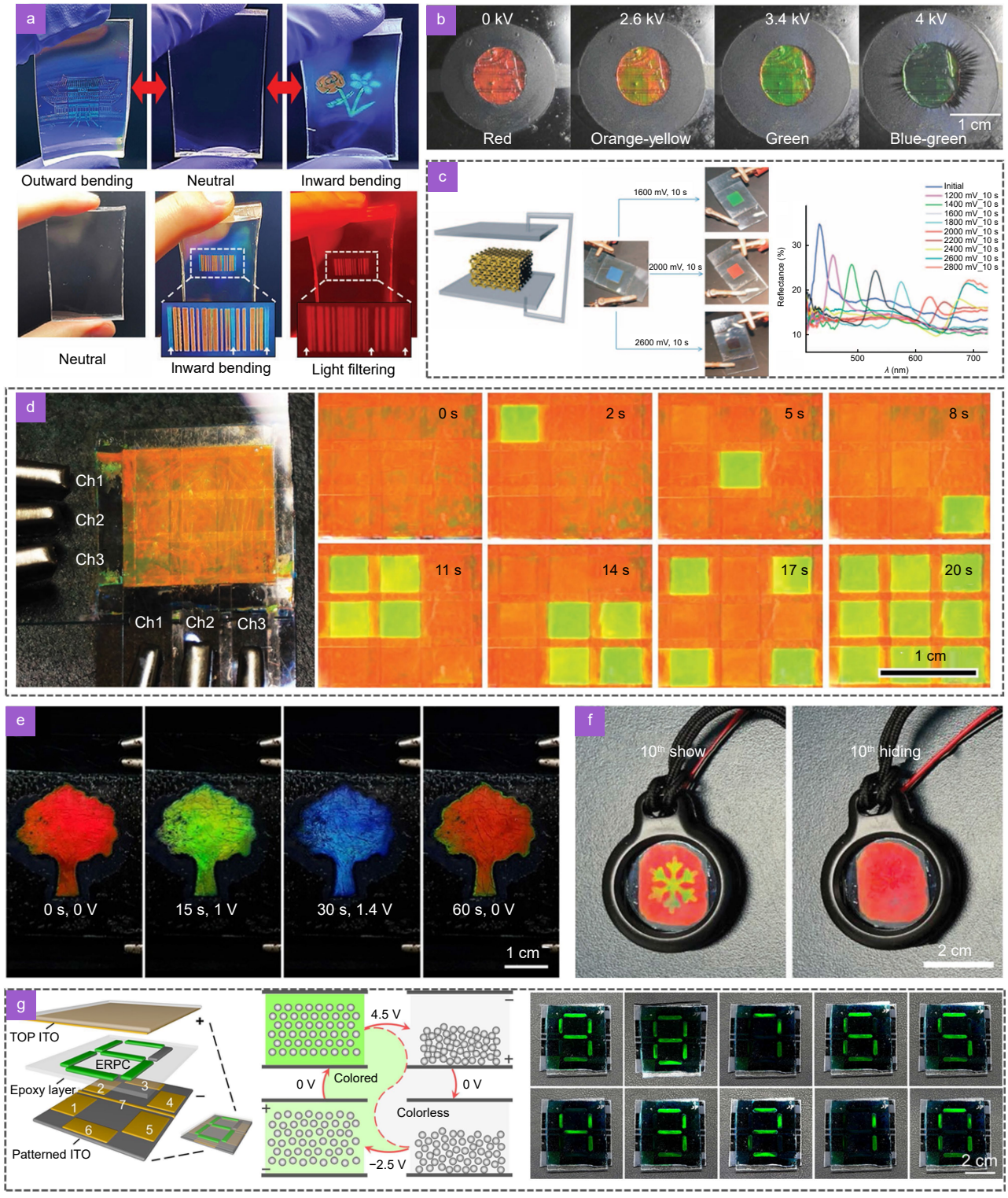

Fig. 8 | Dynamic structural color display. (**a**) Photographic images of two tri-layer films that were bonded together with their patterns facing forwards, illustrating how different patterns are revealed under outward and inward bending. (**b**) Active color changes according to the different fabrication methods and the applied electric potential. (**c**) Representation of the electrochemical cell fabricated for the electrical actuation of the active inverse opal and proof of full-color tuning by recorded spectra. (**d**) PC based display unit composed of 3 × 3-pixel cell array. (**e**) Photographs of the "tree" signage under different voltages. (**f**) Showing and hiding of the pattern in the 10th cycles. (**g**) Numerical indicator based on bistable electrically responsive photonic crystals. Figure reproduced with permission from: (a) ref.[225], John Wiley and Sons; (b) ref.[229], John Wiley and Sons; (c) ref.[80], John Wiley and Sons; (d) ref.[46], John Wiley and Sons; (e) ref.[47], Royal Society of Chemistry; (f) ref.[48], John Wiley and Sons; (g) ref.[21], Springer Nature.

speed is slower than that in polar solvents (Fig. 8(e) and 8(f)).

Moreover, cycle instability remains a challenge for researchers due to the production of electrochemical byproducts in this system. Modifying the ITO electrodes with anion-exchange and proton-exchange membranes has been verified as an effective way to increase cycle numbers[230]. Although the color can cover almost the entire visible regime, maintaining a specific transition color is not possible, as the PCs cannot reach an equilibrium point in the metastable state. Fu et al. further improved the ERPC system by adding polyethylene glycol and ethylene glycol, serving both as a thickening agent and to improve electrostatic forces (Fig. 8(g))[21]. There is a trade-off between viscosity, charge improvement, and electric strength. The key is to balance the disorder speed, which highly depends on the voltage value, and the self-recovery speed controlled by the viscosity. This work achieves this balance in an ingenious and facile way by freezing the particles' Brownian motion, allowing the middle state to be maintained without the application of voltage. The application of a bistable display is demonstrated through a programmed numerical indicator. Moreover, the bistable PC, when combined with photocurable hydrogel[79], retains its utility in information display.

Magnetically tuned dynamic structural color display is another promising candidate, which can show structural color in a contactless way but is less controllable than electric responsive PCs[231–233]. This display approach has received relatively little attention from researchers for several reasons. Firstly, maintaining the transition state during the change of the magnetic field is more challenging. Secondly, it cannot be easily applied in a simple or highly integrated manner due to its intrinsic responsive mechanism. Thirdly, it is typically implemented in a liquid system, which limits its practical application[234,235]. However, the inclusion of magnetic nanocrystals in the system enhances the dielectric contrast, highlighting its advantages in producing bright colors, while also exhibiting an extremely fast response speed. Brush block copolymer (BBC), an emerging type of responsive PC[236], exhibits anisotropic properties and an ellipsoidal morphology. He and coworkers demonstrated its full-color display ability when Fe_3O_4 nanoparticles are attached to it[76].

In conclusion, structural color offers an efficient and eco-friendly method for displaying vibrant colors and information in both static and dynamic forms. It outperforms traditional pigments in applications requiring durability against water, scratches, and corrosion. Moreover, its adaptable manufacturing process supports a wide range of materials and structures, catering to diverse needs. The flexibility and dynamism of structural color enhance its suitability for smart devices like e-ink and adjustable tags, and its multiple responsive channels expand its potential for dynamic displays. While significant research progress has been made, practical applications are still emerging, indicating a promising future in various fields.

Sensors

In military, agriculture, medicine, and other fields, an indicator that is sensitive to a certain chemical substance, pH, temperature, force, and moisture is highly demanded[49,126,237,238]. Usually, traditional sensors indicate environmental conditions by digit numbers or alarms, which either require careful inspection or vogue value reminders. If there could be a kind of direct and vivid sensor, it would bring more convenience. Structural color generation depends on two aspects: geometry parameters and light. Although the principles of structural color generation have been widely and thoroughly studied, there is still great potential to explore concerning light and materials respectively. The relation of light-matter interaction occurs at the nanometer scale, leading to sensitive responsiveness to external changes. Therefore, the detection and visualization can be all in one[239–241].

Drug detection

Bioassay is a pretty important application demonstration of PC; the sensor should exhibit not only high precision but also biocompatibility and non-toxicity. The non-closed or closed-packed PC is biocompatible, and the sensitivity usually benefits from the introduction of hydrogel which makes them well-suited for implementation within the human body. In addition, trace drug tracking, organ-on-a-chip engineering and disease diagnostics are emerging in large numbers, promoting the development of bio-PC[242–245]. For example, Zhang et al. encapsulated PCs with polydopamine (PDA) to achieve multiplex miRNA detection[246]. It is accurate and has high sensitivity with a detection limit as low as 8 Fm (Fig. 9(a)). The miRNA quantification could be easily read out with distinguishing structural color. A better screening strategy was proposed by Zhao et al. with binary channel: fluorescence and structural color. The building block of

the barcode particles is SiO_2@inverse opal polyacrylamide (PAAm), and the shell was modified with TPE-$(COOH)_4$ (Fig. 9(b))[247]. The resultant core-shell structure offers two optical signals due to the volume shrink of hydrogel and the distance change between adjacent molecules. More channels and more responsive mechanisms mean an increase in accuracy. The application could be expanded in in vitro diagnosis. However, most hydrogel-based sensors are indeed disposable, and lack consistency and long-time use ability. The metasurface biomolecular detector has great potential to be used more than once without performance attenuation, and practically, it can endure long-time storage, as demonstrated by Li et al.[68]. The plasmonic metasurfaces exhibit sensitive detection of immunoglobulin G (IgG) (Fig. 9(c)). The shortcoming is obvious that the color difference among different concentrations of IgG is almost invisible. Rho et al. proposed a novel method for hyperspectral imaging using metasurface-driven plasmonic resonance energy transfer (PRET) to obtain molecular fingerprints and image electron-transfer dynamics in living cells[245]. The selective molecular fingerprint imaging can be obtained for chlorophyll *a*, chlorophyll *b*, and cytochrome *c* (Fig. 9(d)).

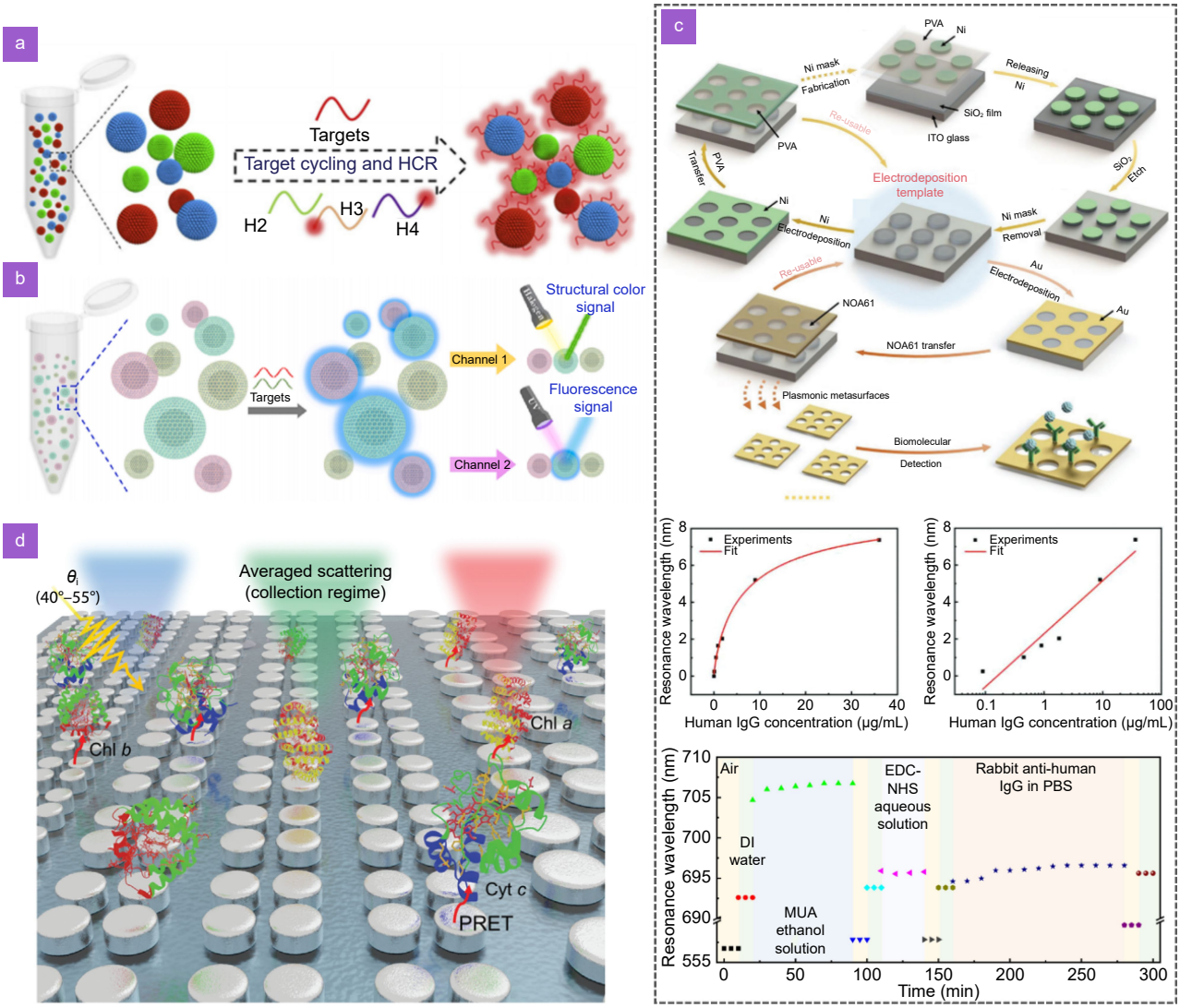

Fig. 9 | Drug detection. (**a**) Schematic diagram of the specificity of PDA-decorated PC barcodes for multiplex miRNA detection. (**b**) Schematic diagram of the AIEgens-integrated structural color barcode particles for multiplex detection with binary optical channels. (**c**) Schematic diagram of the fabrication of electrodeposition templates and plasmonic metasurfaces. (**d**) Schematic of scattering engineered metapixels in the dark-field for multiplexed nanospectroscopy based on PRET. Strong PRET occurs when the metapixels scattering peak matches the distinctive molecular absorption peaks. Figure reproduced with permission from: (a) ref.[246], Elsevier; (b) ref.[247], Elsevier; (c) ref.[68], John Wiley and Sons; (d) ref.[245], John Wiley and Sons.

Temperature indicator

Thermometers are commonly used to measure environmental temperatures, but their bulky appearance and tiny probes limit their use to specific contexts. Moreover, the most commonly used mercury thermometers are toxic. In contrast, hydrogels, in combination with colloidal crystals, have become an optimal thermal sensitive indicator (Fig. 10(a) and 10(b))[49,162,171,248,249]. First, hydrogels and colloidal crystals are both cheap and accessible. Second, the fabrication process is cost-effective and eco-friendly, with rapid and large industrial potential. Thin films can be obtained through deposition, spray coating, vertical convection self-assembly, and spin coating, etc. Third, it is flexible and can conform to a wide range of objects, thus eliminating limitations on its application scenario. Finally, the presentation of accurate temperature relies on structural color change originating from the reflection peak shift, which is vivid and easy to read out.

PNIPAM, one of the most widely used temperature-sensitive hydrogels, is usually combined with self-assembled colloidal crystals to construct temperature indicator films[250,251]. These 3D colloidal crystals possess a complete PBG, so there would be no obvious color difference with angle altering. Intriguingly, when mixed with light absorbers, these PC temperature indicators can supervise temperature change in a contactless way[252–255]. Zhao et al. mimicked the chameleon's behavior in color variation by constructing inverse opal thermosensitive carbon nanotubes and reduced graphene oxide hydrogels exhibiting not only temperature dependence but also time dependence[253]. Moreover, the PC hydrogel temperature indicator, patterned with butterfly and note designs, is both aesthetically pleasing and highly sensitive (Fig. 10(c)). Liu et al. creatively used phase transition material to develop a novel temperature indicator that can precisely indicate outer temperature[256]. Thanks to the existence of pigmentary and structural color, which come from bisphenol A and inverse opal structure, respectively. The color presentation switches from a crystalline state to a molten state above the phase transition temperature (Fig. 10(d)).

Solvent test

A fast and convenient platform for discriminating target solvent content is of great importance, especially for colorless or transparent solvents. Polar and non-polar solvents are the main inducing factors contributing to different absorption volumes for the matrix, obeying the "like dissolves like" principle (Fig. 11(a))[69,78,257,258]. In addition, the immersion of solvents can change the refractive index contrast and shift the reflectance peak, resulting in solvent-induced structural color changes due to synergy. Currently, the testing ability is relatively limited to a few target solvents, including MeOH, alcohols, IPA, BuOH, PeOH, cyclohexane, and others. However, it is still considered a highly efficient way to confirm solvent content. Wang et al. prepared PEGDA-PUA inverse opal PC films, where the swelling ratio in methanol, ethanol, *N*-propyl alcohol, and n-butyl alcohol were 21.1%, 14%, 10%, and 7.2%, respectively[259]. Particularly, the green color of the films disappeared immediately when chloroform penetrated the voids. Unlike the inverse opal hydrogels, Huang et al. prepared HEA-PEGPEA hydrogels with built-in silica particles, capable of sequentially testing at least three different solvents[260]. These

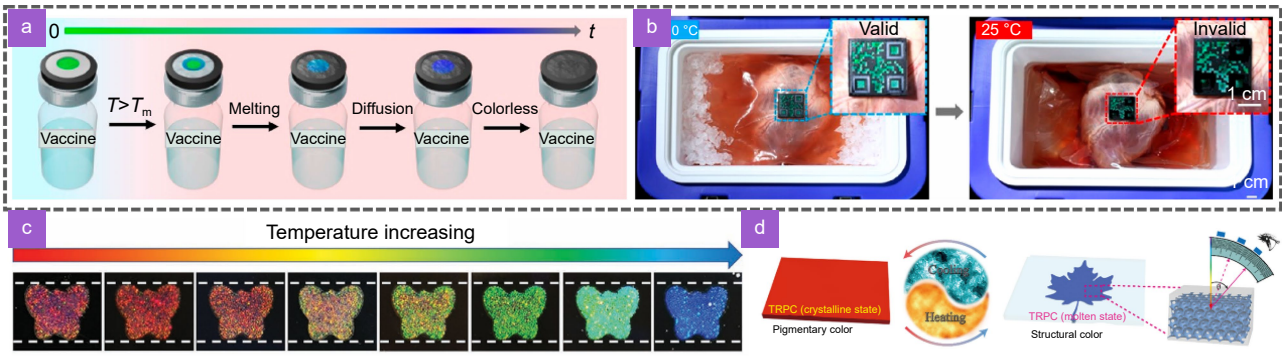

Fig. 10 | Temperature indicator. (**a**) Schematic illustration of the triggering agent melting-to-diffusing induced destruction of a P-TTI for indicating the time−temperature history of a vaccine. (**b**) Schematic diagram of the AIEgens-integrated structural color barcode particles for multiplex detection with binary optical channels. (**c**) Images of the structural color variation of the SCH with temperature increasing. (**d**) Schematic of the thermal response of the chromogenic material consists of SnO_2 inverse opal and thermochromic phase change system. Figure reproduced with permission from: (b) ref.[49], American Society of Chemistry. (c) ref.[253], John Wiley and Sons. (d) ref.[256], American Society of Chemistry.

hydrogels exhibit transparency in water, green and red in acetonitrile, orange and blue in propanol, and green plus blue in dried state (Fig. 11(b)). PC-based solvent test films are not comparable with commercial test papers in terms of sensitivity and cannot tell the exact contents within solutions. Sun et al. reported an effective way to improve sensitivity by integrating TiO_2 metasurfaces into microfluidic channels[261]. The colors change significantly and rapidly within 16.7 ms, which can be attributed to electric dipole resonance and magnetic dipole resonance collectively (Fig. 11(c)). Similarly, Zhou et al. developed a series of hydrogel micropillars, varying in diameter and height, for ethanol detection[91]. The authors verified that the micropillar diameter is a key factor, and when the diameter reached the maximum, the responsive time declined to 400 ms. The hydrogel initially exhibits a red shift when exposed to ethanol, followed by a blue shift, because the ethanol contributes to cross-linking network swelling, and then refractive change dominates over the swell effect as ethanol concentration increases (Fig. 11(d)).

Humidity measurement

Environment sensing is highly demanded in daily life to ensure a comfortable living condition[2,262–265]. Traditional hygrometers, while functional, often fall short in terms of aesthetics and technological sophistication. Nature, a reservoir of astonishing creatures and remarkable phenomena, has been an inspiration for human innovation for millennia, never ceasing to amaze and inspire us[266]. Butterflies and male beetle-*Chlorophila obscuripennis* show humidity sensitivity, as their colors switch evidently on their wings and shells. Inspired by this intriguing characteristic, 1D and 3D responsive PCs that mimic their structures are proposed (Fig. 12(a))[267]. Ma et al. realized a colorimetric sensor by spin-coating TiO_2/P(AM-MBA) stacked films and transferring them onto a PDMS substrate, followed by pressure printing to construct an angle-independent PC (Fig. 12(b))[70]. These PC films can absorb water, indicating relative humidity (RH). As RH increases from 48.1% to 89.6%, the films exhibit a color transition from blue to orange and red. Most importantly, the thin films can sustain their bright structural color even when subjected to running water or friction. Lee et al.

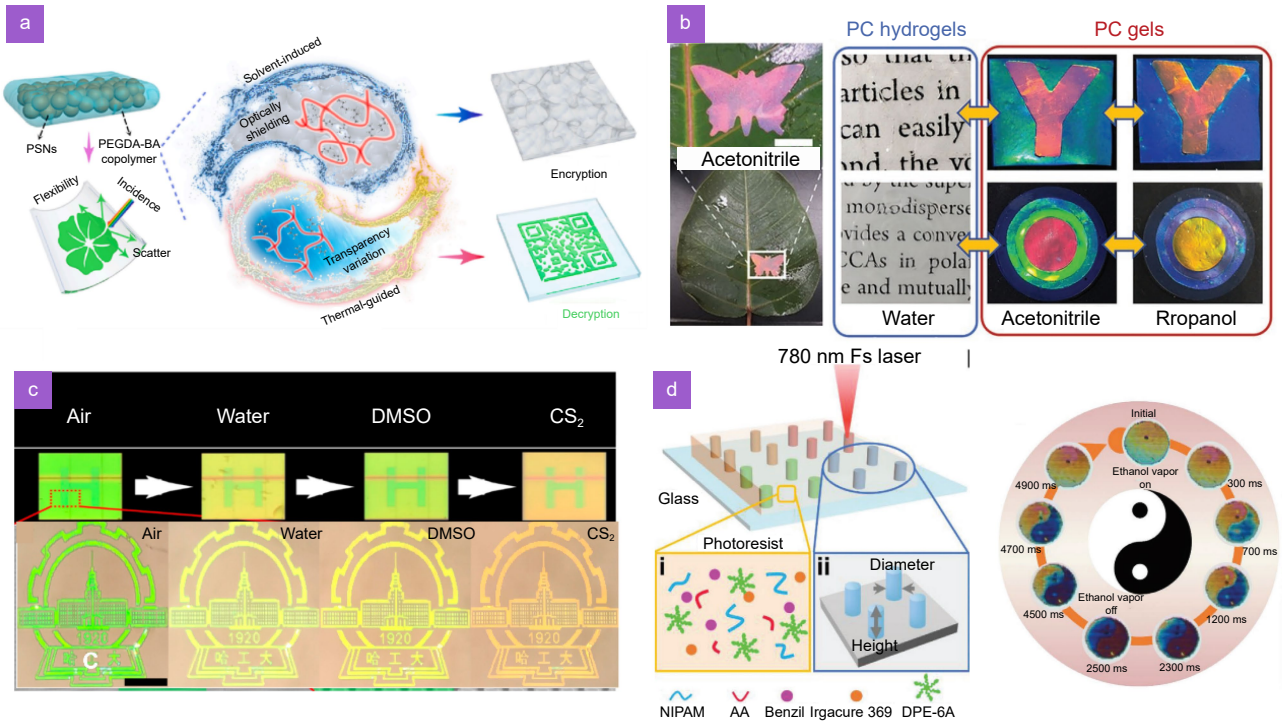

Fig. 11 | Solvent test. (**a**) Schematic illustration of the self-supporting photonic composites with stimulus-responsive capability. (**b**) Digital photos of PC patterns and corresponding PC gel patterns in water, acetonitrile, and propanol. (**c**) Bright-field photographs for the sample in different solvents and color images of the logo of our university are composed of the TiO_2 metasurface. (**d**) Schematic diagram of femtosecond laser direct writing of micropillar arrays with different structural colors and optical micrographs of the dynamic color-switching of the micropillar array exposed to ethanol vapor, showing a "Tai Chi" pattern. Figure reproduced with permission from: (a) ref.[69], Elsevier; (b) ref.[260], John Wiley and Sons; (c) ref.[261], American Society of Chemistry; (d) ref.[91], American Society of Chemistry.

adopted a similar method to construct RH sensors that offer improved sensitivity and a broader detection range, from 30% to 98% (Fig. 12(c))[268]. Significantly, the authors developed a smartphone app to enhance the convenience of using these sensors. A 1D facsimile of a creature's structure can hardly reproduce ideal outcomes, however, fully replicating its intricate structures is limited by the challenges of nanoscale fabrication. However, TPL can perfectly replicate complex structures, while it cannot use responsive material as building block since the resultant high fidelity and resolution products require highly crosslinked polymers. Delaney et al. introduced ionic liquid into cross-link networks, making them suitable for direct laser writing, which can only be applied with limited material choices (Fig. 12(d))[269]. The resulting 2.75 μm × 2.75 μm grid-like RH sensor can expand to 5% of its initial size with a significant color change.

pH gauge

The response mechanism of these sensors resembles that of solvents, which is mainly ascribed to changes in water (Fig. 13(a))[270]. However, the difference is that the former absorbs or releases water in terms of the interaction between functional groups and osmotic pressure-initiated nanoparticle size changes, while the other one occurs due to direct penetration of water or other solvents[71,81,271,272]. As Meng et al. reported, they proposed a novel synthetic method to construct inverse opal P(Cys-co-Glu) films, which show different pH responses with different ratios of Cys:Glu (Fig. 13(b))[71], and the carboxylate groups at the end of the polymer chain play an important role for that, in which deprotonation and electrostatic force converge to color change. Gu et al. designed an elastic film filled with core-shell P(MMA-BA) colloidal nanoparticles that feature well-stretchable mechanical properties and can respond to pH change from pH=5.17 to pH=14.01 (Fig. 13(c))[81]. It is noteworthy that the extra responsive hydrogels are no longer needed, simplifying the process and making it applicable for industrial scale, due to the low glass transition temperature that allows

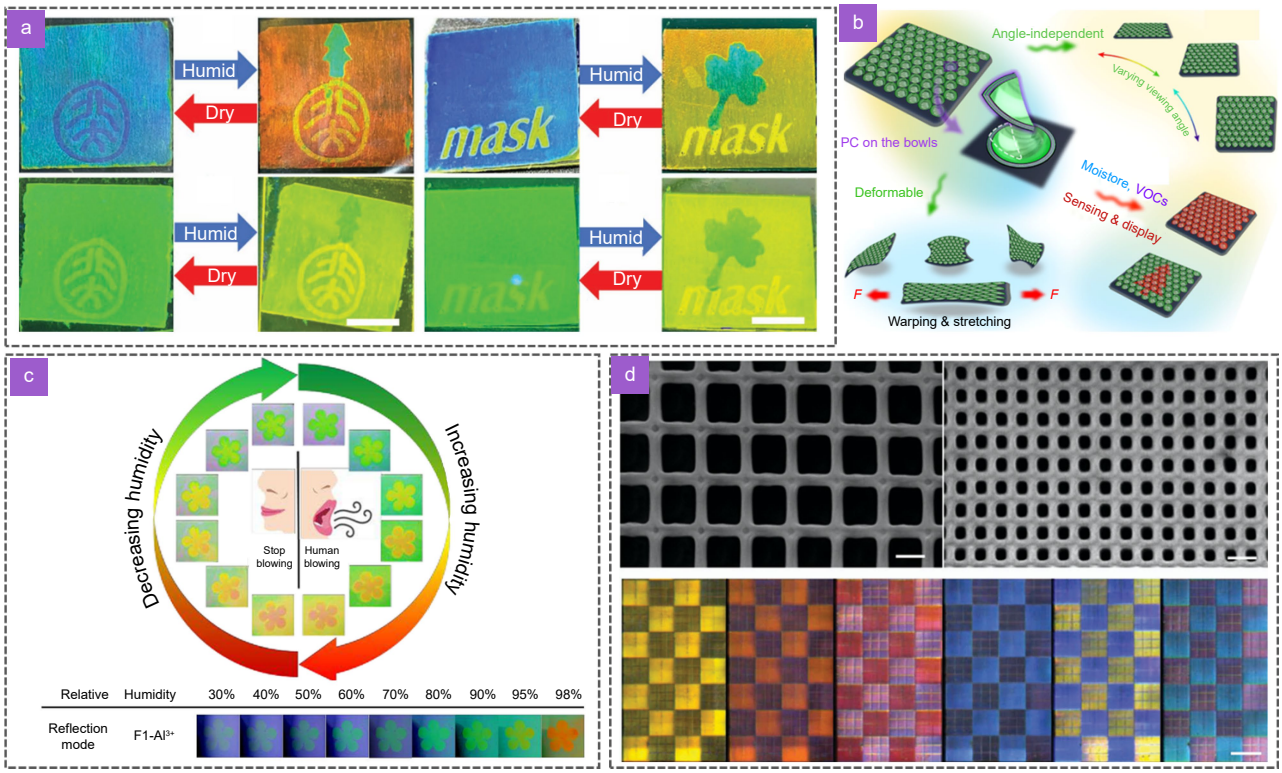

Fig. 12 | Humidity measurement. (**a**) Humidity responsiveness of the cholesteric liquid crystalline networks coating with a PKU logo as a permanent pattern and tree-like dynamic pattern. (**b**) Schematic diagram of 1D PC films built on the surface of artificial bowl array and partially enlarged details, angle-independent optical properties, flexibility and deformability, colorimetric sensing and display applications of the PC films on the bowl arrays. (**c**) Photographs of 1D PC showing the color transition during and after human blowing. (**d**) SEM images and angle-dependent optical microscopy images of periodic photonic structures were obtained through alternate fabrication of two types of square arrays, creating a checkerboard pattern. Figure reproduced with permission from: (a) ref.[267], Elsevier; (b) ref.[70], Elsevier; (c) ref.[268], Elsevier; (d) ref.[269], Royal Society of Chemistry.

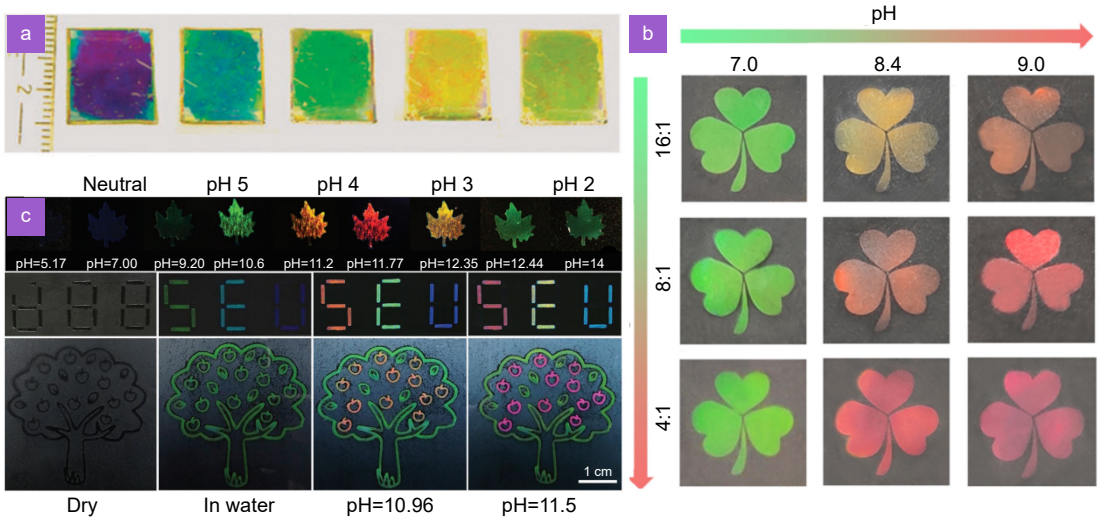

Fig. 13 | pH gauge. (**a**) Transmission dip shift of 2D PC- polyelectrolyte gels in response to different pH conditions. (**b**) Digital photos of the patterned P(Cys-co-Glu) films with different copolymerization ratios upon pH change. (**c**) Digital photographs of the leaf pattern in response to a solution with different pH values and patterned copolymer nanoparticles (up: letters; down: apple tree) reveal their encrypted color information that is controlled by the pH value of the surrounding solution. Figure reproduced with permission from: (a) ref.[270], Royal Society of Chemistry; (b) ref.[71], American Society of Chemistry; (c) ref.[81], John Wiley and Sons.

the nanoparticles to deform and fuse spontaneously at room temperature. Apart from the reflectance mode to indicate pH change, Li et al. developed a smart responsive hydrogel anchored with periodic Ag nanoparticles on the network, through the swell and shrinkage of the crosslink-network when immersed in different pH solutions the plasmonic resonance states changed accordingly leading to different transmitted color[273].

Hybrid sensing

Highly integrated sensors have the potential to replace traditional electric sensors, which usually sense only a single variation and require complicated circuits, in which lumped elements can hardly adapt to a rigid environment. Therefore, sensors that integrate multifunctional sensing and display capabilities attract great attention from researchers. Dually responsive PC sensors are the most widely studied and the common way to achieve this is through responsive hydrogels which swell or shrink to drive the structure change of nanostructures inside them[274–276]. For example, pH/thermo dual-responsive hydrogels are one of the hot topics. Wang et al. and Niu et al. both designed such hydrogel sensors without additional nanoparticles (Fig. 14(a) and 14(b))[277,278]. Interestingly, Niu and coauthors treat butterfly wings as hierarchical structure templates to build tree-like P(NIPAAM-CO-AAc) nanostructures. The pH-responsive characteristics can be explained by the protonation of —NH_2 and selectively deprotonation of —COOH in base or acid solution, while the temperature responsiveness due to the lower critical solution temperature (LCST) of the hydrogels dominates the deswelling and swelling state, resulting in blueshift and redshift respectively. Humidity/thermo sensors are often fabricated in 1D PC configuration which can directly respond to humidity and temperature change as long as there is a change in thickness[72,279]. Kashem et al. constructed alternative stacked chitosan and carboxymethyl cellulose films via the layer-by-layer method, which can alter their thickness when exposed to moisture or drying out[72]. When fixed at 40% RH, as temperature increases from 5 °C to 85 °C, the films exhibit a highly sensitive color change from pink to purple in the desorption cycle (Fig. 14(c)). Notably, at lower temperatures below 25 °C, the color can respond to even tiny changes of 0.5 °C. While the temperature is between 55 °C and 85 °C, it shows a relatively insensitive responsiveness due to being in an almost dry state. Significantly, the authors investigated the correlation between thickness, temperature, and RH using a non-linear regression model for the first time. Integrated digitated electrodes were printed onto the films to verify the application of wearable RH-temperature sensors. There are a lot of other kinds of hybrid sensors such as temperature-alcohol[280], force-temperature (Fig. 14(d))[281,282], humidity-pH (Fig. 14(e))[283], light-temperature[284], and smart motion sensors (Fig. 14(f))[285] as well as

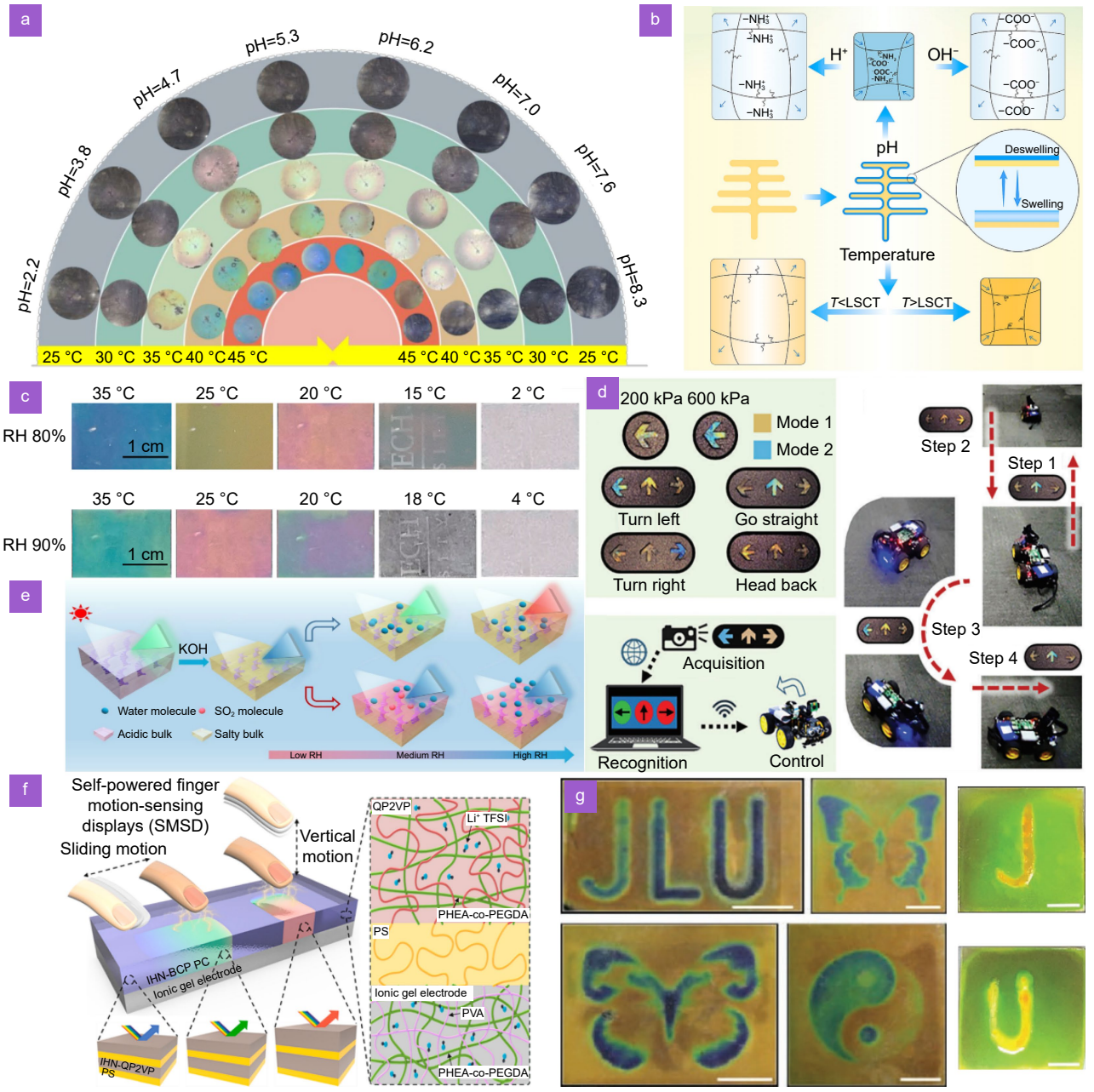

Fig. 14 | Hybrid sensing. (**a**) Representative structural colors of a dual responsive pNIPAAmStMAA hydrogel film displayed at different temperatures and pH values. (**b**) Mechanism for the dually responsive P(NIPAAM-co-AAc)-PC. (**c**) Pattern display and color changing behavior of the film in response to the temperature and RH of the surroundings. (**d**) The programmable traffic lights are controlled by pressure, the intelligent traffic signal recognition/control system and the programmed movement of the intelligent vehicle. (**e**) Mechanism of the humidity and SO_2 responsiveness of the cholesteric liquid crystalline polymer network film. (**f**) Schematic illustration of the self-powered finger motion-sensing display based on an IHN-BCP film on ionic gel electrode and motion responsive SC change in the IHN-BCP layer. Chemical structures of PS-b-QP2VP, Li^+TFSI^-, and PHEA-co-PEGDA are shown. (**g**) Schematic illustration of writing letters with distilled water on the photonic display tablets and relatively actual digital photographs and different stamp patterns on the hydrogel film and schematic illustration of the stress-induced pattern display process. Figure reproduced with permission from: (a) ref.[277], American Society of Chemistry; (b) ref.[278], Elsevier; (c) ref.[72], Elsevier; (d) ref.[281], John Wiley and Sons; (e) ref.[283], Elsevier; (f) ref.[285], Elsevier; (g) ref.[286], John Wiley and Sons.

multimodal responsiveness (Fig. 14(g))[93,286,287].

Colorimetric sensors hold great potential to be used in a wide range of fields without the need for an extra display system, power supply, complex circuits, and lengthy control codes. Additionally, most of these sensors are flexible, non-toxic, and easily accessible. Overall, sensors integrated with structural color are promising smart devices, especially in the Big Data era where

information security is highly emphasized. They do not need electric elements, which in turn eliminates interference and the possibility of invasion. However, these sensors mainly depend on changes in water content to alter their thickness or nanostructures, which has become a criticism that they cannot be used for extended periods. Cycle instability is also another problem that heavily impedes long-term use. So, for further improvement and practical application, long-term stability, high sensitivity, environment resistance, and multimodal responsiveness are urgently needed.

Printing

Printing can be traced back to 600 AD, and so far, many types of printers are widely used. We classify printing applications here based on four principles to distinguish them from anti-counterfeiting and display purposes: capable of large-scale fabrication, featuring complex and fine patterns, offering a wide color range, and providing customized colors. If the devices meet two or more of these principles and show greater promise in printing compared to others, we include them in this section. Colorful printing usually relies on independent nozzles to eject different color inks, which can be harmful to the environment and lack simplicity. Nowadays, there is an increasing demand for carbon-neutralization and green sustainability. Printers capable of producing high-fidelity, high-saturation, high-purity, and high-brightness colors, while also being eco-friendly, are considered cutting-edge in the industry[288,289]. Notably, structural color printing stands out as it can meet all these criteria with a single material, eliminating the need for traditional colorants. Full-color printing can be obtained by just adjusting geometry parameters in 1D, 2D or 3D, and the coloration mechanism varies, including metasurfaces, F-P cavities[67], PCs[126], TIR[65], plasmonic resonance[290], Mie resonance[35]. Moreover, it can overcome the challenge that 3D printing can only output single-color products through the introduction of photonic bandgap[159]. Herein, we discuss five typical types of structural color printing, focusing on resolution, color space, purity, and saturation as the main factors of concern.

Metasurface high-resolution printing

All-dielectric metasurface can confine light more efficiently than metal-based metasurface resulting from low intrinsic loss and high refractive index. Metal-based metasurfaces, on the other hand, cannot ideally reproduce bright and highly saturated full-color images. Therefore, in this discussion, we focus on all-dielectric printing, which holds more promise[291–295]. However, when combining metal coatings with dielectric building blocks, the color range and brightness can be greatly enhanced[293,296], thanks to the excitation of Mie resonance instead of plasmonic resonance.

Commonly used fabrication methods include FIB, EBL, femtosecond laser, deep-ultraviolet immersion lithography, etc[297,298]. Benefiting from the extensive fabrication options and manipulation freedoms, simulation ideas can be easily achieved. However, as lithography technology advances, the challenge is no longer limited to fabrication but also how to print ink-free images without color distortion. For instance, Sun et al. fabricated a periodic TiO_2 metasurface with a trapezoid cross-section, with such a configuration the Mie scattering was successfully merged to improve color brightness and purity in bright fields as shown in logo printing[200]. The formation of photonic bandgaps suppressed high-order resonance, thereby maintaining high saturation colors. Yang et al. use otherwise to achieve this, the high-order Mie resonance was damped by Rayleigh anomalies and the suppression of electric dipole resonance on a silicon nitride metasurface[299]. The vivid "NANO" pattern, composed of red, green, and blue primary pixels, was achieved through simple square nanostructures (Fig. 15(a)).

Expanding the color gamut is equally important, and Liu et al. successfully developed a SiO_2 nanoring that covers the 115% of the sRGB color space[73]. Nevertheless, these methods could reduce the impact of color distortion caused by high-order resonance, but the issue of lossy nature is seldom overcome. Hentschel et al. confined the electric field in air voids, which are lossy-free dielectrics[35]. The ED, MD, EQ and MQ modes are excited in Mie voids through FIB nanoholes. The authors explored the relationship between diameter, depth, and color presentation. A full-color printing of "Improvisation No. 9" was displayed as a sophisticated application. A single nanohole can produce one pixel, so the corresponding resolution can reach 36000 dpi (Fig. 15(b)).

Metasurface printing is prestigious in structural color printing for three main reasons: 1) Finer and more precise color replication from the parameter tuning in both in-plane and out-of-plane. 2) High spatial resolution with the assistance of high-end nanofabrication methods. 3) Good materials compatibility and rich structure

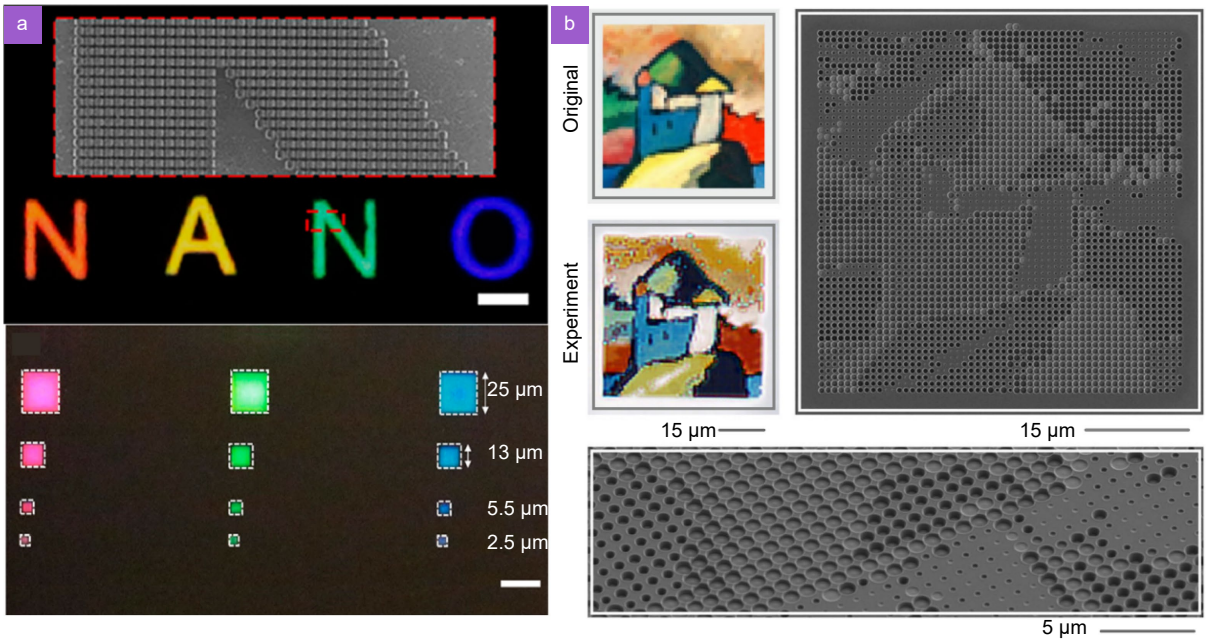

Fig. 15 | | Metasurface high-resolution printing. (**a**) Optical images of characters "NANO" created by gradually varying the size and period of Si_3N_4 color pixels and optical images of red, green, and blue Si_3N_4 metasurfaces of different areas: the lateral size changes from 25 to 2.5 μm. (**b**) Detail taken from the painting "Improvisation No. 9" by Wassily Kandinsky (Staatsgalerie Stuttgart). The top left depicts the original artwork while the lower left shows an optical microscope image of the colour-printed image. In the SEM image on the right, one can clearly identify the image as the pixel size is unchanged. In order to gain access to the full colour space, the diameter as well as the depth of the Mie voids has been varied, which is particularly well visible in the tilted SEM image. Figure reproduced with permission from: (a) ref.[299], American Society of Chemistry. (b) ref.[35], Springer Nature.

designability, enabling the coupling of different structural color mechanisms such as scattering, diffraction, resonance, and photonic band-gaps, etc. In contrast, the high-cost, time-consuming and scalability deficiency are evident disadvantages.

PC low-cost printing

1D PC typically features a multilayer construction, which is not ideal for wide-gamut color pattern printing. Consequently, colloidal crystal PCs, known for their high design flexibility, have garnered more attention. They can self-assemble to form either a hexagonal lattice or a non-close-packed suspension, both of which can be printed to produce ideal patterns and colors. However, this method is limited to low-resolution and relatively monotonous colors, requiring specific nanoparticle sizes for different colors. Despite these limitations, the method excels in large-scale printing, offering advantages such as low cost, rapid manufacturability, and environmental resistance compared to metasurfaces[300].

Screen printing, a simple and fast way to print target patterns enables its competitive status to some extents[52]. Zhou et al.[143] and Ge et al.[85] prepared non-iridescent, angle-independent and iridescent, angle-dependent PC patterns, respectively, through screen printing (Fig. 16(a)). Similarly, Zhang et al.[301] prepared Fe_3O_4@SiO_2 photonic inks consisting of PBA-HB-PEGDA using droplet microfluidics. The introduction of magnetic nanoparticles in the granular hydrogel inks enables the printed patterns have an on/off switch function that is not achievable utilizing traditional printers (Fig. 16(b)). However, the steps to obtain the final patterns are tedious, requiring either high-temperature heating or ultra violet (UV) curing. In this case, Lu et al. proposed a selectively hydrophilic as-prepared method to simplify the following steps[42]. Specifically, the substrate was treated with a fluorine-containing hydrophobic finishing agent to form a given printing hydrophilic region. After the PS-containing paste was adequately scraped, a structural color appeared in no more than 30 s, as displayed (Fig. 16(c)). Subsequently, the structural color deepened as the volatilization process finished. Interestingly, the patterns can reproduce perfect patterns without extra residual areas or cracks due to the hydrophilic-hydrophobic difference areas. Moreover, the direct writing method is an alternative way to construct customized

units, which makes it easier to print multicolor images. Shanker et al. inkjet printed colloidal nanocrystals microdomes to minimize angle-dependence through the careful control of Ohnesorge number at 3, the defect-free, uniform, and well-packed microdome units can be continuously printed (Fig. 16(d))[214]. Pyo et al. used a femtoliter meniscus to construct periodic gratings, thereby endowing two dimensions to control structural color presentation, such as the particle size of PS and the grating pitch[43]. The angle-dependent iridescent structural color can cover almost the full-color range, from blue to red, as the incident angle of light increases from 13.5° to 23° (Fig. 16(e)). Furthermore, three primary colors can be obtained by setting the grating pitch at 1900, 1400, and 1000 nm.

However, colloidal crystal-based printing suffers from low resolution because each single pixel must contain enough nanoparticles to ensure the interaction of light. Chen et al. developed a shape memory PC paper that can not only achieve a higher resolution than 100 μm but also has rewritable ability[302]. The authors demonstrated two ways to print target patterns, namely, pressure-induced printing and pin-printing, which achieved higher resolution with versatile and colorful images (Fig. 16(f)). The shape memory paper can be colorless in its deformed state and recover to its primary image presentation

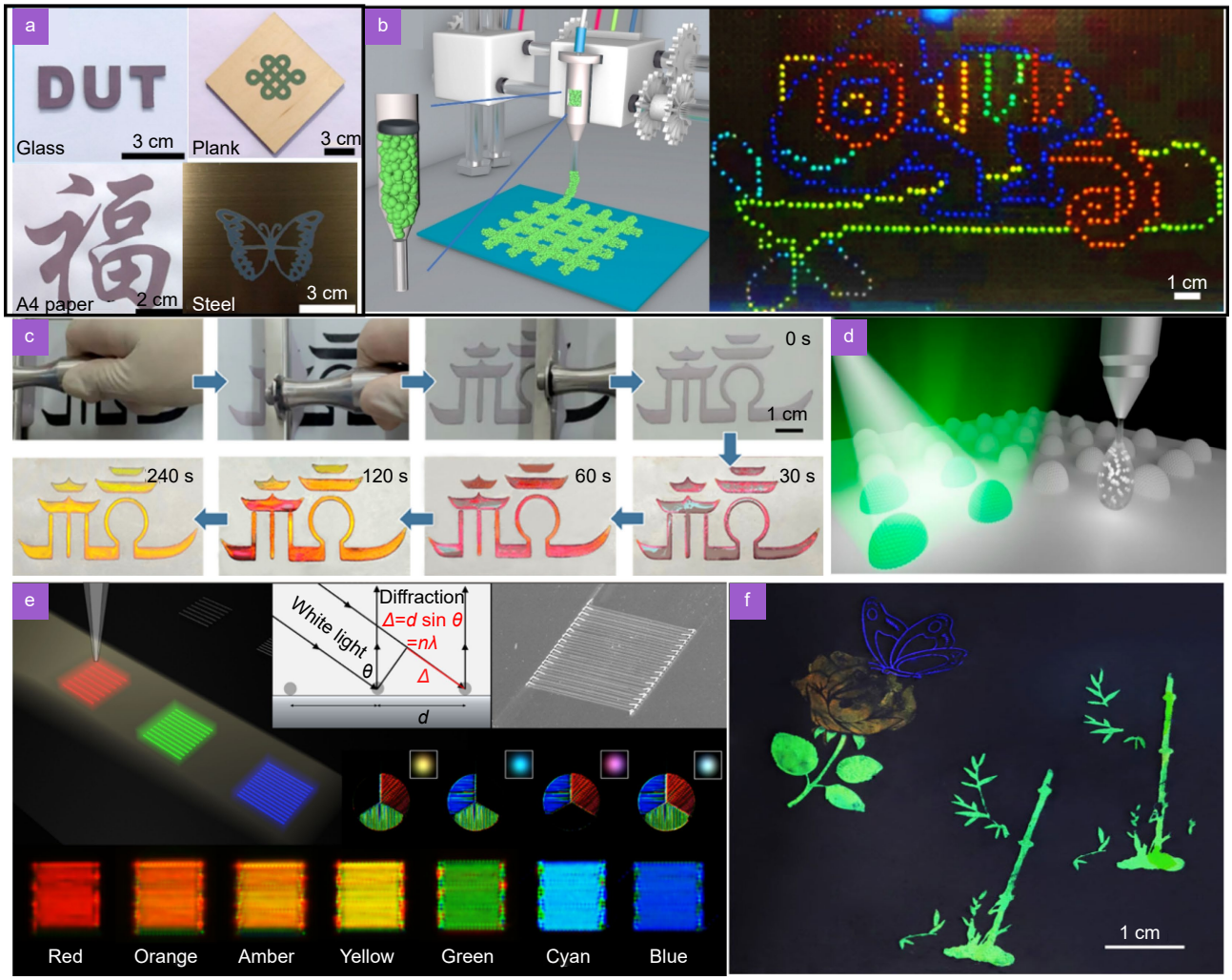

Fig. 16 | PC low-cost printing. (**a**) Photographs of the brilliant noniridescent structural colors fabricated by screen printing on various substrates. (**b**) Schematic for 3D printing of the photonic granular hydrogel ink. (**c**) Digital photo of spreading and assembling of the color paste on the pattern layer under an external shear-induced force. (**d**) Schematic illustration of inkjet-printed melanin NP photonic microdomes. (**e**) Diffraction images obtained from a grating of pitch 1900 nm by white incident light of the given orientation. (**f**) The combination pattern obtained by overlapping three films templated from silica microspheres with three sizes. Figure reproduced with permission from: (a) ref.[143], Elsevier; (b) ref.[301], John Wiley and Sons; (c) ref.[42], American Society of Chemistry; (d) ref.[214], American Society of Chemistry; (e) ref.[43], American Society of Chemistry; (f) ref.[302], John Wiley and Sons.

state under stress or ethanol drying.

F-P high-brightness printing

While metal metasurface may not present ideal saturated high-brightness colors due to the intrinsic loss of metal, the double metal layers that compose the F-P cavity can achieve slightly enhanced coloration performance[41,303]. This improvement can be explained by the constructive and destructive effects on the top metal layer and the middle dielectric layer, which can effectively absorb specific wavelengths of light. Most importantly, it can simplify the fabrication process, requiring only electron beam evaporation or a magnetron sputtering system[53]. As Seo et al. developed, the authors fabricated different patterns on stainless steel (STS) and aluminium substrates. By changing the thickness of the Au layer in Au/Si_3N_4/STS films, they were able to produce a range of colors. Colorful patterns, as shown in Fig. 17(a), could be printed with the assistance of a mask[18]. To achieve high resolution, the thinner the total thickness, the better the resolution can be obtained[304]. The key to optimizing color presentation performance is the reasonable design of the topmost metal layer. Yang et al. deposited an asymmetric F-P cavity on periodic nanopillars, and the Al/hydrogen silsesquioxane/Ni sandwich-like structure can generate more vivid color than pure periodic nanostructures[74]. It is noteworthy that the thin Ni film exerts a great effort to improve the vividness of color, while its absence results in a pale and less striking image (Fig. 17(b)). The F-P resonant cavity provides a suitable platform for printing patterns and images with perfect color performance, high brightness, and saturation, without the need for complex post-processing. In the pretreatment process, vacuum deposition is necessary and can significantly decrease costs compared to FIB, EBL, and reactive ion etching.

A more economical method was proposed by Choi and coauthors[305]. They first developed a polymer-assisted photochemical deposition system; this system can deposit a few kinds of metals at room temperature with good continuity. The metal ions are encapsulated in a composite solution and reduced to nanoparticles with the assistance of pAAm. In their experiments, different thicknesses of Ag films were deposited on a SiO_2/PVD Ag substrate to form an asymmetric F-P cavity. Based on this, "ASU" and "Stich" were printed to verify colorful print presentation, yet some defects and sacrifice of brightness can be seen (Fig. 17(c)). This new cost-effective manufacturing strategy is expected to attract significant attention. However, if we can print images or other information like laser printer, the printed information will have a higher resolution and is easy to control. Zhu et al. put forward a new concept called "resonant laser printing (RLP)", they combined laser printing with the F-P cavity and meticulously set the TiO_2 thickness at 51 nm, which is the exact condition to excite perfect absorption of 532 nm laser (Fig. 17(d))[19]. By adjusting the power of the laser from 0 to 1.9 nJ, atop Au film morphology exhibits apparent change leading to an appearance color transition from pink to cyan.

Plasmonic wide-gamut printing

Metals have peculiar properties that dielectric materials cannot match, such as the well-known plasmonic resonance, which is the collective oscillation of electrons. Once the wavelength of light is located near the resonance wavelength, the electric field can be well confined and enhanced.

Plasmonic resonance systems typically consist of a disordered system with randomly distributed nanoparticles, nanorods, nanodisks, nanoislands or nanoclusters, and thus, the chaotic nature of the system is the primary source of its robustness against perturbations[306]. By delicately controlling the resonance wavelength, specific single-band or wide-wavelength light can be absorbed, enabling the presentation of not only common colorful patterns but also bright white and deep black colors. There are two mainstream paths to gaining plasmonic systems, the solution reduction method and solid nanofabrication. For solution-based plasmonic printing, Zhang et al. demonstrated a simple way using electron transportation from TiO_2 to Ag^+, which was excited by a UV lithography system. Ag^+ as an electron receiver can be reduced to Ag, and then show different morphology with different exposure doses, and the TiO_2 substrate acts like a middle bridge to support Fano resonance (Fig. 18(a))[290]. Structural color can be easily controlled by tuning thickness of TiO_2 and exposure dose. Cui et al. developed a pure solution system to support resonance mode, Au nanodisks were dispersed in a solution and then embedded in a PDMS matrix for laser printing[95]. Full CMY color printing can be obtained since Au nanodisks absorb laser pulse energy due to localized surface plasmon resonances induced shape change, with increasing applied pulse energy from 2.5 nJ to 3 μJ, colors from magenta to yellow can be shown (Fig. 18(b)).

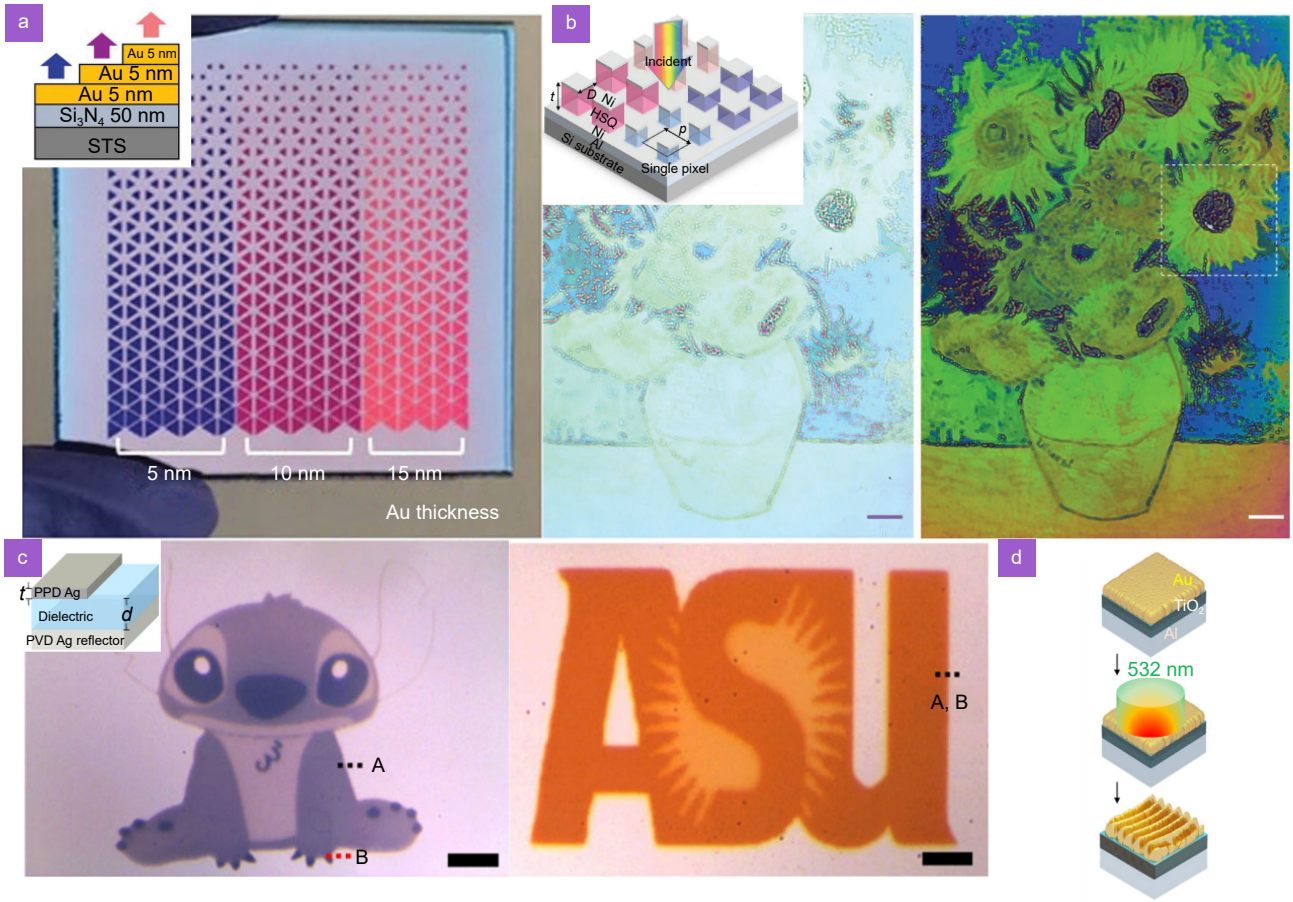

Fig. 17 | F-P high-brightness printing. (**a**) Color images printed on stainless steel substrates (3 × 3 cm² in size) along with a structure schematic. An Au layer was selectively deposited using a shadow mask to different thicknesses onto a 50 nm thick Si_3N_4 film. (**b**) Full-color reproduction of van Gogh's "Still Life: Vase with Twelve Sunflowers" using the obtained palette and the comparison before and after Ni deposition. (**c**) A cartoon character "Stitch" (d = 75 nm) and a symbol of Arizona "Cactus" (d = 150 nm) with various colors. (**d**) Schematics of the FP-type hybrid metasurface with Au-TiO_2-Al coatings. The polarized in-resonance laser pulses interact strongly with the optical cavity, making the metasurface extremely absorbing across the illuminated area, which creates ripples and modifies the optical cavity to an off-resonance state. Figure reproduced with permission from: (a) ref.[18], John Wiley and Sons; (b) ref.[74], John Wiley and Sons; (c) ref.[305], Springer Nature; (d) ref.[19], American Society of Chemistry.

Solution-based plasmonic structural color exhibits weak saturation and non-iridescence, which may be attributed to the existence of residual impurities. Despite this, compared to all-solid plasmonic resonance color, solution-based approaches offer the advantages of low cost and fast manufacturability. All-solid plasmonic systems are often fabricated using magnetron sputtering, e-beam evaporation, or EBL.

Aluminium and silver nanoislands have been successfully demonstrated to generate perfect plasmonic color and enable large-scale fabrication[75,307]. Hail et al. mixed Ag nanorods to achieve continuous primary colors within a single pixel, greatly expanding the color gamut (Fig. 18(c))[308]. However, achieving a black color with structural colors is challenging due to the absence of broadband absorption characteristics. Mao et al. developed a novel approach that combines modifications in cavity space and disorder of plasmonic nanoparticles simultaneously[75]. When the decay rates and coupling rates are well-matched, broadband absorption occurs. Thus, the authors printed a full-color painting of "Peony Flower" that includes black elements (Fig. 18(d)).

Overall, the all-solid plasmonic platform offers superior color performance with high saturation, brightness, and stability, while the stand-alone and transferrable ability of the platforms remains a pending problem. Although a feasible way can solve this by the introduction of a sacrificial layer and in flake format as structural color paint, the color shade and hue will be affected[307].

Other full-color printing

Nanoprinting of structural colors can be categorized

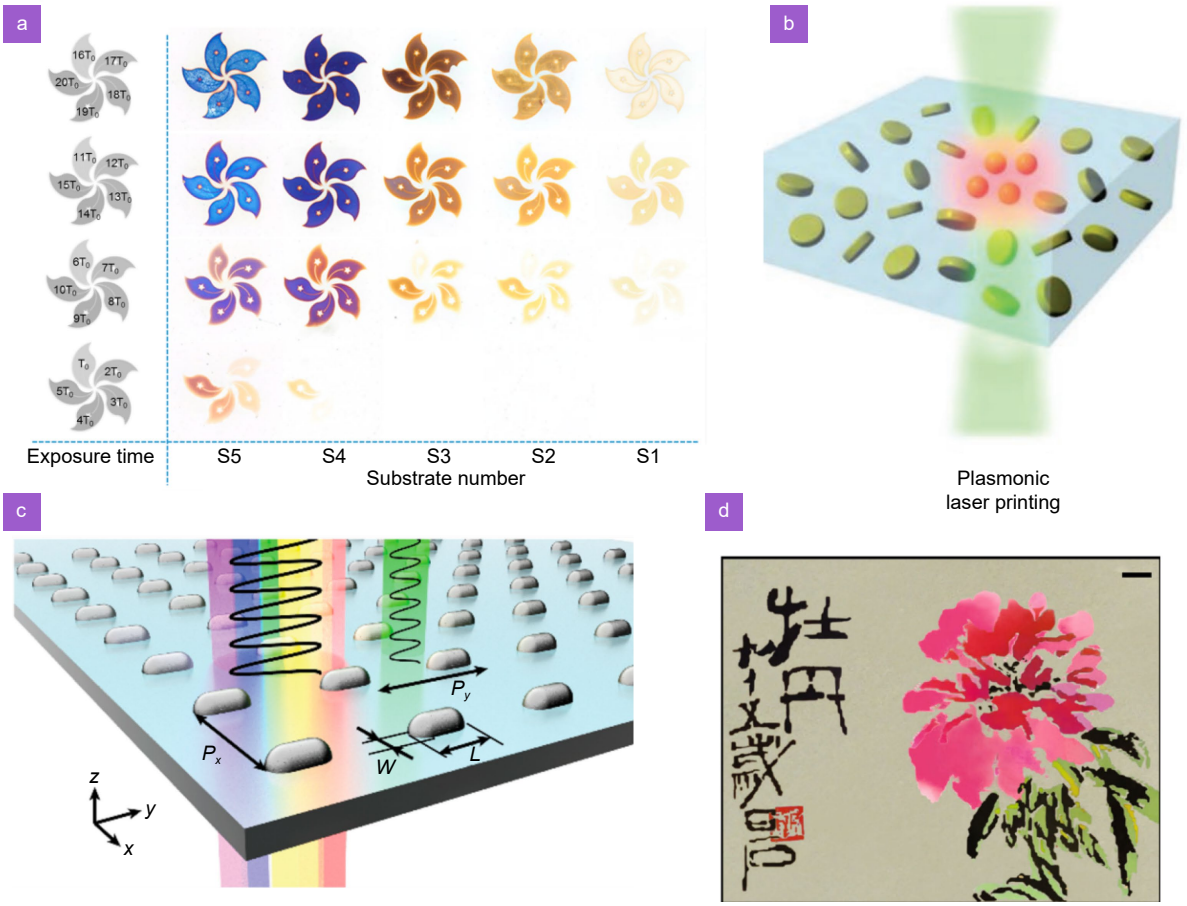

Fig. 18 | Plasmonic wide-gamut printing. (**a**) Color images of Hong Kong bauhinia flowers printed on various substrates. (**b**) The Au NDs can be thermally reshaped into nanospheres under single-pulse laser exposure with sufficient pulse energy. (**c**) Schematic of the single color plasmonic pixel consisting of a lattice of silver nanorods on a glass substrate. White light illumination polarized along the long axis of the nanorods results in distinct colors observed in reflection. The length *L* and width *W* of the nanorods set the local surface plasmon resonance; the periodicity along the *x* direction, P_x, sets the lattice coupling, and the periodicity along the *y* direction, P_y, sets the color luminance. (**d**) The fabricated hybrid structure of "Peony Flower" based on plasmonic systems. Figure reproduced with permission from: (a) ref.[290], American Society of Chemistry; (b) ref.[95], John Wiley and Sons; (c) ref.[308], American Society of Chemistry; (d) ref.[75], American Society of Chemistry.

according to fabrication methods, i.e., top-down and bottom-up methods. The integration of bottom-up with top-down methods facilitates the creation of 3D volumetric structures with uniform structural color in every direction. Most importantly, this approach enables the production of flexible, adaptable, and even responsive 3D structures. The incorporation of thermosensitive and photosensitive hydrogels introduces significant potential for advancing 4D structural color printing (Fig. 19(a) and 19(b))[309–311]. Moreover, TPL 3D printing is an alternative way to achieve complete PBG with woodpile building blocks, providing slow light modes and stopbands for coloration, particularly, extremely fine and complex 3D structures can be printed (Fig. 19(c))[44,45]. Those emerging methods are promising for the printing revolution, but their application scenarios are limited.

In the realm of planar printing, which is most frequently used in daily life and industry, high-temperature and wear-resistance materials are not concerned first for economical principle and manufacturability feasibility. Therefore, a viable method to maintain perfect endurance without color performance sacrifice as well as to support resonance mode is demanded. The introduction of ceramics to construct resonance cavity and oxidation layer as coatings for laser printing can flawlessly meet such purpose (Fig. 19(d))[38].

Additionally, Standing-wave optics can also be applied to lithography images in polymer films, this photosensitive polymer undergoes crosslinking under ultraviolet light, resulting in residual stress and the formation of

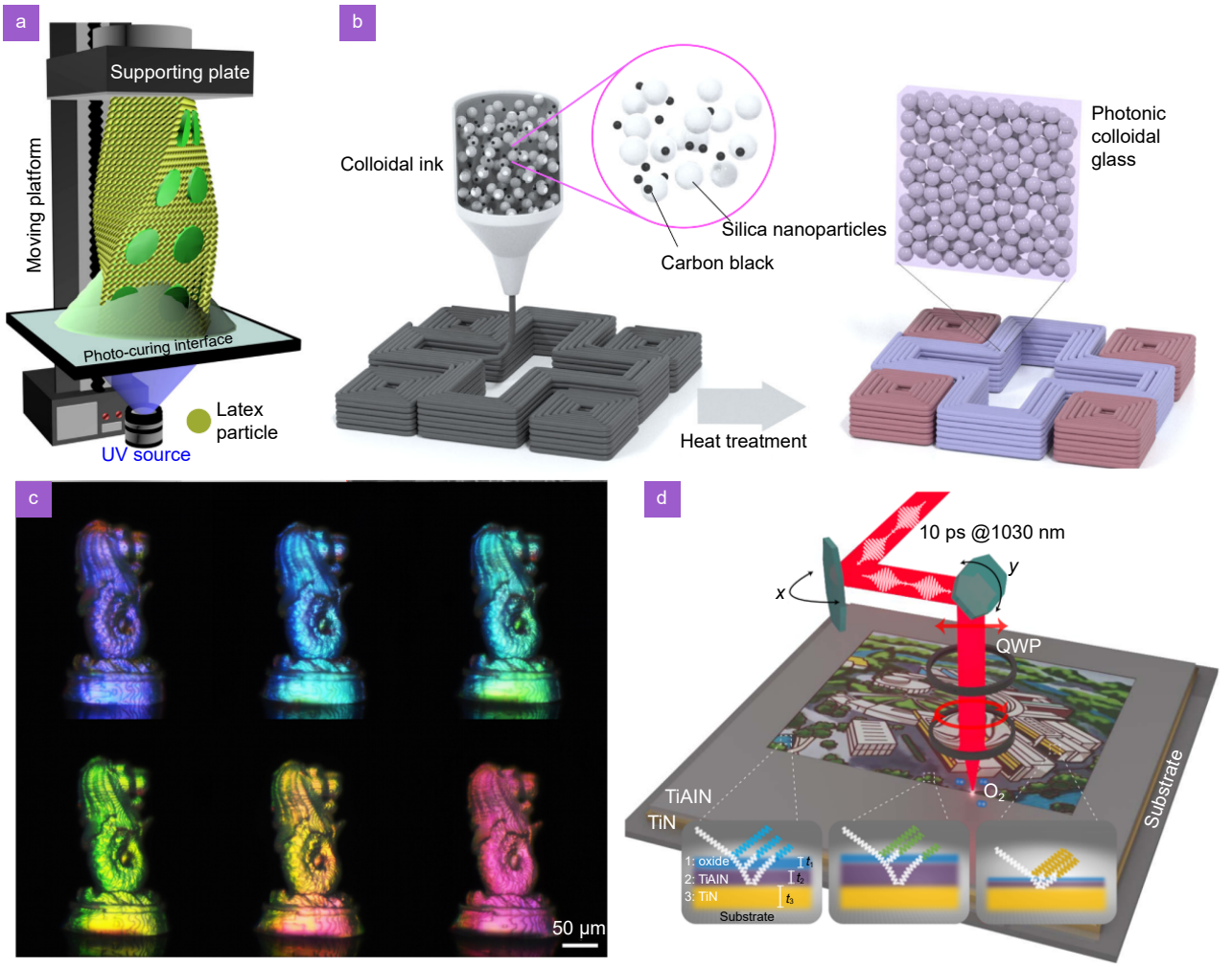

Fig. 19 | Other typical full-color printings. (**a**) Schematic of the continuous DLP 3D printing apparatus for fabricating 3D Lego brick structure with volumetric color property. (**b**) Schematics illustrating the 3D printing of colloidal inks into objects with isotropic structural color. Coloration is generated by photonic colloidal glasses obtained upon complete drying of the as-printed objects. (**c**) Miniaturized 3D Merlions with monochromatic structural colors printed by TPL. (**d**) Scheme of surface coloring by ultrafast laser. Figure reproduced with permission from: (a) ref.[309], Springer Nature; (b) ref.[43], Springer Nature; (c) ref.[44], American Society of Chemistry; (d) ref.[38], Springer Nature.

craze-like microfibrils upon weak solvent infiltration. The presence of multilayered Bragg interferometers is the main reason for the presentation of structural color[37].

Overall, structural color printing provides a feasible and environment-friendly avenue to present information and images. There are various methods for structural color printing, and each of them has outstanding advantages but also shortcomings: Metasurface can offer ultrahigh-resolution printing, allowing for the display of more details and precise color replication. This is achieved by assigning more than one unit to a single pixel and providing greater freedom to control the unit's parameters. However, other methods are more cost-effective, while PC printing may not perfectly achieve complex information or images, F-P printing may not create flexible or soft patterns, and plasmonic printing requires skilful operators to control the formation of a disordered system.

Conclusion and perspective

Structural color is initially inspired by nature and has been successfully applied in many fields through elaborate design and optimization. In this review, we summarized recent research progress and applications of structural color, including anti-counterfeiting, display technology, display-indicator integrated sensors, and printing. According to the mechanisms, structural color devices can be divided into metasurfaces, PCs, resonant cavities, plasmonic resonant systems, and colloidal crystal nanoparticles. Various applications based on these

mechanisms have shown significant advancements and promising potential to replace traditional strategies. Importantly, structural color devices have already been used in almost all aspects of life, military, and medicine and are going to revolutionize everything we do.

Additionally, considering the developmental history, the application of structural color has gradually evolved from aesthetic richness in color to a direction of multifunctionality and systematization. The fabrication methods for devices based on structural color have been progressively refined, transitioning from bottom-up approaches reliant on chemistry to top-down methods involving the construction of artificial structures, with increasing precision, color gamut, and color controllability. Currently, structural color has transcended single-plane structures, and is gradually advancing towards multidimensionality and multiscaling. However, there remain some challenges and room for improvement, which can boost the structural color application more advanced and desirable.

First, developing intelligent structural color devices. Although the advantages of dynamic adjustability have already broken through the inherent barriers of traditional devices in many fields, the rise of artificial intelligence has also posed new requirements for structural color application. In the future, it can be fused with intelligent devices, including chip implantation, integration into the IOT, and dynamic coding devices, to achieve a feedback loop of self-perception and autonomous adjustment of functions.

Second, establishing a nanostructure database system. Using structural design principles as a guide and improving the completeness of the database as the focus, on one hand, a model combining numerical algorithms and geometric structure designs should be established to explore the optimal three-dimensional structure through big data and artificial intelligence. On the other hand, a database of performance parameters for structural color devices under different material systems should be constructed, enhancing autonomous selection, and assisting future researchers in developing more advanced functional devices.

Third, enhancing the closed-loop link between simulation design and physical manufacturing. Although 4D printing, biomimetic metamaterials, and lithography technologies have provided methods to solve the current challenges of complex structure and high precision requirements of structural color devices, there are still limitations in device integration, miniaturization, and material options. As a result, many simulation models with excellent performance are difficult to translate into physical prototypes. Therefore, future efforts should focus on expanding the printable material system and improving micro-nano fabrication processes, fully leveraging the important role of simulation design in guiding physical manufacturing and vice versa.

Finally, exploring applications of structural color in other fields. To broaden the application of structural color in various fields, the primary challenge that must be addressed is the achievement of large-scale fabrication. Both bottom-up and top-down approaches should concentrate on reducing costs and improving efficiency, with the development of assembly line production techniques. Following this, the exploration of applications for structural color devices in the realms of energy[312], communication[313], and information technology should be pursued[314].

References

1. Teyssier J, Saenko SV, van der Marel D et al. Photonic crystals cause active colour change in chameleons. *Nat Commun* **6**, 6368 (2015).
2. Kim JM, Bak JM, Lim B et al. Background color dependent photonic multilayer films for anti-counterfeiting labeling. *Nanoscale* **14**, 5377–5383 (2022).
3. Liu CY, Long Y, Yang BQ et al. Facile fabrication of microgrooves based photonic crystals towards anisotropic angle-independent structural colors and polarized multiple reflections. *Sci Bull* **62**, 938–942 (2017).
4. Wang L, Ma LJ, Zhao QL et al. Internal nanocavity based high-resolution and stable structural colours fabricated by laser printing. *Opt Express* **29**, 7428–7434 (2021).
5. Raza S, Lavieja C, Zhu XL et al. Resonant laser printing of bimaterial metasurfaces: from plasmonic to photonic optical response. *Opt Express* **26**, 20203–20210 (2018).
6. Isapour G, Lattuada M. Bioinspired stimuli-responsive color-changing systems. *Adv Mater* **30**, 1707069 (2018).
7. Shin J, Jo W, Hwang JH et al. Regional control of multistimuli-responsive structural color-switching surfaces by a micropatterned DNA-hydrogel assembly. *Nano Lett* **22**, 5069–5076 (2022).
8. Qi Y, Zhang SF, Lu AH. Responsive structural colors derived from geometrical deformation of synthetic nanomaterials. *Small Struct* **3**, 2200101 (2022).
9. Vashistha V, Vaidya G, Hegde RS et al. All-dielectric metasurfaces based on cross-shaped resonators for color pixels with extended gamut. *ACS Photonics* **4**, 1076–1082 (2017).
10. Yang Y, Seong J, Choi M et al. Integrated metasurfaces for re-envisioning a near-future disruptive optical platform. *Light Sci Appl* **12**, 152 (2023).
11. Yun JG, Sung J, Kim SJ et al. Ultracompact meta-pixels for high colour depth generation using a bi-layered hybrid meta-

surface. *Sci Rep* **9**, 15381 (2019).
12. Jung C, Kim G, Jeong M et al. Metasurface-driven optically variable devices. *Chem Rev* **121**, 13013–13050 (2021).
13. Li YJ, Hu JT, Zeng YX et al. Recent progress on structural coloration. *Photonics Insights* **3**, R03 (2024).
14. Yang DP, Ouyang C, Zhang YQ et al. Rapid fabrication of alcohol responsive photonic prints with changeable color contrasts for anti-counterfeiting application. *Adv Mater Interfaces* **8**, 2001905 (2021).
15. Jo S, Woo JY, Oh JH et al. Angle-insensitive transmission and reflection of nanopatterned dielectric multilayer films for colorful solar cells. *ACS Appl Mater Interfaces* **12**, 29979–29985 (2020).
16. Song HS, Lee GJ, Yoo DE et al. Reflective color filter with precise control of the color coordinate achieved by stacking silicon nanowire arrays onto ultrathin optical coatings. *Sci Rep* **9**, 3350 (2019).
17. Zhao YH, Yang YH, Ji CY et al. Thermosensitive plasmonic color enabled by sodium metasurface. *Adv Funct Mater* **33**, 2214492 (2023).
18. Seo M, Kim J, Oh H et al. Printing of highly vivid structural colors on metal substrates with a metal-dielectric double layer. *Adv Opt Mater* **7**, 1900196 (2019).
19. Zhu XL, Engelberg J, Remennik S et al. Resonant laser printing of optical metasurfaces. *Nano Lett* **22**, 2786–2792 (2022).
20. Bao GY, Yu WY, Fu QQ et al. Low-voltage electrically responsive photonic crystal based on weak-polar colloidal system. *Adv Opt Mater* **10**, 2201188 (2022).
21. Fu QQ, Yu WY, Bao GY et al. Electrically responsive photonic crystals with bistable states for low-power electrophoretic color displays. *Nat Commun* **13**, 7007 (2022).
22. Wen XX, Lu XG, Wei CP et al. Bright, angle-independent, solvent-responsive, and structurally colored coatings and rewritable photonic paper based on high-refractive-index colloidal quasi-amorphous arrays. *ACS Appl Nano Mater* **4**, 9855–9865 (2021).
23. Wang F, Zhang X, Lin Y et al. Structural coloration pigments based on carbon modified ZnS@SiO_2 nanospheres with low-angle dependence, high color saturation, and enhanced stability. *ACS Appl Mater Interfaces* **8**, 5009–5016 (2016).
24. Chan JYE, Ruan QF, Ng RJH et al. Rotation-selective moiré magnification of structural color pattern arrays. *ACS Nano* **13**, 14138–14144 (2019).
25. Wang HT, Wang H, Ruan QF et al. Optical fireworks based on multifocal three-dimensional color prints. *ACS Nano* **15**, 10185–10193 (2021).
26. Wang JT, Tonkaev P, Koshelev K et al. Resonantly enhanced second- and third-harmonic generation in dielectric nonlinear metasurfaces. *Opto-Electron Adv* **7**, 230186 (2024).
27. Tang YT, Intaravanne Y, Deng JH et al. Nonlinear vectorial metasurface for optical encryption. *Phys Rev Appl* **12**, 024028 (2019).
28. Dai Q, Guan ZQ, Chang S et al. A single-celled Tri-functional metasurface enabled with triple manipulations of light. *Adv Funct Mater* **30**, 2003990 (2020).
29. Liu XY, Zhang JC, Leng BR et al. Edge enhanced depth perception with binocular meta-lens. *Opto-Electron Sci* **3**, 230033 (2024).
30. Lai XT, Ren Q, Vogelbacher F et al. Bioinspired quasi-3D multiplexed anti-counterfeit imaging via self-assembled and nanoimprinted photonic architectures. *Adv Mater* **34**, 2107243 (2022).
31. Li ZB, Clark AW, Cooper JM. Dual color plasmonic pixels create a polarization controlled Nano color palette. *ACS Nano* **10**, 492–498 (2016).
32. Gao H, Fan XH, Wang YX et al. Multi-foci metalens for spectra and polarization ellipticity recognition and reconstruction. *Opto-Electron Sci* **2**, 220026 (2023).
33. Zhou YJ, Liu T, Dai CH et al. Functionality multiplexing in high-efficiency metasurfaces based on coherent wave interferences. *Opto-Electron Adv* **7**, 240086 (2024).
34. Lu L, Dong ZG, Tijiptoharsono F et al. Reversible tuning of Mie resonances in the visible spectrum. *ACS Nano* **15**, 19722–19732 (2021).
35. Hentschel M, Koshelev K, Sterl F et al. Dielectric Mie voids: confining light in air. *Light Sci Appl* **12**, 3 (2023).
36. Yang WH, Xiao SM, Song QH et al. All-dielectric metasurface for high-performance structural color. *Nat Commun* **11**, 1864 (2020).
37. Ito MM, Gibbons AH, Qin DT et al. Structural colour using organized microfibrillation in glassy polymer films. *Nature* **570**, 363–367 (2019).
38. Geng J, Xu LY, Yan W et al. High-speed laser writing of structural colors for full-color inkless printing. *Nat Commun* **14**, 565 (2023).
39. Han RZ, Zhang YC, Jiang QL et al. Ultrafast dynamics of femtosecond laser-induced high spatial frequency periodic structures on silicon surfaces. *Opto-Electron Sci* **3**, 230013 (2024).
40. Li SJ, Kou DH, Zhang SF et al. Large-area fabrication of structurally colored and humidity sensitive composite nanofilm via ultrasonic spray-coating. *Polymers* **13**, 3768 (2021).
41. Su YF, Tang XY, Huang GH et al. Large-area, flexible, full-color printings based on asymmetry Fabry–Perot cavity resonances. *Opt Commun* **464**, 125483 (2020).
42. Lu XD, Wang XH, Li XY et al. Preparation of patterned photonic crystals with high fastness and iridescence effect via resist-screen printing. *ACS Appl Mater Interfaces* **15**, 31935–31942 (2023).
43. Bae J, Yoo C, Kim S et al. Three-dimensional printing of structural color using a femtoliter meniscus. *ACS Nano* **17**, 13584–13593 (2023).
44. Liu HL, Wang HT, Wang H et al. High-order photonic cavity modes enabled 3D structural colors. *ACS Nano* **16**, 8244–8252 (2022).
45. Liu YJ, Wang H, Ho J et al. Structural color three-dimensional printing by shrinking photonic crystals. *Nat Commun* **10**, 4340 (2019).
46. Fu QQ, Zhu HM, Ge JP. Electrically tunable liquid photonic crystals with large dielectric contrast and highly saturated structural colors. *Adv Funct Mater* **28**, 1804628 (2018).
47. Bao GY, Yu WY, Fu QQ et al. Low-voltage and wide-tuning-range SiO_2/aniline electrically responsive photonic crystal fabricated by solvent assisted charge separation. *J Mater Chem C* **11**, 3513–3520 (2023).
48. Yu WY, Zhao YX, Sheng WT et al. Creation of nanotips on ITO electrode by nanoparticle deposition: an easy way to enhance the performance of electrically responsive photonic crystal and fabricate electrically triggered anticounterfeiting tags. *Adv Funct Mater* **33**, 2304474 (2023).
49. Huang C, Shang YY, Hua JC et al. Self-destructive structural

color liquids for time-temperature indicating. *ACS Nano* **17**, 10269–10279 (2023).
50. Fang Y, Ni YL, Leo SY et al. Reconfigurable photonic crystals enabled by pressure-responsive shape-memory polymers. *Nat Commun* **6**, 7416 (2015).
51. Liu Y, Luo W, Fan QS et al. Polyphenol-mediated synthesis of superparamagnetic magnetite nanoclusters for highly stable magnetically responsive photonic crystals. *Adv Funct Mater* **33**, 2303470 (2023).
52. Li G, Luo W, Che ZY et al. Lipophilic magnetic photonic nanochains for practical anticounterfeiting. *Small* **18**, 2200662 (2022).
53. Yang ZM, Zhou YM, Chen YQ et al. Reflective color filters and monolithic color printing based on asymmetric Fabry-Perot cavities using nickel as a broadband absorber. *Adv Opt Mater* **4**, 1196–1202 (2016).
54. Liu C, Wang GR, Zhang LY et al. Dynamic color display with viewing-angle tolerance based on the responsive asymmetric Fabry-Perot cavity. *ACS Appl Mater Interfaces* **14**, 7200–7207 (2022).
55. Jeong HD, Lee J, Yu ES et al. Physicochemical modulation of nanometer-thick etalon films for liquid-sensitive color display with full-color spectrum generation. *ACS Appl Nano Mater* **4**, 389–395 (2021).
56. Ghobadi A, Hajian H, Soydan MC et al. Lithography-free planar band-pass reflective color filter using a series connection of cavities. *Sci Rep* **9**, 290 (2019).
57. Li ZY, Butun S, Aydin K. Large-area, lithography-free super absorbers and color filters at visible frequencies using ultrathin metallic films. *ACS Photonics* **2**, 183–188 (2015).
58. Fu R, Chen KX, Li ZL et al. Metasurface-based nanoprinting: principle, design and advances. *Opto-Electron Sci* **1**, 220011 (2022).
59. Wang DY, Liu ZY, Wang HZ et al. Structural color generation: from layered thin films to optical metasurfaces. *Nanophotonics* **12**, 1019–1081 (2023).
60. Li MM, Lyu Q, Peng BL et al. Bioinspired colloidal photonic composites: fabrications and emerging applications. *Adv Mater* **34**, 2110488 (2022).
61. Wu PP, Wang JX, Jiang L. Bio-inspired photonic crystal patterns. *Mater Horiz* **7**, 338–365 (2020).
62. Kim JB, Lee SY, Lee JM et al. Designing structural-color patterns composed of colloidal arrays. *ACS Appl Mater Interfaces* **11**, 14485–14509 (2019).
63. Li ZW, Fan QS, Yin YD. Colloidal self-assembly approaches to smart nanostructured materials. *Chem Rev* **122**, 4976–5067 (2022).
64. Wang L, Wang T, Yan RQ et al. Color printing and encryption with polarization-switchable structural colors on all-dielectric metasurfaces. *Nano Lett* **23**, 5581–5587 (2023).
65. Li KX, Li TY, Zhang TL et al. Facile full-color printing with a single transparent ink. *Sci Adv* **7**, eabh1992 (2021).
66. Ma W, Kou YS, Zhao P et al. Bioinspired structural color patterns derived from 1D photonic crystals with high saturation and brightness for double anti-counterfeiting decoration. *ACS Appl Polym Mater* **2**, 1605–1613 (2020).
67. Park CS, Lee SS. Vivid coloration and broadband perfect absorption based on asymmetric Fabry-Pérot nanocavities incorporating platinum. *ACS Appl Nano Mater* **4**, 4216–4225 (2021).
68. Li GH, Wu MX, Ye XY et al. Template-electrodeposited plasmonic metasurfaces for high-sensitivity biomolecular detection. *Adv Mater Interfaces* **9**, 2200292 (2022).
69. Meng FT, Wang ZZ, Zhang SF et al. Flexible photonic composites with responsive information display based on optical path control. *Chem Eng J* **466**, 143286 (2023).
70. Kou DH, Lin RC, Li C et al. Bioinspired bowl-array enabled angle-independent and fast responsive photonic colors for environmental sensing. *Chem Eng J* **430**, 132805 (2022).
71. Meng FT, Ju BZ, Wang ZZ et al. Bioinspired polypeptide photonic films with tunable structural color. *J Am Chem Soc* **144**, 7610–7615 (2022).
72. Kashem MNH, Gardner K, Momota MR et al. Deciphering the correlation between color response, temperature, and relative humidity in a photo-patternable polymeric nanofilm for tunable multimodal display. *Chem Eng J* **463**, 142333 (2023).
73. Liu X, Huang Z, Zang JF. All-dielectric silicon nanoring metasurface for full-color printing. *Nano Lett* **20**, 8739–8744 (2020).
74. Yang ZM, Chen YQ, Zhou YM et al. Microscopic interference full-color printing using grayscale-patterned Fabry–Perot resonance cavities. *Adv Opt Mater* **5**, 1700029 (2017).
75. Mao P, Liu CX, Song FQ et al. Manipulating disordered plasmonic systems by external cavity with transition from broadband absorption to reconfigurable reflection. *Nat Commun* **11**, 1538 (2020).
76. He QL, Ku KH, Vijayamohanan H et al. Switchable full-color reflective photonic ellipsoidal particles. *J Am Chem Soc* **142**, 10424–10430 (2020).
77. Wu Y, Sun RK, Ren J et al. Bioinspired dynamic camouflage in programmable thermochromic-patterned photonic films for sophisticated anti-counterfeiting. *Adv Funct Mater* **33**, 2210047 (2023).
78. He J, Shen XQ, Li HT et al. Scalable and sensitive humidity-responsive polymer photonic crystal films for anticounterfeiting application. *ACS Appl Mater Interfaces* **14**, 27251–27261 (2022).
79. Chen K, Fu QQ, Ye SY et al. Multicolor printing using electric-field-responsive and photocurable photonic crystals. *Adv Funct Mater* **27**, 1702825 (2017).
80. Puzzo DP, Arsenault AC, Manners I et al. Electroactive inverse opal: a single material for all colors. *Angew Chem Int Ed* **121**, 961–965 (2009).
81. Liao JL, Zhu C, Gao BB et al. Multiresponsive elastic colloidal crystals for reversible structural color patterns. *Adv Funct Mater* **29**, 1902954 (2019).
82. Xi W, Lee YJ, Yu S et al. Ultrahigh-efficient material informatics inverse design of thermal metamaterials for visible-infrared-compatible camouflage. *Nat Commun* **14**, 4694 (2023).
83. Lee KT, Han SY, Li ZJ et al. Flexible high-color-purity structural color filters based on a higher-order optical resonance suppression. *Sci Rep* **9**, 14917 (2019).
84. Lai XT, Peng JS, Cheng QF et al. Bioinspired color switchable photonic crystal silicone elastomer kirigami. *Angew Chem Int Ed* **60**, 14307–14312 (2021).
85. Wang JQ, Pang F, Fu QQ et al. Fabrication of anti-counterfeiting patterns with angle-dependent colors by silkscreen printing and UV-curable photonic crystal inks. *Sci China Mater* **66**, 1623–1631 (2022).
86. Kim GH, An T, Lim G. Bioinspired structural colors fabricated with ZnO quasi-ordered nanostructures. *ACS Appl Mater Interfaces* **9**, 19057–19062 (2017).

87. Zhang YX, Han P, Zhou HY et al. Highly brilliant noniridescent structural colors enabled by graphene nanosheets containing graphene quantum dots. *Adv Funct Mater* **28**, 1802585 (2018).
88. Goodling AE, Nagelberg S, Kaehr B et al. Colouration by total internal reflection and interference at microscale concave interfaces. *Nature* **566**, 523–527 (2019).
89. Lapidas V, Zhizhchenko A, Pustovalov E et al. Direct laser printing of high-resolution physically unclonable function anti-counterfeit labels. *Appl Phys Lett* **120**, 261104 (2022).
90. Hou XY, Vogelbacher F, Lai XT et al. Bioinspired multichannel colorful encryption through kirigami activating grating. *Sci Bull* **68**, 276–283 (2023).
91. Zhou MX, Jin F, Wang JY et al. Dynamic color-switching of hydrogel micropillar array under ethanol vapor for optical encryption. *Small* **19**, 2304384 (2023).
92. Koirala I, Shrestha VR, Park CS et al. Polarization-controlled broad color palette based on an ultrathin one-dimensional resonant grating structure. *Sci Rep* **7**, 40073 (2017).
93. Yang L, Hong XR, Li JF et al. Rechargeable metasurfaces for dynamic color display based on a compositional and mechanical dual-altered mechanism. *Research* **2022**, 9828757 (2022).
94. Liao JL, Ye CQ, Guo J et al. 3D-printable colloidal photonic crystals. *Mater Today* **56**, 29–41 (2022).
95. Cui XM, Zhu XL, Shao L et al. Plasmonic color laser printing inside transparent gold nanodisk-embedded poly(dimethylsiloxane) matrices. *Adv Opt Mater* **8**, 1901605 (2020).
96. Yue YF, Gong JP. Tunable one-dimensional photonic crystals from soft materials. *J Photochem Photobiol C Photochem Rev* **23**, 45–67 (2015).
97. Joannopoulos JD, Johnson SG, Winn JN et al. *Photonic crystals: molding the flow of light* 2nd ed (princeton university press, princeton, 2008).
98. Xuan ZY, Li JY, Liu QQ et al. Artificial structural colors and applications. *Innovation* **2**, 100081 (2021).
99. Qi D, Wang X, Cheng YZ et al. Design and characterization of one-dimensional photonic crystals based on ZnS/Ge for infrared-visible compatible stealth applications. *Opt Mater* **62**, 52–56 (2016).
100. Hao KZ, Wang X, Zhou L et al. Design of one-dimensional composite photonic crystal with high infrared reflectivity and low microwave reflectivity. *Optik* **216**, 164794 (2020).
101. Bonifacio LD, Lotsch BV, Puzzo DP et al. Stacking the nanochemistry deck: structural and compositional diversity in one-dimensional photonic crystals. *Adv Mater* **21**, 1641–1646 (2009).
102. Wang F, Cheng YZ, Wang X et al. Effective modulation of the photonic band gap based on Ge/ZnS one-dimensional photonic crystal at the infrared band. *Opt Mater* **75**, 373–378 (2018).
103. Su YR, Deng ZC, Qin W et al. Adaptive infrared camouflage based on quasi-photonic crystal with $Ge_2Sb_2Te_5$. *Opt Commun* **497**, 127203 (2021).
104. Park CS, Shrestha VR, Lee SS et al. Trans-reflective color filters based on a phase compensated etalon enabling adjustable color saturation. *Sci Rep* **6**, 25496 (2016).
105. Feng L, Huo PC, Liang YZ et al. Photonic metamaterial absorbers: morphology engineering and interdisciplinary applications. *Adv Mater* **32**, e1903787 (2020).
106. Chen J, Song G, Cong S et al. Resonant-cavity-enhanced electrochromic materials and devices. *Adv Mater* **35**, e2300179 (2023).
107. Li ZY, Palacios E, Butun S et al. Omnidirectional, broadband light absorption using large-area, ultrathin lossy metallic film coatings. *Sci Rep* **5**, 15137 (2015).
108. Chen J, Wang Z, Liu CL et al. Mimicking nature's butterflies: electrochromic devices with dual-sided differential colorations. *Adv Mater* **33**, e2007314 (2021).
109. Wu Q, Wang XY, Sun PY et al. Electrochromic metamaterials of metal-dielectric stacks for multicolor displays with high color purity. *Nano Lett* **21**, 6891–6897 (2021).
110. Chen J, Li YW, Zhang TY et al. Reversible active switching of fano and Fabry–Pérot resonances by electrochromic operation. *Laser Photonics Rev* **16**, 2200303 (2022).
111. Wang Z, Wang XY, Cong S et al. Towards full-colour tunability of inorganic electrochromic devices using ultracompact Fabry-Perot nanocavities. *Nat Commun* **11**, 302 (2020).
112. Wen CY, Zhao B, Liu YH et al. Flexible mxene-based composite films for multi-spectra defense in radar, infrared and visible light bands. *Adv Funct Mater* **33**, 2214223 (2023).
113. Zhang XS, Hou K, Sun YQ et al. Bioinspired microplate arrays for magnetically tuned dynamic color. *Adv Opt Mater* **10**, 2200763 (2022).
114. Gao PQ, He J, Zhou SQ et al. Large-area nanosphere self-assembly by a micro-propulsive injection method for high throughput periodic surface nanotexturing. *Nano Lett* **15**, 4591–4598 (2015).
115. Hu LW, Liu XH, Liu CT et al. Self-assembly fabrication and applications of photonic crystal structure color materials. *Acta Chim Sinica* **81**, 809–819 (2023).
116. Zhang ZH, Chen ZY, Shang LR et al. Structural color materials from natural polymers. *Adv Mater Technol* **6**, 2100296 (2021).
117. Li WW, Xu MZ, Xu HX et al. Metamaterial absorbers: from tunable surface to structural transformation. *Adv Mater* **34**, 2202509 (2022).
118. Hsieh CH, Lu YC, Yang HT. Self-assembled mechanochromic shape memory photonic crystals by doctor blade coating. *ACS Appl Mater Interfaces* **12**, 36478–36484 (2020).
119. Lan NXV, Moon J, Kang TH et al. Index-matched composite colloidal crystals of core–shell particles for strong structural colors and optical transparency. *Chem Mater* **33**, 1714–1722 (2021).
120. Huang K, Li QW, Xue YF et al. Application of colloidal photonic crystals in study of organoids. *Adv Drug Delivery Rev* **201**, 115075 (2023).
121. Fan QS, Li ZW, Li YC et al. Unveiling enhanced electrostatic repulsion in silica nanosphere assembly: formation dynamics of body-centered-cubic colloidal crystals. *J Am Chem Soc* **145**, 28191–28203 (2023).
122. Roemling LJ, Bleyer G, Goerlitzer ESA et al. Quantitative optical and structural comparison of 3D and (2+1)D colloidal photonic crystals. *Langmuir* **39**, 5211–5221 (2023).
123. Xie AQ, Li Q, Xi YR et al. Assembly of crack-free photonic crystals: fundamentals, emerging strategies, and perspectives. *Acc Mater Res* **4**, 403–415 (2023).
124. Li YC, Wang XH, Hu MG et al. Patterned SiO_2/polyurethane acrylate inverse opal photonic crystals with high color saturation and tough mechanical strength. *Langmuir* **35**, 14282–14290 (2019).
125. Zhang X, Fu QQ, Ge JP. Triple-state invisible photonic crystal pattern encrypted in hollow-silica/polyurethane film for anti-

counterfeiting applications. *Adv Photonics* **2**, 2000208 (2021).
126. Fu FF, Shang LR, Chen ZY et al. Bioinspired living structural color hydrogels. *Sci Robot* **3**, eaar8580 (2018).
127. Fu FF, Chen ZY, Zhao Z et al. Bio-inspired self-healing structural color hydrogel. *Proc Natl Acad Sci USA* **114**, 5900–5905 (2017).
128. Wang C, Lin X, Schäfer CG et al. Spray synthesis of photonic crystal based automotive coatings with bright and angular-dependent structural colors. *Adv Funct Mater* **31**, 2008601 (2021).
129. He YY, Liu LY, Fu QQ et al. Precise assembly of highly crystalline colloidal photonic crystals inside the polyester yarns: a spray coating synthesis for breathable and durable fabrics with saturated structural colors. *Adv Funct Mater* **32**, 2200330 (2022).
130. Ko YL, Tsai HP, Lin KY et al. Reusable macroporous photonic crystal-based ethanol vapor detectors by doctor blade coating. *J Colloid Interface Sci* **487**, 360–369 (2017).
131. Lee YH, Won Y, Mun J et al. Hierarchically manufactured chiral plasmonic nanostructures with gigantic chirality for polarized emission and information encryption. *Nat Commun* **14**, 7298 (2023).
132. Wang ZH, Zhang JH, Li JX et al. Colorful detection of organic solvents based on responsive organic/inorganic hybrid one-dimensional photonic crystals. *J Mater Chem* **21**, 1264–1270 (2011).
133. Daqiqeh Rezaei S, Dong ZG, Wang H et al. Tri-functional metasurface enhanced with a physically unclonable function. *Mater Today* **62**, 51–61 (2023).
134. Wang YN, Li XY, Zhang YL et al. Structural coloration of textiles with PMMA photonic crystals. *J Mater Chem C* **12**, 254–261 (2024).
135. Minh NH, Kim K, Kang DH et al. Anti-counterfeiting labels of photonic crystals with versatile structural colors. *Nanoscale Adv* **6**, 5853–5860 (2024).
136. Tian ZQ, Zhu JY, Guo QL et al. Ultra-bright stimuli-responsive photonic crystals for high-performance anticounterfeiting coatings. *Adv Opt Mater* **12**, 2402776 (2024).
137. Zhang X, Zhang ZY, Long J et al. Vapor absorption and liquefication triggered dynamic color changes and pattern conversions on photonic crystal films for anticounterfeiting. *ACS Appl Mater Interfaces* **16**, 61360–61370 (2024).
138. Yue YF, Kurokawa T, Haque MA et al. Mechano-actuated ultrafast full-colour switching in layered photonic hydrogels. *Nat Commun* **5**, 4659 (2014).
139. Qin M, Sun M, Bai RB et al. Bioinspired hydrogel interferometer for adaptive coloration and chemical sensing. *Adv Mater* **30**, 1800468 (2018).
140. Tong LP, Qi W, Wang MF et al. Tunable design of structural colors produced by pseudo-1D photonic crystals of graphene oxide. *Small* **12**, 3433–3443 (2016).
141. Hou J, Zhang HC, Su B et al. Four-dimensional screening anticounterfeiting pattern by inkjet printed photonic crystals. *Chem Asian J* **11**, 2680–2685 (2016).
142. Wu MF, Zhang CY, Wei FJ et al. A self-assembly based on a hydrogel interface: facile, rapid, and large-scale preparation of colloidal photonic crystals. *Mater Chem Front* **4**, 2409–2417 (2020).
143. Zhou CT, Qi Y, Zhang SF et al. Rapid fabrication of vivid noniridescent structural colors on fabrics with robust structural stability by screen printing. *Dyes Pigm* **176**, 108226 (2020).
144. Hsu CW, Zhen B, Qiu WJ et al. Transparent displays enabled by resonant nanoparticle scattering. *Nat Commun* **5**, 3152 (2014).
145. Zhou CT, Qi Y, Zhang SF et al. Lotus seedpod inspiration: particle-nested double-inverse opal films with fast and reversible structural color switching for information security. *ACS Appl Mater Interfaces* **13**, 26384–26393 (2021).
146. Chung K, Yu S, Heo CJ et al. Flexible, angle-independent, structural color reflectors inspired by morpho butterfly wings. *Adv Mater* **24**, 2375–2379 (2012).
147. Lee HS, Shim TS, Hwang H et al. Colloidal photonic crystals toward structural color palettes for security materials. *Chem Mater* **25**, 2684–2690 (2013).
148. Li HT, Zhao GW, Zhu MJ et al. Robust large-sized photochromic photonic crystal film for smart decoration and anticounterfeiting. *ACS Appl Mater Interfaces* **14**, 14618–14629 (2022).
149. Huang HW, Li HT, Yin JM et al. Butterfly-inspired tri-state photonic crystal composite film for multilevel information encryption and anti-counterfeiting. *Adv Mater* **35**, e2211117 (2023).
150. Yan JY, Lin YB, Li JX et al. A convenient, environmental-friendly, panchromatic adjustable, re-writable photonic paper and its optical anti-counterfeiting application. *Chem Eng Sci* **288**, 119818 (2024).
151. Wei W, Dong B, Cao L et al. Fabrication of angle-independent anti-reflective structural color coating powders. *Mater Today Phys* **17**, 100361 (2021).
152. Wang Y, Guo JH, Sun LY et al. Dual-responsive graphene hybrid structural color hydrogels as visually electrical skins. *Chem Eng J* **415**, 128978 (2021).
153. Hu HB, Zhong H, Chen CL et al. Magnetically responsive photonic watermarks on banknotes. *J Mater Chem C* **2**, 3695–3702 (2014).
154. Luo W, Ma HR, Mou FZ et al. Steric-repulsion-based magnetically responsive photonic crystals. *Adv Mater* **26**, 1058–1064 (2014).
155. Huang C, Zhang HB, Yang SY et al. Controllable structural colored screen for real-time display via near-infrared light. *ACS Appl Mater Interfaces* **12**, 20867–20873 (2020).
156. He L, Wang MS, Ge JP et al. Magnetic assembly route to colloidal responsive photonic nanostructures. *Acc Chem Res* **45**, 1431–1440 (2012).
157. Jung C, Kim SJ, Jang J et al. Disordered-nanoparticle–based etalon for ultrafast humidity-responsive colorimetric sensors and anti-counterfeiting displays. *Sci Adv* **8**, eabm8598 (2022).
158. Rui GH, Ding CC, Gu B et al. Symmetric $Ge_2Sb_2Te_5$ based metamaterial absorber induced dynamic wide-gamut structural color. *J Opt* **22**, 085003 (2020).
159. Cheng T, Ma YK, Zhao HH et al. Dynamic tuning of optical absorbance and structural color of VO_2-based metasurface. *Nanophotonics* **12**, 3121–3133 (2023).
160. Quan C, Gu S, Zou JL et al. Phase change metamaterial for tunable infrared stealth and camouflage. *Opt Express* **30**, 43741–43751 (2022).
161. Ma HR, Zhu MX, Luo W et al. Free-standing, flexible thermochromic films based on one-dimensional magnetic photonic crystals. *J Mater Chem C* **3**, 2848–2855 (2015).
162. Yang SY, Li J, Wei J. A real-time temperature responsive material based on partial inverse opal photonic crystals and

cholesteric liquid crystals. *Opt Mater* **124**, 111992 (2022).
163. Gyu Hwang T, Woo Cho D, Hwang DH et al. Forensic-level security using non-imitable anticounterfeiting films: humidity-sensitive 1D photonic crystals with UV-tunable color response and their encryption using small aldehydes. *Chem Eng J* **473**, 145448 (2023).
164. Yu WY, Zhao YX, Ge JP. Electrically triggered photonic crystal anti-counterfeiting tags with multi-level response fabricated by regioselective modification of ITO electrode surface. *J Colloid Interface Sci* **659**, 603–610 (2024).
165. Hu Y, Yu SY, Wei BR et al. Stimulus-responsive nonclose-packed photonic crystals: fabrications and applications. *Mater Horiz* **10**, 3895–3928 (2023).
166. Wang JQ, Yin T, Ge JP. A disposable thermally triggered photonic crystal anti-counterfeiting tag with irreversible response and multi-step color changes. *Small* **20**, 2311308 (2024).
167. Deng J, Fu SG, Zhong YF et al. Photonic crystal hydrogels fabricated from nanoparticles of Fe_3O_4/SiO_2 with programmable colors through photopolymerization for applications as anticounterfeiting applications. *ACS Appl Nano Mater* **7**, 7916–7924 (2024).
168. Meng ZP, Liu YK, Huang HF et al. Flexible self-supporting photonic crystals: Fabrications and responsive structural colors. *Adv Colloid Interface Sci* **333**, 103272 (2024).
169. Wu Y, Sun RK, Han YQ et al. Ultrathin photonic crystal film with supersensitive thermochromism in air. *Chem Eng J* **451**, 139075 (2023).
170. Zhang ZL, Dong X, Fan YN et al. Chameleon-inspired variable coloration enabled by a highly flexible photonic cellulose film. *ACS Appl Mater Interfaces* **12**, 46710–46718 (2020).
171. Liu FF, Zhang SF, Meng Y et al. Thermal responsive photonic crystal achieved through the control of light path guided by phase transition. *Small* **16**, 2002319 (2020).
172. Li HT, Zhu MJ, Tian F et al. Polychrome photonic crystal stickers with thermochromic switchable colors for anti-counterfeiting and information encryption. *Chem Eng J* **426**, 130683 (2021).
173. Meng ZP, Wu SL, Tang BT et al. Structurally colored polymer films with narrow stop band, high angle-dependence and good mechanical robustness for trademark anti-counterfeiting. *Nanoscale* **10**, 14755–14762 (2018).
174. Yan YY, Zheng JZ, Wu J et al. Bioinspired artificial photonic nanocrystal skin with high sensitivity and mechanical color change properties for camouflage and visual transmission. *ACS Appl Nano Mater* **7**, 5329–5338 (2024).
175. Wei BR, Zhang ZK, Yang DP et al. Lattice transformation-induced retroreflective structural colors. *ACS Appl Mater Interfaces* **15**, 47350–47358 (2023).
176. Yu SY, Ma DK, Qi CZ et al. All-in-one photonic crystals with multi-stimuli-chromic, color-recordable, self-healable, and adhesive functions. *Adv Funct Mater* **34**, 2411670.
177. Wang XH, Qiu YF, Chen G et al. Self-healable poly(vinyl alcohol) photonic crystal hydrogel. *ACS Appl Polym Mater* **2**, 2086–2092 (2020).
178. Yin SN, Liu J, Wu DF et al. Robust self-healing magnetically induced colloidal photonic crystal hydrogels. *ACS Appl Polym Mater* **2**, 448–454 (2020).
179. Tao J, Lu XH. Tetraphenylbenzene-modified photonic crystal structure colour coating on fabric substrates for dual-mode anticounterfeiting. *Colloids Surf A Physicochem Eng Aspects* **655**, 130044 (2022).
180. Yu ZM, Zhao K, Zhao YB et al. Biomimetic intelligent photonic crystal composite films with tri-mode optical states for advanced anti-counterfeiting and information encryption. *J Mater Chem C* **11**, 16527–16535 (2023).
181. Chen YP, Lou ZZ, Chen ZH et al. Magnetic–fluorescent responsive Janus photonic crystal beads for self-destructive anti-counterfeiting. *Langmuir* **38**, 14387–14399 (2022).
182. Lu YM, Xia X, Guo YX et al. Carbon dots/SiO_2 fluorescent photonic crystals for anti-counterfeiting. *ACS Appl Nano Mater* **7**, 6547–6555 (2024).
183. Xu CJ, Huang CG, Yang DP et al. Photo-luminescent photonic crystals for anti-counterfeiting. *ACS Omega* **7**, 7320–7326 (2022).
184. Wang M, Li XS, Yang H et al. Mechanochromic 3D soft photonic crystals enabled anticounterfeiting and encryption information storage. *Adv Opt Mater* **13**, 2401934.
185. Wu JY, Li JW, Liu XC et al. Unclonable photonic crystal hydrogels with controllable encoding capacity for anticounterfeiting. *ACS Appl Mater Interfaces* **14**, 2369–2380 (2022).
186. Gao YF, Ge KY, Zhang Z et al. Fine optimization of colloidal photonic crystal structural color for physically unclonable multiplex encryption and anti-counterfeiting. *Adv Sci* **11**, 2305876 (2024).
187. Sydney Gladman A, Matsumoto EA, Nuzzo RG et al. Biomimetic 4D printing. *Nat Mater* **15**, 413–418 (2016).
188. Ding Z, Yuan C, Peng XR et al. Direct 4D printing via active composite materials. *Sci Adv* **3**, e1602890 (2017).
189. Li LJ, Li H, Hu HK et al. Full-color and anti-counterfeit printings with all-dielectric chiral metasurfaces. *Photonics* **10**, 401 (2023).
190. Wilson K, Marocico CA, Pedrueza-Villalmanzo E et al. Plasmonic colour printing by light trapping in two-metal nanostructures. *Nanomaterials* **9**, 963 (2019).
191. Li LY, Jin SX, Hu SY et al. Optical metasurfaces for multiplex high-performance grating-type structural colors. *Opt Lett* **48**, 1686–1689 (2023).
192. Shang X, Niu JB, Li H et al. Polarization-sensitive structural colors based on anisotropic silicon metasurfaces. *Photonics* **10**, 448 (2023).
193. Wang P, Su JC, Ding P et al. Graphene-metal based tunable radiative metasurface for information encryption and anticounterfeiting. *Diamond Relat Mater* **131**, 109548 (2023).
194. Li ZL, Dai Q, Deng LG et al. Structural-color nanoprinting with hidden watermarks. *Opt Lett* **46**, 480–483 (2021).
195. Zhao NX, Li ZL, Zhu GD et al. Tri-channel metasurface for watermarked structural-color nanoprinting and holographic imaging. *Opt Express* **30**, 37554–37565 (2022).
196. Li ZF, Premaratne M, Zhu WR. Advanced encryption method realized by secret shared phase encoding scheme using a multi-wavelength metasurface. *Nanophotonics* **9**, 3687–3696 (2020).
197. Yuan H, Zhong ZQ, Zhang YH et al. Multi-channel image encryption based on an all-dielectric metasurface incorporating near-field nanoprinting and far-field holography. *Adv Opt Mater* **11**, 2300352 (2023).
198. Deng J, Li ZL, Li JX et al. Metasurface-assisted optical encryption carrying camouflaged information. *Adv Opt Mater* **10**, 2200949 (2022).
199. Kim I, Jang J, Kim G et al. Pixelated bifunctional metasurface-

driven dynamic vectorial holographic color prints for photonic security platform. *Nat Commun* **12**, 3614 (2021).
200. Sun S, Zhou ZX, Zhang C et al. All-dielectric full-color printing with TiO_2 metasurfaces. *ACS Nano* **11**, 4445–4452 (2017).
201. Wen XX, Lu XG, Li JN et al. Multi-responsive, flexible, and structurally colored film based on a 1D diffraction grating structure. *iScience* **25**, 104157 (2022).
202. Hong YF, Lei YF, Fang XM et al. All-dielectric high saturation structural colors with Si_3N_4 metasurface. *Mod Phys Lett B* **34**, 2050142 (2020).
203. Kim Y, Hyun JK. Encoding Mie, plasmonic, and diffractive structural colors in the same pixel. *Nanophotonics* **12**, 3341–3349 (2023).
204. Gu JT, Liu Y, Meng NN et al. Structural colors based on diamond metasurface for information encryption. *Adv Opt Mater* **11**, 2202826 (2023).
205. Wei YX, Zhao M, Yang ZY. Silicon metasurface embedded Fabry-Perot cavity enables the high-quality transmission structural color. *Opt Lett* **47**, 5344–5347 (2022).
206. Li HX, Xu YL, Zhang X et al. All-dielectric high saturation structural colors enhanced by multipolar modulated metasurfaces. *Opt Express* **30**, 28954–28965 (2022).
207. Li LL, Ruan HX, Liu C et al. Machine-learning reprogrammable metasurface imager. *Nat Commun* **10**, 1082 (2019).
208. Liu XH, Wang P, Xiao CY et al. Compatible stealth metasurface for laser and infrared with radiative thermal engineering enabled by machine learning. *Adv Funct Mater* **33**, 2212068 (2023).
209. Zhang RZ, Guo YH, Zhang F et al. Dual-layer metasurface enhanced capacity of polarization multiplexing. *Laser Photonics Rev* **18**, 2400126 (2024).
210. Wang QS, Fang Y, Meng Y et al. Vortex-field enhancement through high-threshold geometric metasurface. *Opto-Electron Adv* **7**, 240112 (2024).
211. Li XT, Cai XD, Liu C et al. Cascaded metasurfaces enabling adaptive aberration corrections for focus scanning. *Opto-Electron Adv* **7**, 240085 (2024).
212. Xin W, Jiang HB, Sun TQ et al. Optical anisotropy of black phosphorus by total internal reflection. *Nano Mater Sci* **1**, 304–309 (2019).
213. Li RJ, Li KX, Deng X et al. Dynamic high-capacity structural-color encryption via inkjet printing and image recognition. *Adv Funct Mater* **34**, 2404706 (2024).
214. Shanker R, Sardar S, Chen SZ et al. Noniridescent biomimetic photonic microdomes by inkjet printing. *Nano Lett* **20**, 7243–7250 (2020).
215. Zhu HZ, Li Q, Tao CN et al. Multispectral camouflage for infrared, visible, lasers and microwave with radiative cooling. *Nat Commun* **12**, 1805 (2021).
216. Yuan X, Xu W, Huang F et al. Structural colour of polyester fabric coated with Ag/TiO_2 multilayer films. *Surf Eng* **33**, 231–236 (2017).
217. Chen FL, Wang SW, Liu XX et al. High performance colored selective absorbers for architecturally integrated solar applications. *J Mater Chem A* **3**, 7353–7360 (2015).
218. Lu TW, Lin Y, Zhang TQ et al. Self-polarized RGB device realized by semipolar micro-LEDs and perovskite-in-polymer films for backlight applications. *Opto-Electron Adv* **7**, 230210 (2024).
219. Badloe T, Kim J, Kim I et al. Liquid crystal-powered Mie resonators for electrically tunable photorealistic color gradients and dark blacks. *Light Sci Appl* **11**, 118 (2022).
220. Li SQ, Song WZ, Ye M et al. Generalized method of images and reflective color generation from ultrathin multipole resonators. *ACS Photonics* **5**, 2374–2383 (2018).
221. Geng GZ, Pan RH, Li CS et al. Height-gradiently-tunable nanostructure arrays by grayscale assembly nanofabrication for ultra-realistic imaging. *Laser Photonics Rev* **17**, 2300073 (2023).
222. Lin J, Luo SW, Zuo DL et al. Multilayer structure for highly transmissive angle-tolerant color filter. *Opt Commun* **427**, 158–162 (2018).
223. Gao HX, Liang YZ, Li R et al. Eye-friendly reflective structural colors with shortwave infrared shielding. *Adv Opt Mater* **10**, 2101342 (2022).
224. Shen YC, Rinnerbauer V, Wang I et al. Structural colors from fano resonances. *ACS Photonics* **2**, 27–32 (2015).
225. Park JG, Jeong YH, Ji S et al. Multimodal wrinkle micro-nanoarchitectonics by patterned surface material properties for transformative structural coloration. *Adv Opt Mater* **11**, 2300279 (2023).
226. Miller BH, Liu H, Kolle M. Scalable optical manufacture of dynamic structural colour in stretchable materials. *Nat Mater* **21**, 1014–1018 (2022).
227. Li B, Wu YH, Sun Y et al. Switchable and tunable chemical/structure color in a flexible hierarchical surface. *Adv Intell Syst* **6**, 2200415 (2023).
228. Lyu P, Gong T, Rebello Sousa Dias M et al. Transient structural colors with magnesium-based reflective filters. *Adv Opt Mater* **10**, 2200159 (2022).
229. Chang HK, Park J. Flexible all-solid-state electrically tunable photonic crystals. *Adv Opt Mater* **6**, 1800792 (2018).
230. Han MG, Heo CJ, Shim H et al. Structural color manipulation using tunable photonic crystals with enhanced switching reliability. *Adv Opt Mater* **2**, 535–541 (2014).
231. Li QL, Li XL, Wang W et al. Magnetic nanoparticles modified by citrate groups for magnetically responsive photonic crystals. *J Phys Chem Solids* **122**, 278–283 (2018).
232. Li YL, Lu XG, Yang S. Preparation and properties of silver-deposited magnetically responsive colloidal photonic crystals for significant fluorescence enhancement. *Opt Mater* **122**, 111815 (2021).
233. Li Y, Long Y, Yang GQ et al. Tunable amplified spontaneous emission based on liquid magnetically responsive photonic crystals. *J Mater Chem C* **7**, 3740–3743 (2019).
234. Pan LT, Peng Z, Yu HR et al. Robust synthesis of highly charged superparamagnetic Fe_3O_4 colloidal nanocrystal clusters for magnetically responsive photonic crystals. *New J Chem* **45**, 16511–16519 (2021).
235. Xu JS, Zhao Q, Hu TY et al. Rapid preparation of size-tunable Fe_3O_4@SiO_2 nanoparticles to construct magnetically responsive photonic crystals. *J Nanopart Res* **23**, 232 (2021).
236. Li YL, Chen X, Geng HK et al. Oxidation control of bottlebrush molecular conformation for producing libraries of photonic structures. *Angew Chem Int Ed* **60**, 3647–3653 (2021).
237. Park TH, Eoh H, Jung Y et al. Thermo-adaptive block copolymer structural color electronics. *Adv Funct Mater* **31**, 2008548 (2021).
238. Sun LY, Wang Y, Bian FK et al. Bioinspired optical and electrical dual-responsive heart-on-a-chip for hormone testing. *Sci*

Bull **68**, 938–945 (2023).
239. Fu FF, Shang LR, Zheng FY et al. Cells cultured on core-shell photonic crystal barcodes for drug screening. *ACS Appl Mater Interfaces* **8**, 13840–13848 (2016).
240. Xing HH, Li J, Guo JB et al. Bio-inspired thermal-responsive inverse opal films with dual structural colors based on liquid crystal elastomer. *J Mater Chem C* **3**, 4424–4430 (2015).
241. Dai CJ, Li ZL, Li Z et al. Direct-printing hydrogel-based platform for humidity-driven dynamic full-color printing and holography. *Adv Funct Mater* **33**, 2212053 (2023).
242. Zhao YJ, Shang LR, Cheng Y et al. Spherical colloidal photonic crystals. *Acc Chem Res* **47**, 3632–3642 (2014).
243. Zhao YJ, Zhao XW, Pei XP et al. Multiplex detection of tumor markers with photonic suspension array. *Anal Chim Acta* **633**, 103–108 (2009).
244. Zheng FY, Cheng Y, Wang J et al. Aptamer-functionalized barcode particles for the capture and detection of multiple types of circulating tumor cells. *Adv Mater* **26**, 7333–7338 (2014).
245. Kim I, Kim H, Han S et al. Metasurfaces-driven hyperspectral imaging via multiplexed plasmonic resonance energy transfer. *Adv Mater* **35**, e2300229 (2023).
246. Zhang DG, Bian FK, Cai LJ et al. Bioinspired photonic barcodes for multiplexed target cycling and hybridization chain reaction. *Biosens Bioelectron* **143**, 111629 (2019).
247. Bian FK, Chen HX, Sun LY et al. AIEgens-integrated structural color barcodes for binary screening of microRNAs. *Chem Eng J* **471**, 144800 (2023).
248. Zhao Z, Wang H, Shang LR et al. Bioinspired heterogeneous structural color stripes from capillaries. *Adv Mater* **29**, 1704569 (2017).
249. Zheng H, Li J, Song WZ et al. Thermal-responsive photonic crystals based on physically cross-linked inverse opal nanocomposite hydrogels. *J Wuhan Univ Technol Mater Sci Ed* **36**, 289–296 (2021).
250. Ueno K, Matsubara K, Watanabe M et al. An electro- and thermochromic hydrogel as a full-color indicator. *Adv Mater* **19**, 2807–2812 (2007).
251. Wang XQ, Yang SY, Wang CF et al. Multifunctional hydrogels with temperature, ion, and magnetocaloric stimuli-responsive performances. *Macromol Rapid Commun* **37**, 759–768 (2016).
252. Zhang ZH, Chen ZY, Sun LY et al. Bio-inspired angle-independent structural color films with anisotropic colloidal crystal array domains. *Nano Res* **12**, 1579–1584 (2019).
253. Cai LJ, Wang Y, Sun LY et al. Bio-inspired multi-responsive structural color hydrogel with constant volume and wide viewing angles. *Adv Opt Mater* **9**, 2100831 (2021).
254. Xu MH, Liang SZ, Zhang WQ et al. Biomimetic color-changing skin based on temperature-responsive hydrogel microspheres with the photonic crystal structure. *J Polym Sci* **61**, 100–107 (2023).
255. Xiong MY, Sheng YH, Di YS et al. Power-free and self-cleaning solar light detector based on the temperature-sensitive structural color and photothermal effect. *ACS Appl Mater Interfaces* **13**, 33566–33573 (2021).
256. Liu FF, Zhang SF, Jin X et al. Thermal-responsive photonic crystal with function of color switch based on thermochromic system. *ACS Appl Mater Interfaces* **11**, 39125–39131 (2019).
257. Katsura C, Nobukawa S, Sugimoto H et al. Solvent-responsive coloring behavior of colloidal crystal films consisting of cross-linked polymer nanoparticles. *Colloid Polym Sci* **295**, 1709–1715 (2017).
258. Lim YS, Kim JS, Choi JH et al. Solvatochromic discrimination of alcoholic solvents by structural colors of polydopamine nanoparticle thin films. *Colloid Interface Sci Commun* **48**, 100624 (2022).
259. Wang YP, Niu WB, Zhang SF et al. Solvent responsive single-material inverse opal polymer actuator with structural color switching. *J Mater Sci* **55**, 817–827 (2020).
260. Zhang ZK, Wei BR, Yang DP et al. Artificial chameleon skins active mimicking reversible off/on structural colors of insect wings. *Adv Mater Interfaces* **9**, 2201252 (2022).
261. Sun S, Yang WH, Zhang C et al. Real-time tunable colors from microfluidic reconfigurable all-dielectric metasurfaces. *ACS Nano* **12**, 2151–2159 (2018).
262. Szendrei K, Jiménez-Solano A, Lozano G et al. Fluorescent humidity sensors based on photonic resonators. *Adv Opt Mater* **5**, 1700663 (2017).
263. Diao YY, Liu XY, Toh GW et al. Multiple structural coloring of silk-fibroin photonic crystals and humidity-responsive color sensing. *Adv Funct Mater* **23**, 5373–5380 (2013).
264. Xu JS, Hu TY, Zhao Q et al. Fe_3O_4@SiO_2/PAM/glycerol photonic crystal film as a long-term effective sensor for ambient humidity. *Mater Res Bull* **153**, 111895 (2022).
265. Kim J, Kim H, Kang H et al. A water-soluble label for food products prevents packaging waste and counterfeiting. *Nat Food* **5**, 293–300 (2024).
266. Ding M, Chen G, Xu WC et al. Bio-inspired synthesis of nanomaterials and smart structures for electrochemical energy storage and conversion. *Nano Mater Sci* **2**, 264–280 (2020).
267. Lan RC, Wang Q, Shen C et al. Humidity-induced simultaneous visible and fluorescence photonic patterns enabled by integration of covalent bonds and ionic crosslinks. *Adv Funct Mater* **31**, 2106419 (2021).
268. Bak JM, Kim Y, Park C et al. Dual-responsive photonic multilayers in combination with a smartphone application as high-security anti-counterfeiting devices. *Chem Eng J* **468**, 143631 (2023).
269. Delaney C, Qian J, Zhang X et al. Direct laser writing of vapour-responsive photonic arrays. *J Mater Chem C* **9**, 11674–11678 (2021).
270. Li C, Lotsch BV. Stimuli-responsive 2D polyelectrolyte photonic crystals for optically encoded pH sensing. *Chem Commun* **48**, 6169–6171 (2012).
271. Fei X, Lu T, Ma J et al. Bioinspired polymeric photonic crystals for high cycling pH-sensing performance. *ACS Appl Mater Interfaces* **8**, 27091–27098 (2016).
272. Luo W, Cui Q, Fang K et al. Responsive Hydrogel-based photonic nanochains for microenvironment sensing and imaging in real time and high resolution. *Nano Lett* **20**, 803–811 (2020).
273. Li WY, Zeng XZ, Dong YJ et al. Laser nanoprinting of floating three-dimensional plasmonic color in pH-responsive hydrogel. *Nanotechnology* **33**, 065302 (2022).
274. Zhang MM, Hou ZY, Liu SM et al. Temperature/pH dual-responsive reversible morphology evolution of block copolymer microparticles under three-dimensional confinement. *Sci China Chem* **66**, 3587–3593 (2023).
275. Couturier JP, Sütterlin M, Laschewsky A et al. Responsive inverse opal hydrogels for the sensing of macromolecules. *Angew Chem Int Ed* **54**, 6641–6644 (2015).
276. Wang Y, Zhang ZH, Chen HX et al. Bio-inspired shape-memo-

ry structural color hydrogel film. *Sci Bull* **67**, 512–519 (2022).
277. Xia YQ, Gao S, He H et al. A new and straightforward strategy to prepare an optical hydrogel film with dynamic structural colors. *J Phys Chem C* **124**, 16083–16089 (2020).
278. Xue H, Liu F, Wang Z et al. Bio-inspired dual-responsive photonic crystal with smart responsive hydrogel for pH and temperature detection. *Mater Des* **233**, 112242 (2023).
279. Kim Y, Kim SH, Girma HG et al. Dual responsive dependent background color based on thermochromic 1D photonic crystal multilayer films. *Polymers* **14**, 5330 (2022).
280. Shen HF, Lin Q, Tang HC et al. Fabrication of temperature- and alcohol-responsive photonic crystal hydrogel and its application for sustained drug release. *Langmuir* **38**, 3785–3794 (2022).
281. Li XK, Liu JZ, Zhang XX. Pressure/temperature dual-responsive cellulose nanocrystal hydrogels for on-demand schemochrome patterning. *Adv Funct Mater* **33**, 2306208 (2023).
282. Yan D, Lu W, Qiu LL et al. Thermal and stress tension dual-responsive photonic crystal nanocomposite hydrogels. *RSC Adv* **9**, 21202–21205 (2019).
283. Shen C, Wang ZZ, Huang R et al. Humidity-responsive photonic crystals with pH and SO_2 gas detection ability based on cholesteric liquid crystalline networks. *ACS Appl Mater Interfaces* **14**, 16764–16771 (2022).
284. Belmonte A, Ussembayev YY, Bus T et al. Dual light and temperature responsive micrometer-sized structural color actuators. *Small* **16**, e1905219 (2020).
285. Kim T, Lee JW, Park C et al. Self-powered finger motion-sensing structural color display enabled by block copolymer photonic crystal. *Nano Energy* **92**, 106688 (2022).
286. Xue JZ, Yao MN, Wang GY et al. An environmental perception self-adaptive discolorable hydrogel film toward sensing and display. *Adv Opt Mater* **9**, 2100116 (2021).
287. Chen CW, Wang Y, Zhang H et al. Responsive and self-healing structural color supramolecular hydrogel patch for diabetic wound treatment. *Bioact Mater* **15**, 194–202 (2022).
288. Nagasaki Y, Suzuki M, Hotta I et al. Control of Si-based all-dielectric printing color through oxidation. *ACS Photonics* **5**, 1460–1466 (2018).
289. Nagasaki Y, Hotta I, Suzuki M et al. Metal-masked Mie-resonant full-color printing for achieving free-space resolution limit. *ACS Photonics* **5**, 3849–3855 (2018).
290. Zhang YX, Zhang Q, Ouyang X et al. Ultrafast light-controlled growth of silver nanoparticles for direct plasmonic color printing. *ACS Nano* **12**, 9913–9921 (2018).
291. James TD, Mulvaney P, Roberts A. The plasmonic pixel: large area, wide gamut color reproduction using aluminum nanostructures. *Nano Lett* **16**, 3817–3823 (2016).
292. Roberts AS, Pors A, Albrektsen O et al. Subwavelength plasmonic color printing protected for ambient use. *Nano Lett* **14**, 783–787 (2014).
293. Tan SJ, Zhang L, Zhu D et al. Plasmonic color palettes for photorealistic printing with aluminum nanostructures. *Nano Lett* **14**, 4023–4029 (2014).
294. Huang Y, Zhu J, Jin SX et al. Polarization-controlled bifunctional metasurface for structural color printing and beam deflection. *Opt Lett* **45**, 1707–1710 (2020).
295. Wang L, Wang T, Yan RQ et al. High performance two-way full colors of transmission and reflection generated by hybrid Mg–TiO_2 metasurfaces. *Opt Laser Technol* **157**, 108770 (2023).
296. Yue WJ, Gao S, Lee SS et al. Highly reflective subtractive color filters capitalizing on a silicon metasurface integrated with nanostructured aluminum mirrors. *Laser Photonics Rev* **11**, 1600285 (2017).
297. Wang H, Ruan QF, Wang HT et al. Full color and grayscale painting with 3D printed low-index nanopillars. *Nano Lett* **21**, 4721–4729 (2021).
298. Overvig AC, Shrestha S, Malek SC et al. Dielectric metasurfaces for complete and independent control of the optical amplitude and phase. *Light Sci Appl* **8**, 92 (2019).
299. Yang JH, Babicheva VE, Yu MW et al. Structural colors enabled by lattice resonance on silicon nitride metasurfaces. *ACS Nano* **14**, 5678–5685 (2020).
300. Li WB, Zhang C, Lan D et al. Imbibition-induced ultrafast assembly and printing of colloidal photonic crystals. *J Colloid Interface Sci* **624**, 370–376 (2022).
301. Zhang J, Qin YP, Ou YT et al. Injectable granular hydrogels as colloidal assembly microreactors for customized structural colored objects. *Angew Chem Int Ed* **61**, e202206339 (2022).
302. Chen XM, Wang ZH, Tang MS et al. Reusable shape-memory photonic crystal paper for pin-printing and high-resolution press printing. *Adv Eng Mater* **25**, 2300753 (2023).
303. Shi SH, Lu H, Li YW et al. Asymmetric nanocavities with wide reflection color gamut for color printing. *Nanotechnology* **34**, 025201 (2023).
304. Zhao JC, Qiu M, Yu XC et al. Defining deep-subwavelength-resolution, wide-color-gamut, and large-viewing-angle flexible subtractive colors with an ultrathin asymmetric Fabry-Perot lossy cavity. *Adv Opt Mater* **7**, 1900646 (2019).
305. Choi S, Zhao Z, Zuo JW et al. Structural color printing via polymer-assisted photochemical deposition. *Light Sci Appl* **11**, 84 (2022).
306. Hu HB, Gao WJ, Zang R et al. Direct growth of vertically orientated nanocavity arrays for plasmonic color generation. *Adv Funct Mater* **30**, 2002287 (2020).
307. Cencillo-Abad P, Franklin D, Mastranzo-Ortega P et al. Ultralight plasmonic structural color paint. *Sci Adv* **9**, eadf7207 (2023).
308. Hail CU, Schnoering G, Damak M et al. A plasmonic painter's method of color mixing for a continuous red-green-blue palette. *ACS Nano* **14**, 1783–1791 (2020).
309. Zhang Y, Zhang LD, Zhang CQ et al. Continuous resin refilling and hydrogen bond synergistically assisted 3D structural color printing. *Nat Commun* **13**, 7095 (2022).
310. Demirörs AF, Poloni E, Chiesa M et al. Three-dimensional printing of photonic colloidal glasses into objects with isotropic structural color. *Nat Commun* **13**, 4397 (2022).
311. Xue J, Yin XW, Xue LL et al. Self-growing photonic composites with programmable colors and mechanical properties. *Nat Commun* **13**, 7823 (2022).
312. Wang WH, Wang L, Wang LY et al. Bio-inspired colorful selective solar absorber. *Sol Energy Mater Sol Cells* **276**, 113076 (2024).
313. Xu ZY, Niu WQ, Liu Y et al. 31.38 Gb/s GaN-based LED array visible light communication system enhanced with V-pit and sidewall quantum well structure. *Opto-Electron Sci* **2**, 230005 (2023).
314. Liang CL, Deng LG, Dai Q et al. Single-celled multifunctional

metasurfaces merging structural-color nanoprinting and holography. *Opt Express* **29**, 10737–10748 (2021).

Acknowledgements

This work was financially supported by the Natural Science Foundation of Shaanxi Province (Grant No. 2024JC-YBMS-291); Special Support Program for High-level Talents of Shaanxi Province (No. 2020-44). The authors thank Wenhui Dou (Rocket Force University of Engineering) for offering language support.

Author contributions

All authors commented on the manuscript. Wenhao Wang, Qianqian Fu and Wang Zhang contributed equally to this work, they wrote the original draft. Long Wang, Liuying Wang and Xiaohu Wu proposed the original idea and supervised the project. Gu Liu and Youju Huang reviewed and edited the manuscript. Jie Huang, Haoyuan Zhang and Fuqiang Guo drew the pictures.

Competing interests

The authors declare no competing financial interests.